DNA/LANGLEY
R-FILE

79737-CR

P.140

NAG1-530

IN-02

A NUMERICAL STUDY OF THREE-DIMENSIONAL

VORTEX BREAKDOWN

Robert E. Spall and
Robert L. Ash
Old Dominion University Research Foundation
Norfolk, Virginia

NASA

National Aeronautics and
Space Administration

MAY 1987

SUMMARY

A numerical simulation of bubble-type vortex breakdown using a unique discrete form of the full three-dimensional, unsteady incompressible Navier-Stokes equations was performed. The Navier-Stokes equations were written in a vorticity-velocity form and the physical problem was not restricted to axisymmetric flow. Based on the results of a previous study, the problem was parameterized in terms of a Rossby number-Reynolds number basis. Utilization of this parameter duo was shown to dictate the form of the free-field boundary condition specification and allowed control of axial breakdown location within the computational domain. The structure of the breakdown bubble was studied through time evolution plots of planar projected velocity vectors as well as through plots of particle traces and vortex lines. These results compared favorably with previous experimental studies. In addition, profiles of all three velocity components are presented at various axial stations and a Fourier analysis was performed to identify the dominant circumferential modes. The dynamics of the breakdown process were studied through plots of axial variation of rate of change of integrated total energy and rate of change of integrated enstrophy, as well as through contour plots of velocity, vorticity and pressure.

NOMENCLATURE

a	an adjustable constant associated with the vortex core diameter
A	n x m row vector where m is the number of unknowns in a cell
$[B_n]$	3x3 exponential transformation matrix
$\bar{c}$	a vector function, the cross product of which is divegrence free
e_{ij}	defined as $\frac{1}{2} (\frac{\partial u_i}{\partial x_j} + \frac{\partial u_j}{\partial x_i})$
F_i	scalar quantity in Kaczmarz relaxation scheme
g	boundary condition for the velocity vector
(h_x, h_y, h_z)	defined as $(\Delta x/2, \Delta y/2, \Delta z/2)$ respectively
$(\bar{h}_x, \bar{h}_y, \bar{h}_z)$	computational domain lengths in the x, y and z directions, respectively
K	a constant proportional to circulation
P	pressure variable
r	radial coordinate
r'	radial reference length defined as $(2v/a)^{1/2}$
r^*	radius where the swirl velocity is a maximum
R_i	residual quantity in Kaczmarz relaxation scheme
Re	Reynolds number; defined as $\frac{U^* r^*}{v}$
Ro	Rossby number; defined as $\frac{U^*}{r^* \Omega}$
t	time variable
(u,v,w)	velocity components in (x,y,z) system of coordinates respectively
U_∞	free stream axial velocity
U^*	axial velocity at a radius equal to r^*

U_o	axial velocity excess (or deficit) at the vortex centerline
v_θ	swirl velocity
(x,y,z)	Cartesian system of coordinates: x-axial, y-transverse, z-spanwise
$(\bar{x},\bar{y},\bar{z})$	nondimensional coordinates for use in grid generation; $0 < (\bar{x},\bar{y},\bar{z}) < 1$
(y_c, z_c)	transverse and spanwise coordinates corresponding to the location of the vortex centerline
(α,β,κ)	defined as $(\Delta x/\Delta z, \Delta x/\Delta y, \Delta y/\Delta z)$, respectively
$\bar{\delta}$	defined as U_o/U_∞
$(\delta_x, \delta_y, \delta_z)$	central difference spatial operators
δ_t	central difference time operator
$(\Delta x, \Delta y, \Delta z)$	discretization intervals
ε	stretching parameter for grid in y and z directions
$(\zeta_x, \zeta_y, \zeta_z)$	transformed vorticity in (x,y,z) system of coordinates, respectively
$(\theta_x, \theta_y, \theta_z)$	defined as $(\frac{u\Delta x}{2\nu}, \frac{v\Delta y}{2\nu}, \frac{w\Delta z}{2\nu})$, respectively
$(\lambda_x, \lambda_y, \lambda_z)$	defined as $(\Delta t/\Delta x, \Delta t/\Delta y, \Delta t/\Delta z)$, respectively
(μ_x, μ_y, μ_z)	spatial averaging operators
μ_t	time average operator
ν	kinematic viscosity
ρ	density
σ	stretching parameter for grid in x direction
τ	defined as $t_{n+1/2} - t_n$
τ'	defined as $t_{n+1} - t_{n+1/2}$
$(\bar{\phi}, \bar{\psi}, \bar{\xi})$	variables related to the gradient of vorticity
χ	a scalar quantity used in the Helmholtz projection
$(\omega_x, \omega_y, \omega_z)$	vorticity components in (x,y,z) system of coordinates respectively
Ω	rate of rotation taken in the limit as $r \to o$

INTRODUCTION

Vortices and vortical motions have played an important role in the development of theoretical fluid mechanics. For instance, the Helmholtz Theorems of Vorticity and generalizations by Kelvin, Crocco and others established flow properties involving the kinematics of vortex lines and the dynamics of vorticity. The theory of lifting surfaces, developed by Prandtl, Kutta and Joukowski, is based on the concept of a bound vortex. Recently, the recognition of large scale coherent vortical structures in turbulent flows has resulted in renewed interest in the study of vortices.

Although no general definition of a vortex exists, it can be thought of as a collection of fluid particles rotating around a common axis. Mathematically, vorticity is defined as the curl of the velocity vector and is equivalent to twice the angular velocity of a fluid particle. In addition, it is not necessary for a vorticity field to represent a vortex, an example being a parallel shear flow.

The most common development of a vortex occurs when a boundary layer separates from a surface and rolls up into a wake vortex. Tip vortices fall into this class. Tip vortices are generated when a fluid flows against a finite plate or sharp edged body at a nonzero angle of attack. These vortices are often highly stable structures and are characterized by a strong axial flow. Other examples of vortices with

1

an axial velocity component include tornados and waterspouts, intake vortices and swirling flows in pipes and tubes.

The presence of tip vortices in the wake of large aircraft constitute a hazard in areas of dense air traffic. These vortices can cause severe rolling of smaller aircraft that enter them. They are dissipated either by viscous dissipation, a sinusoidal type instability or, infrequently, by a core bursting mechanism.

Leading edge vortices shed from a delta wing induce a velocity field that results in increased lift and stability of the wing [1]. However, under certain conditions related to the angle of attack of the wing, these vortices can undergo a sudden and drastic change in structure known as vortex breakdown. This breakdown can alter severely the aerodynamic characteristics of the wing.

Swirling flows have been used to stabilize high intensity combustion processes [2]. Here a recirculation zone acts to stabilize combustion by recirculating hot gases to the root of the flame. In addition, combustion lengths are reduced due to the high levels of entrainment induced by the recirculation zone.

The ability to control these vortical structures is an important and active area of research. For example, it is desirable to delay the breakdown process over a delta wing and accelerate the process in regards to trailing wing tip vortices. In combustion applications, the internal structure of the recirculation (breakdown) region is of critical importance. Unfortunately, a comprehensive theory to describe the breakdown process and the parameters affecting it is lacking

presently, although several have been proposed. A review of these theories and supporting numerical and experimental work follows.

Vortex breakdown was first observed experimentally by Peckham and Atkinson [3]. They observed that vortices shed from a delta wing at high angles of attack appeared to "bell out" and dissipate several core diameters downstream from the trailing edge of a wing. Since then, vortex breakdown has been observed in swirling flows in straight pipes, nozzles, diffusers and combustion chambers, [2,4] and tornados [5]. Seven types of breakdown have been identified experimentally, [6] ranging from a mild "spiral" type to a strong "bubble" type breakdown. Observations in the early 1960's spurred considerable effort to develop a theoretical explanation of the vortex breakdown phenomena. Three schools of thought can be identified, all of which may be divided into three separate groups: 1) The concept of a critical state [7,8,9]; 2) Analogy to boundary layer separation [10,11] and, 3) Hydrodynamic instability [12,13,14].

Squire [7] appears to be the first to have performed a theoretical analysis of vortex breakdown. He suggested that if standing waves were able to exist on a vortex core then small disturbances, present downstream, could propogate upstream and cause breakdown. This is analogous to the earlier work of Taylor [15] on the stability of circular Couette flow. There, a linear stability analysis was performed to ascertain the ability of the base flow to support axisymmetric standing wave disturbances. Two of the cases studied by Squire assumed that the vortex flow was inviscid and axisymmetric. The assumed form of the upstream velocity distribution resulted in a linear disturbance equation which he then solved to determine a condition under which an

3

inviscid, axisymmetric, steady perturbation to the flow could exist. This condition, which was necessary for the existence of a standing wave, was taken to mark the transition between subcritical and supercritical states. In Squire's first case, the axial velocity, U, was considered to be a constant. The dimensionless swirl velocity V was taken piecewise as that of solid body rotation inside a core of unit radius ($V=V_0 r$) and connected with a potential vortex outside ($V=V_0/r$). A constant, V_0, was used to control the swirl. He found that for standing waves to exist a swirl parameter, "k", which was the ratio of the maximum swirl speed to the axial speed (V_{max}/U), had to be greater than, or equal to 1.20. When k=1.20 the wave is infinitely long, but it has a finite wavelength for k>1.20.

In the second case U was also taken to be a constant, but the swirl velocity was assumed to be $V = (V_0/r)(1-e^{-r^2})$ with V_0 a nondimensional parameter. Again Squire found that there was a condition on the swirl parameter k for the existence of a standing wave. This condition was $k=V_{max}/>1.0$ where we note that $V_{max}=0.638 V_0$.

Benjamin [8] examined this phenomena from a different point of view. He considered vortex breakdown to be a finite transition between two dynamically conjugate states of flow, similar to the occurrence of a hydraulic jump in open channel flow. These are a subcritical flow, which is defined as the state that is able to support standing waves, and the conjugate supercritical flow which is unable to support standing waves. Subcritical flows generally have higher swirl velocities than the conjugate supercritical flow. In this context, the work of Squire gives a condition marking the interface between these two states. As in the work of Squire, a universal characteristic parameter was defined

which delineates the critical regions of the flow. This parameter, denoted by N, is the ratio of absolute phase velocities of long wavelength waves which propagate along the vortex in the axial direction, i.e., $N=(C_+ + C_-)/(C_+ - C_-)$. Here C_+ and C_- are the phase velocities of the waves which propagate with and against the flow respectively. For N>1 the flow conditions are supercritical and for N<1, subcritical.

Benjamin applied this theory to a specific vortex flow, defined by a constant axial velocity, U, and $V=V_o r$, 0<r<1 and $V=V_o/r$, 1<r<R. If R→∞, this is just the combined vortex studied by Squire [7]. Benjamin found that the critical condition was the same form as Squire's. The precise value of the constant depends on the value of R but lies between 1.92 when R=1 and 1.20 when R approaches infinity. Thus Benjamin, although starting from a different perspective, arrived at the same critical condition for a combined vortex as did Squire.

A recent paper by Ito, Suematsu, and Hayase [16] examined both stationary and unsteady vortex breakdown in an inviscid, incompressible fluid. They considered the stability of a columnar vortex subjected to small amplitude disturbances. The disturbances considered were axisymmetric as well as asymmetric and either steady or unsteady. Their analysis produced a criterion for breakdown from the requirement for existence of solutions to their disturbance equations. A comparison of these results with those of Benjamin [8], for the case of a finite radius pipe containing a rigid-body rotation, gave the same criterion for breakdown. The important aspect of the work of Ito et al. lies in their interpretive criterion. Their nondimensionalization leads to the Rossby number as the controlling parameter. For example, in the case of

swirling pipe flow consisting of solid body rotation, the relevant scales are the axial velocity U, pipe radius r_0 and constant angular velocity of the flow, Ω. Thus the dimensionless controlling parameter is: $R_0 = U/r_0\Omega$.

Tsai and Widnall [17] examined a group velocity criterion which can be considered as a variation of the phase velocity criterion of Benjamin [8]. Their analyses of swirling pipe flow is more consistent with the view that breakdown occurs due to a wave trapping mechanism [18]. They assumed that the radial and axial velocity distributions could both be fit to exponential profiles [19]. They used a least squares fit given by Garg and Leibovich to calculate the dispersion relation from linear parallel stability theory. The group velocity associated with various flow profiles was then calculated. The results showed that upstream of breakdown the group velocity of both symmetric and asymmetric modes was directed downstream. Even though their criticality condition of zero group velocity proved to be an accurate guide for the various types of breakdown, they were unable to establish a relationship between vortex breakdown and wave trapping.

Bossel [9] concluded that breakdown was not analogous to the hydraulic jump, rather it was a regular feature of the Navier-Stokes equations for the given flowfield. This flowfield is considered to be supercritical with rigid initial rotation and some axial deceleration near the axis. Bossel divided the flowfield into two distinct regions: (1) An inner region, which could contain a stagnation point, and was approximated by the equations for an inviscid rotating flow; and (2), a viscous quasi-cylindrical region which surrounds the inner region. Bossel assumed the outer solution was known which produced conditions at

the boundary of the inviscid region that will result in breakdown. For a rigid rotation the inviscid equation for the stream function becomes linear and solutions were obtained by superposition. Results which resemble the configuration of a vortex breakdown were obtained.

Hall [11] considered vortex breakdown to be analagous to the separation of a two dimensional boundary layer. He assumed that a failure of the quasi-cylindrical approximation through large axial gradients signaled an impending vortex breakdown. A numerical experiment was performed to test the theory using experimental data obtained by Kirkpatrick [20]. A retardation of the flow along the axis was found. At this point, computations failed due to the inability of the iteration scheme to coverage. Hall considered this to represent the failure of the quasi-cylindrical approximation. In addition, stream tube divergence, pressure gradient, and swirl magnitude were varied parametrically and effected the failure of the quasi-cylindrical approximation in a manner consistent with their affect on vortex breakdown. Hall also found that the effect due to a change in Reynolds number was small.

Linear hydrodynamic stability theory investigates only the amplification or decay of infinitesimally small disturbances imposed on the base flow. Breakdown is then assumed to be analogous to laminar-turbulent transition. Of course, as pointed out by Leibovich [21], breakdown can occur with little sign of instability and conversely a vortex flow may become unstable and not undergo breakdown. In the case of zero axial velocity the Rayleigh [22] criterion (that the square of the circulation should nowhere decrease as r increases) provides a necessary and sufficient condition for flow stability.

That vortex breakdown may be a result of an hydrodynamic instability was first proposed by Ludwig [12]. He found a stability boundary with respect to spiral disturbances for an inviscid rotating flow in an annulus. It was proposed that this instability could be amplified and induce an asymmetry in the core. Ludwig's idea has not been widely accepted due to the difficulty of relating the geometry of his analyses to vortex breakdown.

Howard and Gupta [13] have shown that the stability of the quasi cylindrical approximation s guaranteed if the "Richardson number" criterion $r^{-1}(\partial u_r/\partial r)^{-2}V_\theta [\partial(rV_\theta)/\partial r] < 1/4$ is satisfied. This implies that the role of swirl is purely stabilizing for axisymmetric disturbances. In practice, nearly all approach flows turn out to be stable to axisymmetric disturbances [21].

Pedley [23] considered the stability of an almost fully developed viscous flow in a rotating pipe. He found that the flow became unstable to asymmetric disturbances for sufficiently small values of the Rossby number (defined in terms of the rate of rotation of the pipe, the pipe radius and the axial velocity of the fluid) at a critical Reynolds number of 82.9.

Lessen, Singh and Paillet [14] defined a parameter, q, involving the ratio of the magnitude of the maximum swirl to that of the maximum axial velocity. This parameter completely determined the inviscid stability characteristics of the flow defined by the equations $V_\theta = (q/r)(1-e^{-r^2})$, $U = e^{-r^2}$. Thus a wake or jet-like axial velocity profile does not affect stability. They found that the flow was stable to all disturbances for q>1.5 and unstable to nonaxisymmetric

disturbances for smaller values of q. Thus, from the point of view of stability, the role of swirl is stabilizing with respect to axisymmetric disturbances, and destabilizing with respect to asymmetric disturbances over a range of q.

After the initial observations of vortex breakdown by Peckham and Atkinson [3], experimentalists began studying vortex breakdown in a more controllable setting. Harvey [24] performed experiments in a long tube, imparting a swirl velocity on the fluid as it entered. This was done using a set of adjustable vanes mounted in the inlet section. Harvey concluded that for low swirl velocities the classical vortex was obtained but as the swirl was increased a breakdown bubble formed. He also concluded that the breakdown was due to a critical state phenomena and not a hydrodynamic instability since the flow reverted to a normal swirling flow downstream of the breakdown bubble. Instabilities usually result in increasingly large amplitude velocity fluctuations ending in a turbulent flow.

Sarpkaya [25] described experiments in swirling flows in a diverging cylindrical tube. He observed three types of breakdown; double helix, spiral, and axisymmetric. The type of breakdown that occurred depended on a combination of Reynolds number (based on tube diameter and mean axial velocity) and circulation. For 1000<Re<2000 the spiral or double helix breakdown was observed. Axisymmetric breakdown was found to develop from the double helix or spiral form, or as an axisymmetric swelling of the core. For high Reynolds numbers and circulation the axisymmetric type breakdown occurred as a swelling of the vortex core. He also noted that the axisymmetric breakdown responded to changes in upstream and downstream flow conditions in a

manner analagous to hydraulic jump in an open channel flow. In a later paper, Sarpkaya [26] concluded that Benjamin's finite transition concept was in complete agreement with experimental results in the region where axisymmetric breakdown occurred (high swirl and Re). The spiral breakdown appeared to be a consequence of the instability of the flow due to asymmetric disturbances. He concluded that the overall mechanism for vortex breakdown might encompass finite transition and hydrodynamic instability theories, each applicable in a specific region.

Faler and Leibovich [27] have mapped the internal structure of an axisymmetric type vortex breakdown using a laser-Doppler anemometer. They found that the interior of the bubble, which contained a two celled structure, was dominated by low frequency periodic velocity fluctuations. The magnitude of these fluctuations was greatest in the rear portion of the bubble. In addition, four stagnation points existed on the axis.

The affect of an adverse pressure gradient on vortex breakdown has been examined by Sarpkaya [28] and more recently by Delray et al. [29]. Delray found experimental limits for vortex breakdown as a function of adverse pressure gradient and vortex strength. Pressure measurements showed considerable pressure increase within the core for small variations outside the core. In general, as the adverse pressure gradient increased, the swirl required to induce vortex breakdown decreased.

Numerical solutions for vortex bursting have been reported by at least seven previous investigators [30,31,32,33,34,35,36]. In all cases, the flows were assumed to be incompressible and were restricted

to studies of laminar, axisymmetric systems. The solutions by Kraus
et al. and Hafez et al. were time dependent while the others were steady
state solutions.

Kopecky and Torrance [31] considered axisymmetric swirling flow
through a cylindrical tube. The fluid entered the tube with an
exponential swirl velocity. This distribution behaved as a solid body
near the axis and as a potential vortex away from the axis, representing
a solution to the Navier-Stokes equations for the limiting case of
Reynolds number approaching infinity. A parametric study was performed
with Reynolds numbers (based on tube radius and constant axial velocity)
ranging from 50 to 500 and swirl ratios from 0.4 to 10. The development
of a recirculation zone was demonstrated as the swirl was increased for
fixed Reynolds number and core diameter. Similar results were obtained
when the core diameter and swirl were fixed while the Reynolds number
was increased. In all cases the breakdown appeared to form at the inlet
station. With a grid spacing of 0.25 in the streamwise direction the
major portion of the breakdown was contained within about four grid
points. While this grid seems excessively coarse, Kopecky and Torrance
reported that doubling the number of grid points in the streamwise
direction produced similar results.

Grabowski and Berger [33] solved the steady axisymmetric Navier-
Stokes equations for a free vortex approximated by a two parameter
family of assumed inflow distributions. The inflows were the polynomial
profiles given by Mager [37] in his integral analysis, imbedded in an
irrotational flow. The equations of motion were written in terms of
stretched coordinates in the radial and axial directions. At inflow, a
parameter, alpha, could be varied to allow for jet like or wake like

axial profiles. An "artificial compressibility" technique was used to solve the equations of motion. Solutions were obtained which exhibited many of the characteristics of vortex breakdown for Reynolds numbers up to 200. These solutions were obtained with upstream conditions that were, in many cases, subcritical. Their results appear to refute the finite transition theory of Benjamin [8] which required the flow upstream of breakdown to be supercritical.

Narin [32] investigated the occurrence of vortex breakdown for three different flow configurations: (1) a straight tube, (2) a step tube, and (3) confined jet mixing. This appears to be the only work investigating the breakdown of a confined jet, which consists of a swirling jet discharging into a coaxial nonrotating surrounding stream. For this configuration, the resulting flow field depended on the radius of the enclosing tube, jet velocity and swirl ratio, and on the velocity of the surrounding stream. In general, increasing Reynolds number and swirl ratio enhanced the severity of the vortex breakdown.

Benay [35] has also simulated vortex breakdown by a numerical solution of the laminar axisymmetric Navier-Stokes equations. At inflow, an exponential circumferential velocity distribution was imposed in a parametric study to determine the effect of vortex core radius, Reynolds number (based on tube radius and free stream axial velocity), and tangential and axial velocity on vortex breakdown. In general, an increase in the Reynolds number or swirl ratio resulted in a more pronounced recirculation zone.

Excellent review articles summarizing vortex breakdown research have been published by Hall [38] and Leibovich [21,39]. Since relevant

numerical work only began in the mid 1970's, only Leibovich's survey includes those investigations. He noted that the numerical solutions do not show a two celled structure within the breakdown bubble as revealed in physical experiments by Faler and Leibovich [27]. In addition, Faler and Leibovich measured four stagnation points along the axis, whereas numerical experiments have shown only two. However, this structure was later claimed to have been computed by Kraus, Shi, and Hartwich [34] by studying the flow in a time dependent manner. An examination of their computed streamlines reveals that the bubble has lifted off the axis for some of the time levels shown. At these time levels no stagnation points are present along the axis. Leibovich is also critical of the fact that the numerical solutions "contain strong axial gradients right up to the initial axial station." He suggests that the bubble may pass through the initial stations if the inlet boundary conditions were relaxed. In addition, axisymmetric numerical solutions show bubbles that increase in size as swirl is increased, a result that is not consistent with experimental observations. Furthermore, axisymmetric numerical simulations are unable to predict spiral type breakdowns, which are a common occurrence in experiments [6,25]. Thus, Leibovich has concluded that "the assumption of steady axisymmetric motion may not be adequate to compute all the detailed structure of vortex breakdown."

The purpose of this work was to study numerically the spatial and temporal evolution of a class of vortical structures. Wing tip vortices are of specific interest, but the influence of wing geometry on the tip vortices was beyond the scope of this analysis. A numerical solution has been chosen because closed form analytic solutions of the equations of motion are unlikely to be found without assuming overly restrictive,

simplified flow fields. An experimental approach was also deemed impractical because of the difficulty in making accurate measurements in regions where the velocity gradients are extreme, which is often the situation during vortex breakdown. Thus, the unsteady, three-dimensional, laminar Navier-Stokes equations have been integrated numerically to study the parameters affecting the evolution and possible breakdown of an isolated wing tip vortex.

Authors of the numerical studies cited previously report breakdown at or immediately downstream of the inflow boundary. It will be shown that these previous computational results can be re-evaluated in terms of a single parameter which identifies the cause of the breakdown at inflow. Through an examination of several previous studies concentrating on standing wave analyses, it is shown that the controlling parameter is the Rossby number. A means of avoiding the problem of breakdown at inflow is suggested, and the numerical analyses is then performed with the Rossby number and Reynolds number as the nondimensional parameters. It is important to emphasize the fact that the algorithm was not restricted by an axisymmetry requirement. This allowed for the existence of asymmetric disturbances which may be important in the breakdown process. Previous numerical simulations have precluded this possibility. The numerical algorithm which has been used is an implementation of the "velocity-vorticity" formulation of Gatski, Grosch and Rose [39]. The pressure, although not a variable in the formulation, was computed.

Contour plots of pressure, Bernoulli's constant, axial velocity and vorticity are displayed as a part of this investigation. Particle traces, vortex lines and velocity vector plots have been obtained using

the PLOT3D, a three-dimensional color graphics program implemented on an Iris workstation at NASA Langley Research Center. In addition, the rates of change of energy and enstrophy were computed and plotted as a function of axial location. Conclusions have been drawn which may be useful in the interpretation, as well as the modification and control, of wing tip vortices. Finally, the internal structure of the vortex breakdown bubble is discussed.

THE ROSSBY NUMBER - BREAKDOWN CRITERION

The Rossby number is an important control parameter in the study of large scale atmospheric and oceanic motions. It is a measure of the relative importance of the Coriolis and inertial forces on the fluid motion. The Coriolis force is due to the rotation of fluid and is directed perpendicular to the axis of rotation. In the study of geophysical fluid dynamics, fluid rotation is generally considered to be of the rigid body type. However, the Coriolis forces can be important for a variety of circumferential velocity distributions associated with other flows, such as those occurring in wing tip and leading edge vortices. When significant, the Coriolis acceleration represents a restoring force, providing a mechanism for the creation of waves (in the absence of sufficient damping). It tends to restore fluid particles displaced laterally from their equilibrium positions. However, the restoring force can cause the fluid particles to overshoot their original locations, setting up an oscillatory motion. Under some conditions the fluid can sustain these oscillations, and in the case of vortex flows, these wavelike fluctuations can then propagate along the axis of the vortex. Waves of this type are known as inertial waves [40]. The intent of this chapter is to show how the vortex breakdown phenomenon can be characterized in terms of the ability of a base flow to support these waves. This effect can be described, in terms of the

Rossby number, and can be justified by using the theoretical, experimental and computational literature discussed in the introduction.

Throughout the remainder of this chapter a cylindrical polar coordinate system, (r, θ, x), with corresponding velocity components, w in the radial (r) direction, v in the circumferential (θ) direction, and u in the axial (x) direction are employed.

The Rossby number can be developed naturally from the vorticity transport equation and is defined as the ratio of the inertial forces to the Coriolis forces as

$$Ro = \frac{u}{r^{*}\Omega} \tag{2.1}$$

where u is a representative velocity magnitude, r^{*} a characteristic length, and Ω, a characteristic rate of rotation of the flow. For the flows considered in this study, r^{*} is taken to be the vortex core diameter, defined as the radius of maximum swirl velocity. The reference velocity u is taken as the axial velocity at the core radius (r^{*}). Wing tip vortices are characterized by a solid body type rotation near the axis, and this is taken to be the characteristic rate of rotation, Ω.

As discussed earlier, Squire [7], Benjamin [8] and Ito et al. [16] were able to derive a criterion for the existence of standing waves on a vortical base flow. Squire [7] and Benjamin [8] formulated this criterion in terms of characteristic circumferential and axial velocities. Here it will be shown that their criteria can be reinterpreted in terms of a Rossby number.

The most important case considered by Squire, in terms of a model for vortex breakdown, was an exponential form for the circumferential velocity profile, given by:

$$v = \frac{V_0}{r} (1 - e^{-r^2})$$ (2.2)

with V_0 used as a scaling parameter. The axial velocity was considered to be a constant, i. e. $u = U$. Recall from the introduction that the existence of neutrally stable standing waves occurred when

$$V_m/U = 1.0$$ (2.3)

where V_m is the maximum swirl velocity. In addition, it should be noted that the maximum swirl velocity using Squire's velocity profile is $V_m = 0.638 \, V_0$, at $r^* = 1.12$.

Consistent with our previous definitions, the reference length, r^*, is given as:

$$r^* = 1.12.$$ (2.4)

The reference velocity is the constant axial velocity, U. The characteristic rate of rotation, Ω, is given as:

$$\Omega = \lim_{r \to 0} (v/r) = V_0.$$ (2.5)

Hence the Rossby number is then given as:

$$Ro = 0.57.$$ (2.6)

The combined vortex considered by Benjamin [8] is given by

$$v = V_o r \qquad 0 < r < 1$$

$$v = V_o/r \qquad 1 < r < R \qquad (2.7)$$

$$u = U \qquad all\ r$$

where V_o is a constant.

The critical condition, for R=1 and R → ∞ is given as

$$V_o/U = 1.92 \qquad for\ R = 1$$

$$V_o/U = 1.20 \qquad for\ R \to \infty \qquad (2.8)$$

The case R→∞, corresponds to the combined vortex studied by Squire [7]. The case R=1 corresponds to a solid body rotation within a tube and was also studied by Ito et al. [16]. The characteristic radius is taken to be the distance at which the solid body rotation and irrotational flow are matched. Thus, r^* is equal to unity and Ω is equal to V_o. These results can be expressed in terms of a Rossby number as

$$Ro = 0.52 \qquad for\ R = 1$$

$$Ro = 0.83 \qquad for\ R \to \infty \qquad (2.9)$$

From the above analyses, it appears that a criterion based on the Rossby number can be used to delineate the critical regions of the vortex flow but the critical value depends upon the type of vortex flow. This criterion was then used as a basis for examining a variety of vortex flows. Previous computational and experimental work has been examined for both confined and unconfined flows to determine the range of applicability of this Rossby number parameter.

The computational studies of Kopecky and Torrance [31], Grabowski and Berger [33], Benay [35] and Hafez et al. [36] have been reinterpreted in terms of the Rossby number. The circumferential velocity profiles used by Kopecky and Torrance and Benay are of exponential form, similar to Eq. (2.2). Grabowski and Berger [33] and Hafez et al. [36] express the circumferential velocity in terms of a polynomial. Both profile types asymptote to solid body rotation near the axis. The exponential profile asymptotes to an irrotational flow in the far field. The polynomial profile is exactly irrotational outside a specific core radius.

The circumferential velocity profile of Grabowski and Berger [33] and Hafez et al. [36], in nondimensional form, is expressed as

$$v = Vr(2 - r^2) \qquad 0 < r < 1$$
$$v = V/r \qquad 1 < r < R$$

$$(2.10)$$

The axial velocity profile is given as

$$u = \alpha + (1-\alpha)r(6-8r+3r^2) \qquad 0 \le r < 1$$
$$u = 1 \qquad 1 < r < R$$

$$(2.11)$$

where α is an adjustable parameter to allow for jet-like or wake-like profiles. The circumferential velocity is a maximum at $r = \sqrt{2/3}$, and is equal to 1.088 V. The characteristic rate of rotation, Ω, is given as

$$\Omega = \lim_{r \to 0} (v/r) = 2 V U_\infty /\delta \qquad (2.12)$$

20

where δ is the dimensional core radius at the inflow plane and U_∞ the dimensional free stream axial velocity. The radius of maximum swirl velocity is given as

$$r^* = \sqrt{2/3}\; \delta. \tag{2.13}$$

The characteristic axial velocity becomes

$$u = \left\{\alpha + (1-\alpha)\; 8\sqrt{2/3}\; (1- \sqrt{2/3})\right\} U_\infty \tag{2.14}$$

For the case of $\alpha = 1$, i.e. $u = U_\infty$, the Rossby number becomes

$$Ro = .612/V \tag{2.15}$$

where V is a parameter describing the circumferential velocity profile. The Reynolds number, based on the free stream axial velocity, U_∞, and the characteristic radius, r^*, becomes

$$Re = \sqrt{2/3}\; U_\infty\; \delta/\nu \tag{2.16}$$

where $U_\infty\, \delta/\nu$ is the form of the Reynolds number employed by Grabowski and Berger [33] and Hafez et al. [36].

In a similar manner, expressions for the Rossby number and Reynolds number can be extracted from the works of Kopecky & Torrance [31] and Benay [35]. Using the notation employed by these authors, the following results are obtained for u = constant

$$Ro = \frac{1}{1.12 \sqrt{B}\; \Gamma_0} \tag{2.17}$$

$$Re = \frac{1.12}{\sqrt{B}\; (U_\infty\, r_0/\nu)} \tag{2.18}$$

The results of the previous works are summarized in Fig. 1.1 in terms of the Rossby and Reynolds numbers. Open symbols denote breakdown and closed symbols denote no breakdown. That figure and Fig. 1.2 have employed an axial velocity criterion to define breakdown. For confined flows and numerical solutions, vortex breakdown is defined as a flow which produces stagnation of the axial velocity component. For unconfined flows, breakdown is considered to be a rapid expansion of the vortex core accompanied by a sudden deceleration of the axial velocity. A limit line exists that separates regions of vortex breakdown from regions that experience no breakdown.

The computational results show a Reynolds number dependence in the low Reynolds number range. From Fig. 2.1, it can be seen that for Reynolds numbers above 100, viscous effects appear to be negligible and inviscid theory can be expected to give good results. The dashed line represents the inviscid standing wave theory developed by Squire [7] for an exponentially varying circumferential velocity profile.

The experimental results appearing in Fig. 2.1 are all at higher Reynolds numbers than the numerical simulations. Garg and Leibovich [19] and Uchida et al. [41] made LDV measurements just upstream of breakdown in a tube and vane apparatus. In the case of Garg and Leibovich, a least squares fit of the data was used to obtain exponential profiles for both the circumferential and axial velocity distributions. These results were easily translated to the Rossby number and Reynolds number previously defined. The bubble form of breakdown occurred at a lower Rossby number (~ 0.57) than the spiral form (~ 0.63). From the available data, it appears that the Rossby
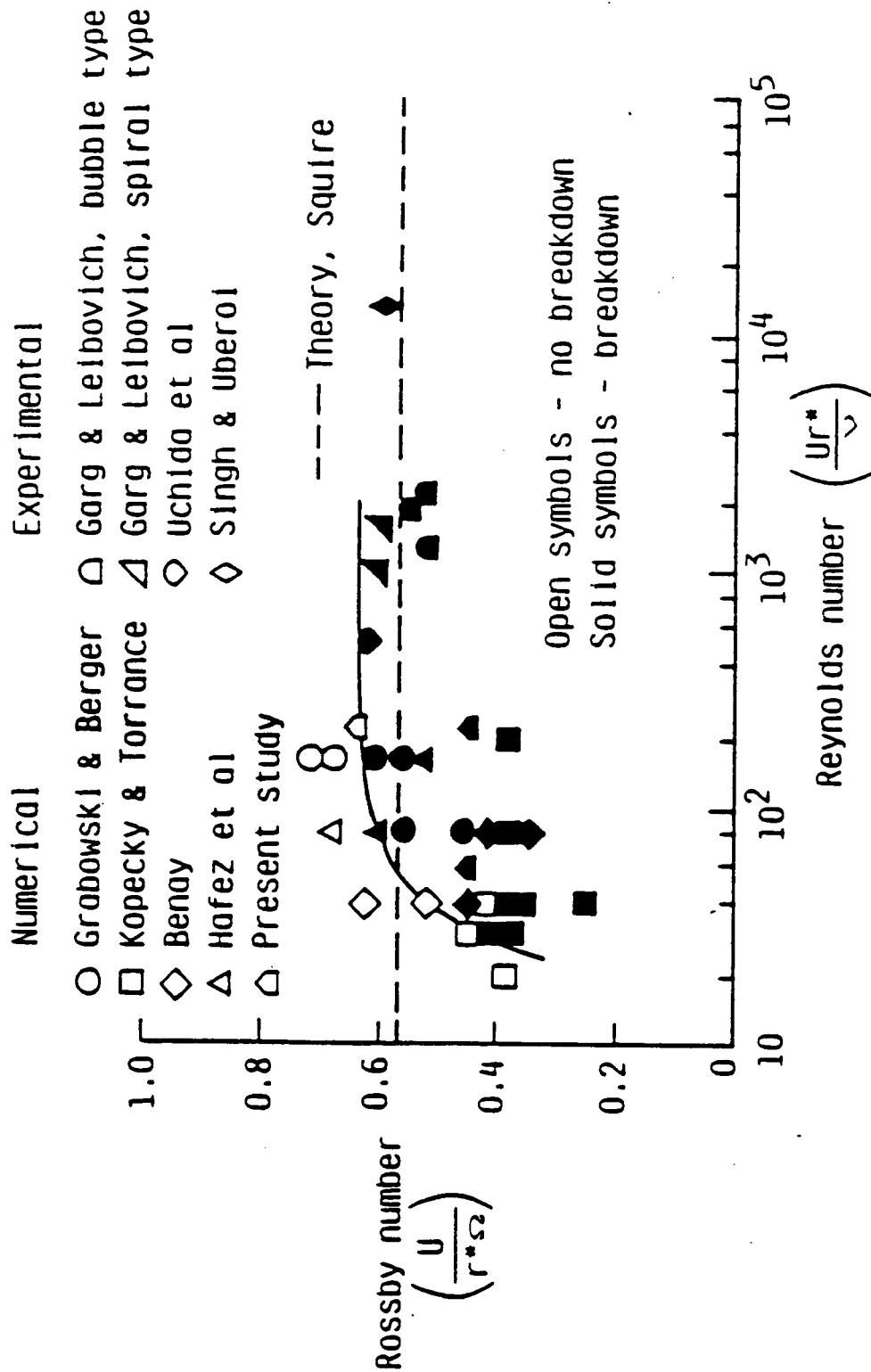
Fig. 2.1 Correlation of Rossby number for vortex breakdown (shaded symbols) with Reynolds number. Wing tip vortex case.
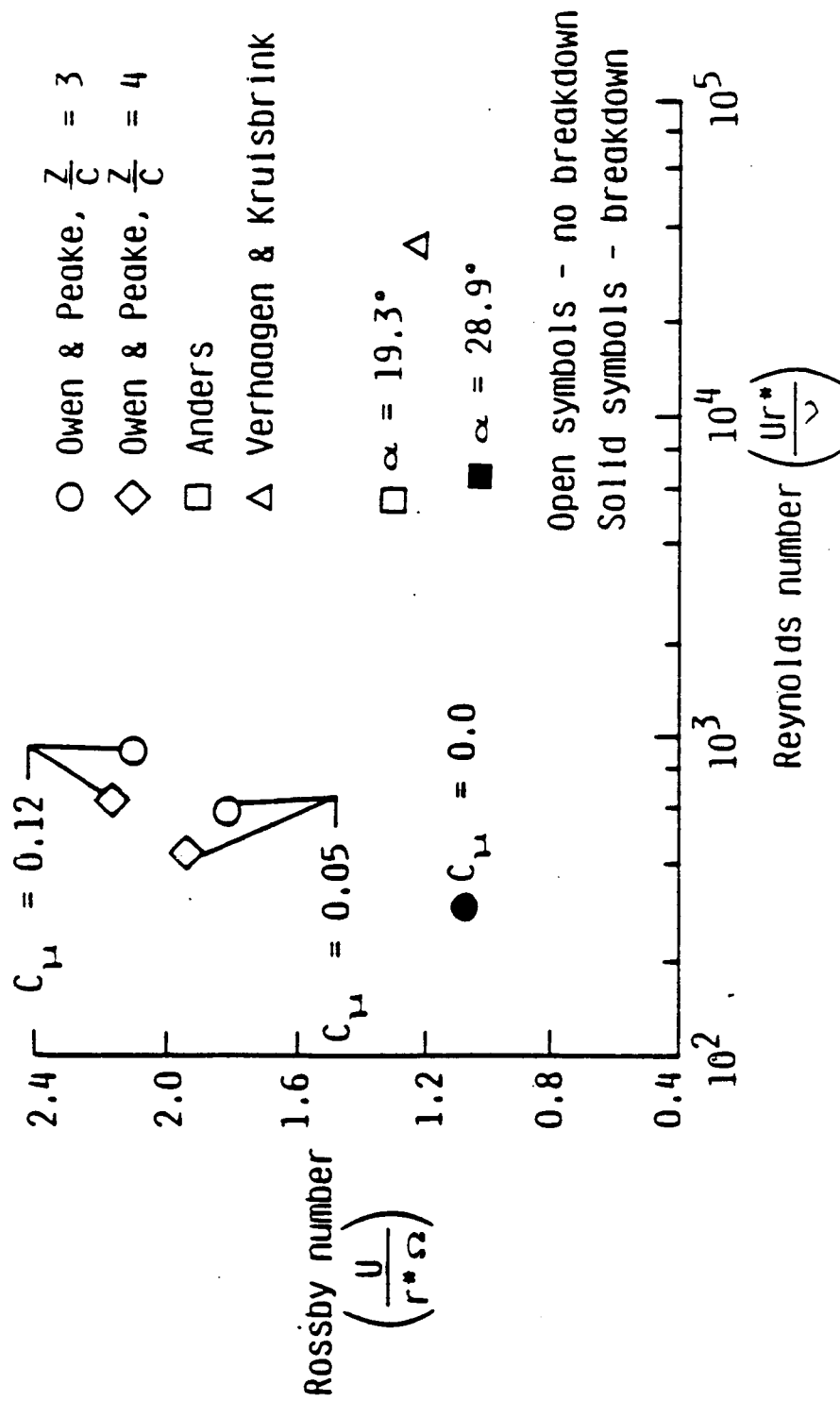
Fig. 2.2 Correlation of Rossby number for vortex breakdown (shaded symbols) with Reynolds number. Leading edge vortex case.

number at inflow, in the case of the bubble form of breakdown, was already below the level of the Rossby number at which the spiral form of breakdown occurred. The Rossby number for the Uchida et al. work, obtained from plots of the axial and circumferential velocity profiles, equaled 0.64 for the bubble form of breakdown. Note the excellent agreement between these confined experimental flows and the inviscid standing wave analyses of Squire.

Singh and Uberoi [42] measured the velocity distribution of a wing tip vortex at several axial stations along the vortex core. A laminar flow wing was used to generate the vortex. Their measurements provided enough information to obtain an estimate of the Rossby number, (~ 0.60) and Reynolds number, (~ 13000) just upstream of a region in which the axial velocity decreases rapidly to 0.3 U_∞ , suggesting vortex breakdown.

Based on Fig. 2.1 the critical Rossby number for the symmetric form of breakdown for the trailing wing tip class of vortices is approximately 0.60. The computational results indicate that for Reynolds numbers below 100, the value of the critical Rossby number is decreased, undoubtedly due to the increased damping effects of viscosity on the wave motions.

Figure 2.2 displays the Rossby number-Reynolds number relationship for leading edge vortices. The experimental data were obtained from reports by Owen and Peake [43], Anders [44] and Verhaagen and Kruisbrink [45]. Once again, open symbols denote no breakdown and closed symbols denote breakdown.

Anders [44] made LDV measurements of a leading edge vortex over a delta wing at two different angles of attack; 19.3° and 28.9°. The vortex produced by the wing at the lesser angle of attack did not break down. The vortex produced at the angle of attack of 28.9° degrees broke down above the delta wing. The Rossby number is computed at the same distance from the apex of the wing for both cases.

Blowing can stabilize a leading edge vortex and thus change the breakdown criterion. Owen and Peake [43] introduced core blowing into vortices shed from delta wings at high angles of attack to study its effect on vortex breakdown. The symbols in Fig. 2.2 representing these data are variations based on a blowing coefficient parameter, C_μ, at fixed streamwise locations $z/c=3$ and $z/c=4$, where c is the chord length of the delta wing. Owen and Peake state that breakdown occurs for the case $C_\mu = 0.0$, while for the cases $C_\mu = 0.05$ and $C_\mu = 0.12$ the flow is stabilized and no breakdown occurs.

Although the data are sparse and the evaluation of the Rossby number approximate, one may conclude that vortex breakdown for leading edge vortices occurs at a higher Rossby number than for trailing wing tip vortices. This may be due to the fact that the swirl velocity profiles are of a different type. Far downstream, the flow outside the core of a trailing wing tip vortex is nearly irrotational. For a leading edge vortex, the flow at the edge of the core is rotational and nearly inviscid. In addition, the leading edge vortex contains a narrow viscous subcore where the radial gradients of the circumferential velocity are extremely large. In contrast, a significant region of fluid near the center of a wing tip vortex tends to rotate like a rigid body.

No standing wave analyses of velocity profiles applicable to leading edge vortices were found during this investigation. That analysis could predict an analytic Rossby number breakdown criterion for leading edge vortices and would bridge the two cases. However, based on experimental results, the critical Rossby number should be near unity.

In summary, the theoretical analyses of Squire [7], Benjamin [8] and Ito et al. [16] have been reinterpreted to enable the identification of a criterion that predicts the existence of axisymmetric standing waves based on a Rossby number. An exponential representation of the circumferential velocity profile, which most closely models experimental flows, yields a critical Rossby number of 0.57. This value is shown as a dashed line on Fig. 2. The experimental data of Garg and Leibovich [19], interpreted in terms of a Rossby number, shows that the spiral form of breakdown occurs when the local Rossby number falls to approximately 0.63. From the available data, the local Rossby number was initially below 0.63 for the cases involving the bubble form of breakdown. Numerical experiments reveal that the critical value of the Rossby number for the bubble form of breakdown becomes independent of Reynolds number above Reynolds numbers of 100. At lower values of the Reynolds number, a lower Rossby number is required to initiate breakdown.

NUMERICAL FORMULATION

The governing equations describing incompressible, isothermal flow of a Newtonian fluid are given by:

$$\nabla \cdot \bar{u} = 0 \tag{3.1}$$

$$\frac{D\bar{u}}{Dt} = \frac{-1}{\rho} \nabla P + \nu \nabla^2 \bar{u} \tag{3.2}$$

subject to $\qquad \bar{u} = \bar{g} \qquad$ on boundary B. $\qquad$ (3.3)

Here, Eqs. (3.1) and (3.2) represent the continuity equation and the Navier-Stokes equation's respectively, each valid over a domain D. Equation (3.3) is a statement of specified velocity boundary condition to be satisfied on the boundary, B, of the domain. Higher order equations involving the vorticity, $\bar{\omega}$, are given by:

$$\nabla \cdot \bar{u} = 0$$

$$\nabla \times \bar{u} = \bar{\omega} \tag{3.4}$$

$$\frac{D\bar{\omega}}{Dt} = \bar{\omega} \cdot \nabla \bar{u} + \nu \nabla^2 \bar{\omega} \tag{3.5}$$

$$\nabla \cdot \bar{\omega} = 0 \tag{3.6}$$

with a corresponding boundary condition:

$$\bar{\omega} = \nabla \times \bar{u}. \tag{3.7}$$

on B.

Equation (3.4) represents the definition of vorticity, Eq. (3.5) the vorticity transport equation and Eq. (3.6) the solenoidal condition on the vorticity vector. Equation (3.6) is an identity obtained by taking the divergence of each side of Eq. (3.4). The numerical scheme used to solve these equations represents an implementation of a method described by Gatski, Grosch and Rose [39]. The scheme is second order accurate in time and space for the vorticity and velocity variables, and is independent of the local cell Reynolds number. A major advantage of this formulation is that boundary conditions for the pressure are not needed to advance the solution in time. (The difficulty in specifying the pressure boundary conditions accurately has been discussed by Orszag, et al. [46].)

Several major aspects of this algorithm can be identified. Equations (3.1) and (3.4) form the basis for the solution to the velocity vector field when given the vorticity vector field at any time level n, along with the velocity boundary conditions. Equation (3.5) is utilized to advance the vorticity field from time level n to time level n+1. Here, the boundary condition, Eq. (3.7), is needed to produce a unique solution to the higher order system of equations which are solutions to Eq. (3.1) and Eq. (3.2) subject to the boundary condition prescribed by Eq. (3.3). The solution of Eq. (3.6) is used periodically during the time evolution of the flow field to ensure that the vorticity vector remains divergence free. That is, the divergence free requirement is tested at each time level and if it fails to meet its tolerance, Eq. (3.6) is employed.

For reference purposes, a brief description of the computational sequence follows. The physical domain is first divided into a

computational region of rectangular cells IMAX x JMAX x KMAX. A typical cell is sketched in Figure 3.1. Velocities, defined at the centers of faces, are the average of box variables defined at the vertices of cells. The numbering scheme (1-8) for the box variables is shown in Figure 3.1. Vorticity is also defined at the center of each cell face. The velocity and vorticity variables thus represent average values over a cell face.

Beginning with an assumed vorticity distribution, the velocities, utilizing Eqs. (3.1) and (3.4) are computed at time level n. The vorticity is then advanced to level n+1 using the velocities at time level n and vorticity boundary conditions determined by the velocity components on each boundary. This vorticity is subsequently projected into a new vector space satisfying the requirement that the divergence of vorticity be zero. Next, velocities are updated to time level n+1 using the divergence free vorticity at n . and appropriate velocity boundary conditions. The vorticity is then recomputed at level n+1 using the updated velocity field. Repetition of the above process yields a second order accurate solution at any subsequent time [39].

Numerically, it is required that one component of the velocity vector be specified on each boundary cell face. All three components of the vorticity vector are specified on each boundary cell face.

Velocity Equations

Assuming the vorticity at time level n is known, the velocity components at level n can be computed through a numerical solution of Eqs. (3.1) and (3.4) where $\bar{\omega}$ satisfies the compatibility condition, Eq. (3.6). Fix and Rose [47] have shown that this compatibility condition
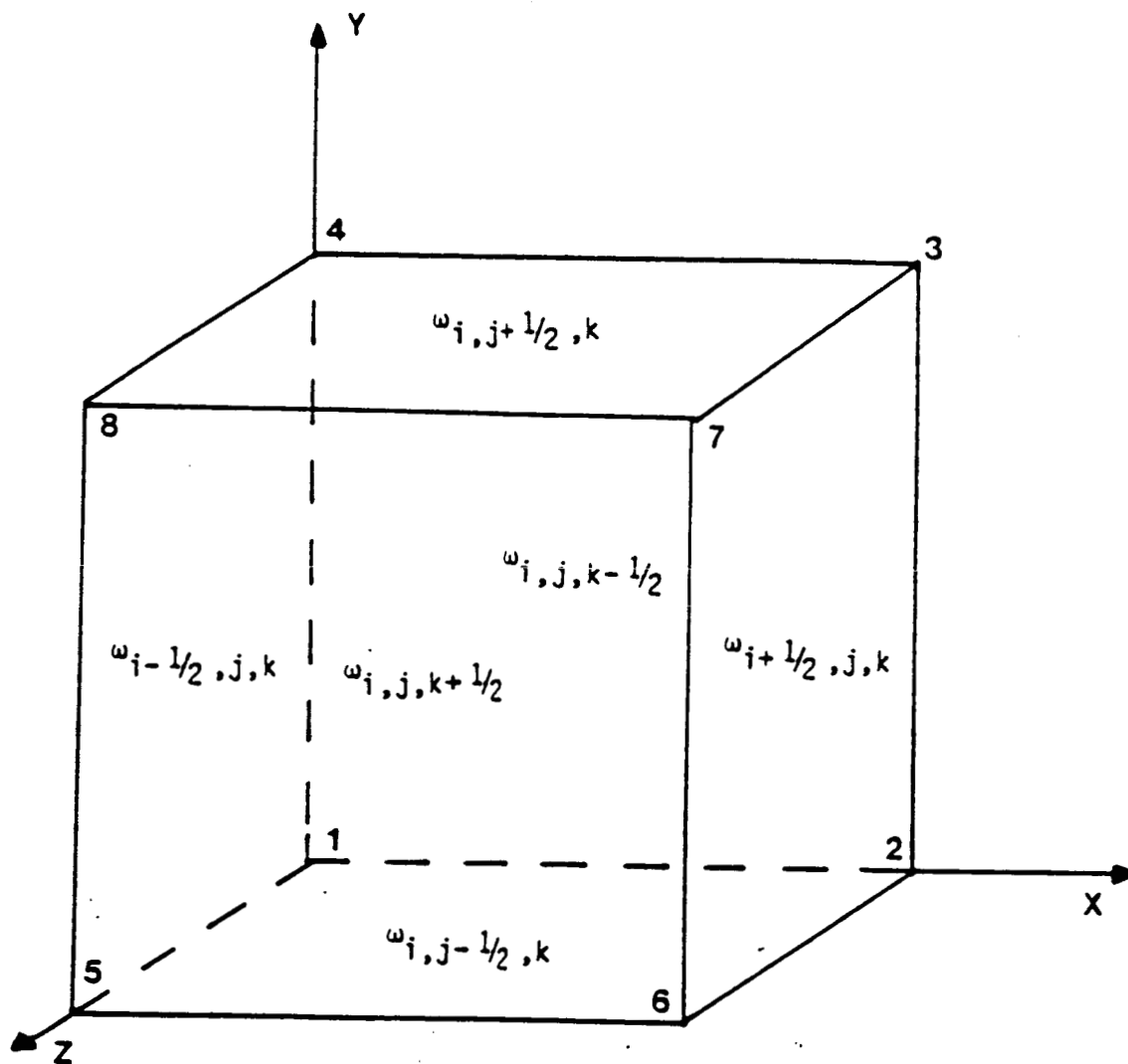
Fig. 3.1 Representative computational cell showing the location of
the velocity and vorticity variables.

is a necessary condition for the overdetermined system, Eq. (3.1) and Eq. (3.4) to have a solution.

A finite volume approximation to the continuity equation is obtained by applying the divergence theorem to the integral form of the continuity equation. That approach results in the requirement:

$$\int \nabla \cdot \bar{u} dV = \int \bar{u} \cdot \hat{n} d\sigma \qquad (3.8)$$

The integral on the right hand side represents the net flux of mass into any arbitrary fixed volume. It is convenient to define an operator $\nabla_h \cdot \bar{u}$, as

$$\nabla_h \cdot \bar{u} = \frac{1}{|V|} \int \bar{u} \cdot \hat{n} \, d\sigma. \qquad (3.9)$$

Using the trapezoidal rule, the continuity requirement can be expressed as

$$\nabla_h \cdot \bar{u} = \Sigma \, \delta_i u_i \qquad i = 1,2,3 \qquad (3.10)$$

(where δ_i is the standard difference operator, $\delta_i u_i \equiv (u_{i+\frac{1}{2}} - u_{i-\frac{1}{2}})/\Delta x_i$)

so that $\qquad \nabla_h \cdot \bar{u} = \nabla \cdot \bar{u} + 0 \ (h^2) \qquad (3.11)$

The discretized form of the definition of vorticity results from an application of Stokes theorem. Consider a two-sided surface in three dimensions having a closed surface C as its boundary. The circulation of the velocity u around C is equal to the flux of the curl of u over S, i.e.,

$$\int_S (\nabla \times \bar{u}) \cdot \hat{n} dS = \int_C \bar{u} \cdot d\hat{C} \qquad (3.12)$$

where n is a unit normal to the surface S. We can define a second operator $\nabla_h \times \bar{u}$ as

$$\nabla_h \times \bar{u} = \frac{1}{|A|} \int_C \bar{u} \cdot d\hat{C} \qquad (3.13)$$

Using the trapezoidal rule, the discrete form of the curl operator is given as

$$\left(\nabla_h \times \bar{u}\right)_k = \delta_i u_j - \delta_j u_i \qquad (3.14)$$

so that $\qquad \nabla_h \times \bar{u} = \nabla \times \bar{u} + O(h^2) \qquad (3.15)$

The preceding approximations are valid over the entire computational domain. Additional equations are needed for boundary cells. For the numerical solution, a Dirichlet condition must be applied to any one component of velocity on all boundaries. This condition is expressed as

$$\int_B \bar{u} \cdot \hat{n} \, dS = 0 \qquad (3.16)$$

The numerical problem requires the solution of Eq. (3.10) on each cell, Eq. (3.14) on each cell face, and Eq. (3.16) on all boundary cell faces. This can be solved by an iterative scheme due to Kaczmarz [48]. The resulting solution represents a least squares approximation to the system $A\bar{x} = \bar{F}$, where A is an nxm matrix and $\bar{x}$ and $\bar{F}$ are m and n dimensional vectors respectively. When applying this scheme to the system of equations given by Eq. (3.10) and (3.14), each equation is relaxed independently. Therefore, $n \equiv 1$, and m is equal to the number of unknowns in a cell. The scheme is derived in the following paragraph.

If R is a residual and (k) is a counter, then we can write:

$\bar{A}_i \bar{u}^{(k)} - F_i = R_i^{(k)}$ and $\bar{u}^{(k+1)} = \bar{u}^{(k)} + \bar{v}^{(k)}$, where $\bar{v}$ is a correction term.

$R_i^{(k+1)} = \bar{A}_i \cdot \bar{u}^{(k+1)} - F_i$ where i represents the specific equation to be relaxed.

$$R_i^{(K+1)} = \bar{A}_i (\bar{u}^{(k)} + \bar{v}^{(k)}) - F_i$$

$$= R_i^{(k)} + \bar{A}_i \bar{v}^{(k)}$$

choose $\qquad R_i^{(k+1)} = 0$

$$0 = R_i^{(k)} + \bar{A}_i \bar{v}^{(k)}; \text{ define } \bar{v}^{(k)} = A_i^T \bar{w}^{(k)}.$$

Then $\qquad \bar{A}_i \bar{A}_i^T \bar{w}^{(k)} = -R_i^{(k)}$

$$\bar{w}^{(k)} = -(\bar{A}_i \bar{A}_i^T)^{-1} R_i^{(k)}$$

$$\bar{v}^{(k)} = -A_i^T (\bar{A}_i \bar{A}_i^T)^{-1} R_i^{(k)}$$

$$\bar{u}^{(k+1)} = \bar{u}^{(k)} - \gamma \bar{A}_i^T (\bar{A}_i \bar{A}_i^T)^{-1} R_i^{(k)} \qquad (3.17)$$

An acceleration parameter γ has been introduced in Eq.(3.17). Expressions for $(\bar{A}\bar{A}^T)$ appear below for each of the required equations.

continuity $\qquad (\bar{A} \bar{A}^T)^{-1} = \dfrac{1}{8(1+\alpha^2+\beta^2)} \qquad (3.18)$

x vorticity $\qquad (\bar{A} \bar{A}^T)^{-1} = \dfrac{1}{4(1+\kappa^2)} \qquad (3.19)$

34

y-vorticity
$$(\bar{A}\ \bar{A}^T\ )^{-1} = \frac{1}{4(1+\beta^2)}$$
(3.20)

z-vorticity
$$(\bar{A}\ \bar{A}^T\ )^{-1} = \frac{1}{4(1+\alpha^2)}$$
(3.21)

where
$$\kappa = \Delta y/\Delta z$$
(3.22)

$$\beta = \Delta x/\Delta y$$
(3.23)

and
$$\alpha = \Delta x/\Delta z$$
(3.24)

For a Dirichlet type boundary condition

$$(\bar{A}\ \bar{A}^T\ )^{-1} = 1/4.$$
(3.25)

To implement the Neumann condition, $\partial u/\partial x = 0$ on a cell face, the continuity equation can be used to write

$$\partial v/\partial y + \partial w/\partial z = 0. \quad \text{Then}$$

$$(\bar{A}\ \bar{A}^T\ )^{-1} = .25/(1+\kappa^2)$$
(3.26)

In summary, a projection method due to Kaczmarz has been implemented to solve the overdetermined system given by Eqs. (3.1), (3.3) and (3.4). Tanabe [49] has shown that the method will converge for any system of linear equations with nonzero rows even if the system is singular.

Vorticity Equations

The discretized form of the vorticity transport equation is obtained by expressing the vorticity within a cell in terms of a set of basis functions. These functions are integrated over time and space resulting in expressions valid on cell faces. Appropriate combinations of these expressions result in the discretized form of the equations for

the transport of the vorticity. This procedure is detailed by McInville
[50].

The basis set employed by Gatski, Grosch, and Rose [51] for the
two-dimensional formulation is a solution to the one dimensional form of
the vorticity transport equation. These solutions are of the form

$$\omega(x,t;\alpha) = \exp\left[\alpha x - \beta(\alpha)t\right] \tag{3.27}$$

where $\qquad\qquad \beta(\alpha) = \alpha(u - \alpha v) \tag{3.28}$

The three-dimensional form of the vorticity transport equation
contains the vortex stretching term $\bar{\omega} \cdot \nabla \bar{u}$ which requires special
consideration. The basis set no longer represents solutions to the
three dimensional transport equation. Thus, Gatski, Grosch and Rose
[39] employed the transformation

$$\bar{\omega} = e^{\left[B_n \cdot (t-t_n)\right]}\bar{\zeta} \tag{3.29}$$

where $\bar{\omega}$ is the vorticity and $\bar{\zeta}$ is a transformed vorticity. Matrix $[B_n]$
is a 3x3 array which relates each component of $\bar{\omega}$ to the three components
of ζ. When applied to the vorticity transport equation, this
transformation eliminates the vortex stretching term. The resulting
transformed equation is

$$\frac{\partial \bar{\zeta}}{\partial t} + \bar{u} \cdot \nabla \bar{\zeta} = \nu \nabla^2 \bar{\zeta} \tag{3.30}$$

Details of the transformation appear in Appendix A. This form of the
transport equation has solutions of the type (3.27) and is the equation
to be discretized. Note that at time level n the transformed vorticity

36

equals the physical vorticity. Hence, "true" vorticity and "transformed" vorticity are equated at the beginning of each time step.

The discretized form of the transport equation has been derived in Gatski, Grosch and Rose [39]. It takes the form,

$$\{\delta_t + [(\mu_x u)\delta_x + (\mu_y v)\delta_y + (\mu_z w)\delta_z]\} \bar{\zeta}^n$$

$$= \nu (\delta_x \bar{\phi} + \delta_y \bar{\psi} + \delta_z \bar{\xi}) \qquad (3.31)$$

$$(\mu_x - h_x q_x \delta_x) \bar{\phi} = \delta_x \bar{\zeta}$$

$$(\mu_y - h_y q_y \delta_y) \bar{\psi} = \delta_y \bar{\zeta} \qquad (3.32\ a,b,c)$$

$$(\mu_z - h_z q_z \delta_z) \bar{\xi} = \delta_z \bar{\zeta}$$

$$\mu_t \bar{\zeta} = \mu_x \bar{\zeta} - h_x^2 p_x \delta_x \bar{\phi}$$

$$\mu_t \bar{\zeta} = \mu_y \bar{\zeta} - h_y^2 p_y \delta_y \bar{\psi} \qquad (3.33\ a,b,c)$$

$$\mu_t \bar{\zeta} = \mu_z \bar{\zeta} - h_z^2 p_z \delta_z \bar{\xi}$$

where,

$$\bar{\phi} = \frac{\partial \zeta_1}{\partial x} \hat{i} + \frac{\partial \zeta_2}{\partial x} \hat{j} + \frac{\partial \zeta_3}{\partial x} \hat{k} \qquad (3.34)$$

$$\bar{\psi} = \frac{\partial \zeta_1}{\partial y} \hat{i} + \frac{\partial \zeta_2}{\partial y} \hat{j} + \frac{\partial \zeta_3}{\partial y} \hat{k} \qquad (3.35)$$

$$\bar{\xi} = \frac{\partial \zeta_1}{\partial z} \hat{i} + \frac{\partial \zeta_2}{\partial z} \hat{j} + \frac{\partial \zeta_3}{\partial z} \hat{k} \qquad (3.36)$$

and $\quad q(\theta_{\ell}) = \coth (\theta_{\ell}) - \theta_{\ell}^{-1}; \quad \ell = 1,2,3$ $\qquad$ (3.37)

$$p(\theta_{\ell}) = q(\theta_{\ell})/\theta_{\ell} \qquad (3.37a)$$

$$\theta_{\ell} = \frac{u_{\ell}\Delta x_{\ell}}{2\nu} ; \quad \ell = 1,2,3 \qquad (3.38)$$

The finite difference operators δ and μ are defined as follows.

$$\delta_x S^n_{i,j,k} = \frac{S^n_{i+\frac{1}{2},j,k} - S^n_{i-\frac{1}{2},j,k}}{\Delta x} \qquad (3.39)$$

$$\delta_t S^n_{i,j,k} = \frac{S^{n+\frac{1}{2}}_{i,j,k} - S^{n-\frac{1}{2}}_{i,j,k}}{\Delta t} \qquad (3.40)$$

$$\mu_x S^n_{i,j,k} = \frac{S^n_{i+\frac{1}{2},j,k} + S^n_{i-\frac{1}{2},j,k}}{2} \qquad (3.41)$$

$$\mu_t S^n_{i,j,k} = \frac{S^{n+\frac{1}{2}}_{ijk} + S^{n-\frac{1}{2}}_{ijk}}{2} \qquad (3.42)$$

The algorithm governing the time advance of vorticity from time level n to level n+1 utilizes the vorticity at time level $n+\frac{1}{2}$ which is given by

$$\bar{\omega}^{n+\frac{1}{2}} = e^{B_n(t_{n+\frac{1}{2}} - t_n)} \bar{\zeta}^{n+\frac{1}{2}} \qquad (3.43)$$

By definition

$$\bar{\zeta}^{n+\frac{1}{2}} = (\mu_t + \tau\delta_t)\bar{\zeta}^n \qquad (3.44)$$

Thus

$$\bar{\omega}^{n+1/2} = e^{B_n(t_{n+1/2} - t_n)} (\mu_t + \tau\delta_t)\bar{\zeta}^n \tag{3.45}$$

Now consider the vorticity at time level $n+\frac{1}{2}$ centered around level $n+1$.

$$\bar{\omega}^{n+1/2} = e^{-B_{n+1}(t_{n+1} - t_{n+1/2})}\bar{\zeta}^{n+1/2} \tag{3.46}$$

By definition

$$\bar{\zeta}^{n+1/2} = (\mu_t - \tau'\delta_t)\bar{\zeta}^{n+1} \tag{3.47}$$

Thus,

$$\bar{\omega}^{n+1/2} = e^{-B_{n+1}(t_{n+1} - t_{n+1/2})}(\mu_t - \tau'\delta_t)\bar{\zeta}^{n+1} \tag{3.48}$$

By equating Eqs. (3.45) and (3.48) the condition that the vorticity at time level $n+\frac{1}{2}$ be continuous is imposed. This results in a relationship between the vorticity at time level $n+1$ and level n. This condition is given as:

$$(\mu_t - \tau'\delta_t)\,\bar{\zeta}^{n+1} = e^{B_{n+1}\tau'}[e^{B_n\tau}(\mu_t + \tau\delta_t)\,\bar{\zeta}^n] \tag{3.49}$$

where $\qquad \tau' = t_{n+1} - t_{n+1/2}$ $\qquad\qquad\qquad$ (3.50)

and $\qquad \tau = t_{n+1/2} - t_n$ $\qquad\qquad\qquad$ (3.51)

Equation (3.49) governs the advance of vorticity from time level n to level $n+1$. If it is assumed that the vorticity field is known at time level n, then the right hand side of Eq. (3.49) can be calculated explicitly. The time average on the right hand side is expanded by using Eqs. (3.33 a,b,c). The time difference is expanded by using the

transport equation (Eq. (3.31)). These expansions remove the $n+\frac{1}{2}$ time level from the right hand side of Eq. (3.49). The expanded forms of Eq. (3.49) using Eq. (3.31) and Eq. (3.33a) (3.33b) or (3.33c) respectively, become:

$$(\mu_t - \tau'\delta_t)\bar{\zeta}^{\,n+1} = e^{B_{n+1}\tau'}e^{B_n\tau}[\mu_x\bar{\zeta}^{\,n} - \tau[\mu_x u\delta_x\bar{\zeta}^{\,n} + \mu_y v\delta_y\bar{\zeta}^{\,n} + \mu_z w\delta_z\bar{\zeta}^{\,n}]$$

$$+ \nu\tau(\delta_x\bar{\phi} + \delta_y\bar{\psi} + \delta_z\bar{\xi}) - h_x^2 p_x\delta_x\bar{\phi}^{\,n}] \qquad (3.52)$$

$$(\mu_t - \tau'\delta_t)\bar{\zeta}^{\,n+1} = e^{B_{n+1}\tau'}e^{B_n\tau}[\mu_y\bar{\zeta}^{\,n} - \tau[\mu_x u\delta_x\bar{\zeta}^{\,n} + \mu_y v\delta_y\bar{\zeta}^{\,n} + \mu_z w\delta_z\bar{\zeta}^{\,n}]$$

$$+ \nu\tau(\delta_x\bar{\phi} + \delta_y\bar{\psi} + \delta_z\bar{\xi}) - h_y^2 p_y\delta_y\bar{\psi}^{\,n}] \qquad (3.53)$$

$$(\mu_t - \tau'\delta_t)\bar{\zeta}^{\,n+1} = e^{B_{n+1}\tau'}e^{B_n\tau}[\mu_z\bar{\zeta}^{\,n} - \tau[\mu_x u\delta_x\bar{\zeta}^{\,n} + \mu_y v\delta_y\bar{\zeta}^{\,n} + \mu_z w\delta_z\bar{\zeta}^{\,n}]$$

$$+ \nu\tau(\delta_x\bar{\phi} + \delta_y\bar{\psi} + \delta_z\bar{\xi}) - h_z^2 p_z\delta_z\bar{\xi}^{\,n}] \qquad (3.54)$$

The only unknowns on the right hand side in these equations are the diffusion terms $\delta_x\bar{\phi}$, $\delta_y\bar{\psi}$, and $\delta_z\bar{\xi}$. Explicit expressions for these terms are obtained from a set of equations, derived from the identity $\bar{\zeta}^{\,n-\frac{1}{2}} = \mu_t\bar{\zeta}^{\,n} - \tau\delta_t\bar{\zeta}^{\,n}$ where $\bar{\zeta}^{\,n-\frac{1}{2}}$ is known from the previous time step. This identity is expanded using Eq. (3.31) and Eqs. (3.33 a,b,c). The three resulting sets of equations become

$$\bar{\zeta}^{\,n-\frac{1}{2}} = \mu_x\bar{\zeta}^{\,n} + \tau(\mu_x u\delta_x\bar{\zeta}^{\,n} + \mu_y v\delta_y\bar{\zeta}^{\,n} + \mu_z w\delta_z\bar{\zeta}^{\,n}) - (h_x^2 p_x + \nu\tau)\delta_x\bar{\phi} - \nu\tau\delta_y\bar{\psi} - \nu\tau\delta_z\bar{\xi} \qquad (3.55)$$

$$\bar{\zeta}_y^{n-\frac{1}{2}} = \mu_y \bar{\zeta}^n + \tau(\mu_x u \delta_x \bar{\zeta}^n + \mu_y v \delta_y \bar{\zeta}^n + \mu_z w \delta_z \bar{\zeta}^n) - \nu\tau\delta_x \bar{\phi} - (h_y^2 p_y + \nu\tau)\delta_y \bar{\psi} - \nu\tau\delta_z \bar{\xi} \quad (3.56)$$

$$\bar{\zeta}_z^{n-\frac{1}{2}} = \mu_z \bar{\zeta}^n + \tau(\mu_x u \delta_x \bar{\zeta}^n + \mu_y v \delta_y \bar{\zeta}^n + \mu_z w \delta_z \bar{\zeta}^n) - \nu\tau\delta_x \bar{\phi} - \nu\tau\delta_y \bar{\psi} - (h_z^2 p_z + \nu\tau)\delta_z \bar{\xi} \quad (3.57)$$

Note that the i component of the above equations represents one "set," consisting of 3 scalar equations with unknowns $\delta_x \phi_1$, $\delta_y \psi_1$ and $\delta_z \xi_1$. Similarly for the j and k components.

The details of the solution of these equations for $\delta_x \bar{\phi}$, $\delta_y \bar{\psi}$, $\delta_z \bar{\xi}$ by utilizing Eqs. (3.32 a,b,c), appears in Appendix B. The advance to time level n+1 is implicit. Equations (3.52), (3.53) and (3.54) are reduced to a tridiagonal system which can be solved using either alternating direction implicit (ADI) or successive over relaxation (SOR) methods. The reduction of the equations to tridiagonal form has been developed in Appendix B.

To implement an ADI solution, a Thomas algorithm [52] is first applied along each line of constant jk for the x direction sweep. This gives the three components of vorticity at the centers of the x=constant cell faces. Explicit in this sweep are the three components of vorticity occurring on the y=constant and the z=constant faces. For the first iteration through x direction sweeps, the values of the vorticity components are at time level n. The Thomas algorithm is then applied in the y direction and z direction, resulting in the updated components of vorticity on the y=constant and z=constant faces respectively. In general, it is found that sufficient refinement of the solution is achieved by cycling through each sweep direction three times.

Recall that the velocity coefficients of the advection terms are lagged by one time level during these cycles. To achieve second order accuracy in time it is necessary to update these velocities to the current time level of the vorticity, and then recompute the vorticity using these updated velocities. It is also necessary to recompute the right hand side of Eq. (3.49) after recycling through the velocity equations and before recomputing the vorticity. This requirement results from the fact that the n+1 time level of the exponential transformation appears in Eq. (3.49). Repeated application of the above procedure yields in the vorticity and velocity fields at later times.

Alternately, the implicit system may be solved using a SOR type iteration scheme instead of applying the Thomas algorithm along lines. The advantage of this approach is that when only a few cycles are required, the SOR iteration will be faster computationally. In addition, a residual can be identified and used as a criterion for convergence. The residual is defined as the difference between the left side and right side of each individual equation of the tridiagonal system. The other aspects of the solution procedure are identical with the method employing the Thomas algorithm. In all the subsequent computations, the time steps were kept small enough to ensure that the CFL stability criterion [53] was not violated.

Helmholtz Projection

In general, the vorticity resulting from the finite difference solution to the vorticity transport equations does not satisfy the requirement that the vorticity vector be divergence free. This is due to the fact that the divergence free condition is a vector identity and

42

is not part of the Navier-Stokes equations. Hence, the divergence free condition is not required in the derivation of the vorticity transport equation. Thus, an initially divergence free field may drift from the requirement due to roundoff error or discretization error.

A previously discussed requirement for the numerical solution of the velocity field was the compatibility condition $\nabla \cdot \bar{\omega} = 0$. If the vector resulting from the time advance of the transport equation does not satisfy this condition, it must be projected onto the vector space of divergence free vorticity. A well known property of any vector field is the fact that it can be decomposed into an irrotational field and a divergence free field according to the Helmholtz projection:

$$\bar{\omega} = \bar{\nabla}\chi + \bar{\nabla} \times \bar{c} \qquad (3.58)$$
$$\text{irrotational} \qquad \text{divergence free}$$

Here, χ represents a scalar function and $\bar{c}$, a vector function. To extract the divergence free part of the vector, $\bar{\omega}$, take the divergence of Eq. (3.58) to get:

$$\nabla \cdot \bar{\omega} = \nabla^2 \chi \qquad (3.59)$$

Equation (3.61) can be used to solve for χ, subject to the boundary condition $\frac{\partial \chi}{\partial n} = 0$ on B. This boundary condition is utilized to ensure that the component of vorticity normal to the boundary is not altered. The divergence free component, $\bar{\nabla} \times \bar{c}$, of the original vector, $\bar{\omega}$, is given by

$$\bar{\nabla} \times \bar{c} = \bar{\omega} - \bar{\nabla}\chi \qquad (3.60)$$

An alternate approach to enforcing the solenoidal condition on the vorticity vector can also be derived. Equation (3.59) can be reduced to the following set of first order differential equations:

$$\frac{\partial p}{\partial x} + \frac{\partial q}{\partial y} + \frac{\partial r}{\partial z} = \bar{\nabla} \cdot \bar{\omega} \tag{3.61}$$

$$p = \frac{\partial \chi}{\partial x} \tag{3.62}$$

$$q = \frac{\partial \chi}{\partial y} \tag{3.63}$$

$$r = \frac{\partial \chi}{\partial z} \tag{3.64}$$

where $\frac{\partial \chi}{\partial n} = 0$ on the boundary. The unknowns in this system are the scalar quantities p, q, r and χ. The divergence free components of the original vector are then given by:

$$(\bar{\nabla} \times \bar{c})_1 = \omega_1 - p \tag{3.65}$$

$$(\bar{\nabla} \times \bar{c})_2 = \omega_2 - q \tag{3.66}$$

$$(\bar{\nabla} \times \bar{c})_3 = \omega_3 - r. \tag{3.67}$$

The discretization of equations (3.61) to (3.64) is described by Rose [54]. The finite difference forms are:

$$\delta_x p + \delta_y q + \delta_z r = \bar{\nabla} \cdot \bar{\omega} \tag{3.68}$$

$$\mu_x p = \delta_x \chi \tag{3.69}$$

$$\mu_y q = \delta_y \chi \tag{3.70}$$

$$\mu_z r = \delta_z \chi \tag{3.71}$$

$$\mu_x \chi - \frac{\Delta x^2}{3} \delta_x p = \mu_y \chi - \frac{\Delta y^2}{3} \delta_y q \qquad (3.72)$$

$$\mu_x \chi - \frac{\Delta x^2}{3} \delta_x p = \mu_z \chi - \frac{\Delta z^2}{3} \delta_z r \qquad (3.73)$$

The averaging and difference operators are identical to those defined previously for the discretization of the transport equation.

These equations have been solved using the Kaczmarz [48] iteration scheme which was discussed in reference to the solution of the velocity field. Recall that the Kaczmarz scheme requires the evaluation of the expression $\bar{A}_i^T (\bar{A}_i \bar{A}_i^T)^{-1} R_i$ for each of the discretized equations, the subscript i denoting a specific equation. The expressions for $\bar{A}_i$ and R_i are given below for Eqs. (3.68) to (3.71) as Eqs. (3.74 a,b) to (3.80 a,b) respectively.

$$A_1 = (\frac{1}{\Delta x}, \frac{-1}{\Delta x}, \frac{1}{\Delta y}, \frac{-1}{\Delta y}, \frac{1}{\Delta z}, \frac{-1}{\Delta z}) \qquad (3.74a)$$

$$R_1 = \frac{1}{\Delta x} (p_{i+1/2} - p_{i-1/2}) + \frac{1}{\Delta y} (q_{j+1/2} - q_{j-1/2})$$

$$+ \frac{1}{\Delta z} (r_{k+1/2} - r_{k-1/2}) - (\nabla \cdot \bar{\omega})_{i,j,k} \qquad (3.74b)$$

$$A_2 = (\frac{1}{2}, \frac{1}{2}, \frac{-1}{\Delta x}, \frac{1}{\Delta x}) \qquad (3.75a)$$

$$R_2 = \frac{1}{2} (p_{1+1/2} + p_{i-1/2}) - \frac{1}{\Delta x} (\chi_{i+1/2} - \chi_{i-1/2}) \qquad (3.75b)$$

$$A_3 = (\frac{1}{2}, \frac{1}{2}, \frac{-1}{\Delta y}, \frac{1}{\Delta y}) \qquad (3.76a)$$

$$R_3 = \frac{1}{2} (q_{j+1/2} + q_{j-1/2}) - \frac{1}{\Delta y} (x_{j+1/2} - x_{j-1/2}) \qquad (3.76b)$$

$$A_4 = (\frac{1}{2}, \frac{1}{2}, \frac{-1}{\Delta z}, \frac{1}{\Delta z}) \qquad (3.77a)$$

$$R_4 = \frac{1}{2} (r_{k+1/2} + r_{k-1/2}) - \frac{1}{\Delta z} (x_{k+1/2} - x_{k-1/2}) \qquad (3.77b)$$

$$A_5 = (\frac{1}{2}, \frac{1}{2}, -\frac{1}{2}, -\frac{1}{2}, \frac{-\Delta x}{8}, \frac{\Delta x}{8}, \frac{\Delta y}{8}, \frac{-\Delta y}{8}) \qquad (3.78a)$$

$$R_5 = \frac{1}{2} (x_{i+1/2} + x_{i-1/2}) - \frac{1}{2} (x_{j+1/2} + x_{j-1/2})$$

$$- \frac{\Delta x^2}{8} (p_{i+1/2} - p_{i-1/2}) + \frac{\Delta y^2}{8} (q_{j+1/2} - q_{j-1/2}) \quad (3.78b)$$

$$A_6 = (\frac{1}{2}, \frac{1}{2}, -\frac{1}{2}, -\frac{1}{2}, -\frac{\Delta x}{8}, \frac{\Delta x}{8}, \frac{\Delta z}{8}, -\frac{\Delta z}{8}) \qquad (3.79a)$$

$$R_6 = \frac{1}{2} (x_{i+1/2} + x_{i-1/2}) - \frac{1}{2} (x_{k+1/2} + x_{k-1/2})$$

$$- \frac{\Delta x^2}{8} (p_{i+1/2} - p_{i-1/2}) + \frac{\Delta z^2}{8} (r_{k+1/2} - r_{k-1/2}) \quad (3.79b)$$

Each of the above equations is relaxed independently over all interior and boundary cells using the Kaczmarz iteration scheme repeated below.

$$\bar{\pi}_i^{(k+1)} = \bar{\pi}_i^{(k)} - \gamma \bar{A}_i^T (\bar{A}_i \bar{A}_i^T)^{-1} R_i^{(k)} \qquad (3.80)$$

The vector $\bar{\pi}$ is composed of combinations of the variables p,q,r, and χ depending on the equation being relaxed. For instance, when i=1, which corresponds to Eq. (3.68) the vector $\bar{\pi}$, is given by

$$\bar{\pi}_1 = (p_{i+\frac{1}{2}}, \ p_{i-\frac{1}{2}}, \ q_{j+\frac{1}{2}}, \ q_{j-\frac{1}{2}}, \ r_{k+\frac{1}{2}}, \ r_{k-\frac{1}{2}},) \qquad (3.81)$$

The boundary conditions are handled in a similar manner. It is required that the normal component of vorticity on a boundary remain unchanged after the Helmholtz projection. Thus, on constant x boundary faces $\frac{\partial \chi}{\partial x}$ = 0, on constant y boundary faces, $\frac{\partial \chi}{\partial y}$ = 0, and on constant z boundary face, $\frac{\partial \chi}{\partial z}$ = 0. Hence, the boundary conditions are

$$p = 0 \qquad \text{on } i=1, \text{ and } imax \qquad (3.82)$$

$$q = 0 \qquad \text{on } j=1, \text{ and } jmax \qquad (3.83)$$

$$r = 0 \qquad \text{on } k=1, \text{ amd } kmax \qquad (3.84)$$

These values are reset after each iteration through the Kaczmarz update, since in general, the boundary values of p,q and r change after the relaxation of Eqs. (3.68) to (3.73).

An alternate method, mentioned initially, is to solve the Poisson equation for χ, and then compute $\nabla\chi$. This can be done using an SOR iteration scheme. The divergence of vorticity is given at the center of a cell, so that χ should be computed at cell centers while $\nabla\chi$ should be computed at cell faces. To facilitate coding, it is desirable to express the Poisson equation in terms of the orthogonal, curvilinear coordinates

$$x = x \ (\xi)$$
$$y = y \ (\eta)$$
$$z = z \ (\zeta)$$

The transformed Poisson equation takes the form

$$\xi_x^2 \, \chi_{\xi\xi} + \eta_y^2 \, \chi_{\eta\eta} + \zeta_z^2 \, \chi_{\zeta\zeta} = \xi_x \frac{\partial \omega_1}{\partial \xi} + \eta_y \frac{\partial \omega_2}{\partial \eta} + \zeta_z \frac{\partial \omega_3}{\partial \zeta} \qquad (3.88)$$

where

$$0 < \xi < 1, \qquad 0 < \eta < 1, \qquad 0 < \zeta < 1$$

The computational plane consists of rectangular cells with uniform spacing in each coordinate direction. This allows one to use simple unweighted finite difference expressions. Equation (3.85) is discretized using central differences for both first and second order derivatives. The discretized form can be solved using an SOR scheme for the variable χ . It is then necessary to compute $\nabla\chi$ as follows.

$$\nabla\chi = \xi_x \frac{\partial \chi}{\partial \xi} \hat{i} + \eta_y \frac{\partial \chi}{\partial \eta} \hat{j} + \zeta_z \frac{\partial \chi}{\partial \zeta} \hat{k} \qquad (3.86)$$

In the discretized form, the first order derivatives are represented by central differences. On boundaries, $\partial\chi/\partial n = 0$, so Eq. (3.86) is computed for interior cells only. If the divergence free components are represented by "'", then

$$\omega'_1 = \omega_1 - \partial\chi/\partial x \qquad (3.87)$$

$$\omega'_2 = \omega_2 - \partial\chi/\partial y \qquad (3.87b)$$

$$\omega'_3 = \omega_3 - \partial\chi/\partial z \qquad (3.87c)$$

Pressure Equations

One advantage of the vorticity-velocity formulation is that the pressure does not appear explicitly in the equations of motion. Therefore, the velocity and vorticity are obtained independent from the

48

pressure field. In Appendix C, it is shown that pressure satisfies a Poisson equation, whose right hand or function side is an expression containing the velocity gradients. The numerical solution of this equation is analagous to the solution of the Poisson equation, Eq. (3.59).

Neumann conditions, resulting from the momentum equations, were specified on all boundaries. A special requirement of these boundary conditions, due to an application of Green's theorem, is discussed below.

The integral form of the Poisson equation for pressure can be developed from the momentum equations and written as:

$$\int \nabla^2 P \, dV = \int S dv \qquad (3.88)$$

where the source term S is given as

$$S = -2\rho \left[\frac{\partial v}{\partial x} \frac{\partial u}{\partial y} + \frac{\partial w}{\partial x} \frac{\partial u}{\partial z} + \frac{\partial w}{\partial y} \frac{\partial v}{\partial z} - \frac{\partial u}{\partial x} \frac{\partial v}{\partial y} - \frac{\partial u}{\partial x} \frac{\partial w}{\partial z} - \frac{\partial v}{\partial y} \frac{\partial w}{\partial z} \right] \qquad (3.89)$$

Through an application of Green's theorem, a relationship between the source term and the boundary flux is given as:

$$\int S dV = \int \frac{\partial P}{\partial n} \, \partial\sigma \qquad (3.90)$$

Here, n is taken as positive when directed outward from the boundary σ. In general, the finite difference equivalent of Eq. (3.90) will not be satisfied identically. As a result, the numerical solution of the Poisson equation for pressure need not converge.

A convergence requirement can be developed for the Poisson equation by imposing an error condition, E, defined as

$$E = \int S dV - \int \frac{\partial P}{\partial n} \, \partial\sigma \qquad (3.91)$$

49

The strategy is to distribute this error over the boundary flux terms $\partial P/\partial n$, which represent the boundary conditions. In this sense, the finite difference analog of Eq. (3.90) is satisfied.

SPECIFICATION OF THE PROBLEM -
BOUNDARY CONDITIONS

Mathematically, the Navier-Stokes equations are a set of three elliptic, second order partial differential equations. This means that either a Dirichlet or Neumann condition must be specified on all closed boundaries. It is these boundary conditions that distinguish all the different flow patterns occurring in nature. Therefore, it is extremely important that these conditions be chosen properly.

The purpose of the present study was to model the evolution of a class of vortices similar to those shed from the wing tips of aircraft. Although these vortices generally occur in pairs, only a single vortex was considered. Observations reveal that these vortices are roughly axisymmetric with an appreciable axial velocity (either a defect or an excess velocity relative to the free stream, depending on the wing loading [55]). In addition, far downstream of the wing the flow outside of the core is nearly irrotational.

Experimental measurements of a trailing wing tip vortex [42] and vortices produced in a tube and vane apparatus [27] revealed that the circumferential velocity profile is well represented by the two-dimensional Burgers vortex. The axial velocity appears to decay exponentially in the radial direction (from the vortex centerline), reaching a constant value at large radius. These observations can be represented by the following dimensional form for the swirl and axial velocity profiles.

$$v_e = (K/r)(1-e^{\frac{-ar^2}{2\nu}}) \tag{4.1}$$

$$u = U_\infty + U_o e^{\frac{-ar^2}{2\nu}} \tag{4.2}$$

Here, K is a constant, which is proportional to the circulation, "a" is an adjustable constant associated with the vortex core diameter and ν is the kinematic viscosity. U_∞ is the free stream axial velocity and U_o is an axial velocity excess (or deficit) occurring at the vortex center-line. Profiles similar to these were employed in numerical studies of vortex breakdown by Kopecky and Torrance [31] and Benay [35].

In the above equations, length was nondimensionalized by r', where

$$r' = \sqrt{2\nu/a} \tag{4.3}$$

and velocities were nondimensionalized by the axial velocity, U^*, occurring at the radius of maximum swirl velocity, r^*. Formally, the quantity r' is the distance in which the axial vorticity e-folds once. In fact, the radius of maximum swirl velocity is nearly equal to r^*. Through an iterative process one obtains the relation

$$r^* = 1.12 \, r' \tag{4.4}$$

The nondimensional forms of Eqs. (4.1) and (4.2) become

$$v_\theta = \frac{1}{1.12 \, Ro} \frac{1}{r} (1-e^{-r^2}) \tag{4.5}$$

$$u = \frac{1 + \bar{\delta}e^{-r^2}}{1 + 0.285\bar{\delta}} \tag{4.6}$$

52

where the Rossby number is given as $Ro = U^*/r^*\Omega$ and $\bar{\delta} = U_0/U_\infty$. Here, Ω is defined as the solid body rotation rate obtained from

$$\Omega = \lim_{r \to o} (V/r) = aK/2\nu. \tag{4.7}$$

The axial component of vorticity, for the velocity distribution given by Eqs. (4.1) and (4.2), is given as

$$\omega_x = \frac{aK}{\nu} e^{\frac{-ar^2}{2\nu}}. \tag{4.8}$$

By defining Ω as the reference vorticity, the above equation can be written in nondimensional form as

$$\omega_x = 2 \, e^{-r^2} \tag{4.9}$$

The circumferential vorticity component is given as

$$\omega_\theta = \frac{ar}{\nu} U_0 e^{\frac{-ar^2}{2\nu}} \tag{4.10}$$

which in nondimensional form becomes:

$$\omega_\theta = \frac{2.24\bar{\delta}}{1.0 + 0.285\bar{\delta}} \, Ro \, re^{-r^2} \tag{4.11}$$

These expressions represent the form of the vortex employed in the present study from which the initial and boundary conditions were derived. The initial and boundary conditions at inflow are discussed first, followed by the outflow conditions and conditions at large radius.

The specification of the velocity vector, Eq. (3.3), or its gradient on all closed boundaries is required to solve the primitive variable form of the Navier-Stokes equations, Eq. (3.2). The numerical solution of the vorticity transport equation, Eq. (3.5), requires the

specification of three components of vorticity on the boundaries. The numerical solution of the "velocity equations", Eqs. (3.1) and (3.4), requires the specification of a single component of the velocity vector (or gradient) on the boundaries. The general procedure is to specify the primitive variables on a boundary and translate this specification to a finite difference form consistent with the above requirements of the algorithm.

Although quasi-cylindrical vortices are best described in a cylindrical coordinate system, the algorithm, as constructed at this point, was written in terms of Cartesian coordinates. Therefore, references to both coordinate systems are required in order to interpret the influence of the boundary conditions on the solution. In the following discussion it is assumed that the initial vortical distribution was cylindrical (i.e., no variations in the axial direction and no radial velocities). The vortex was aligned along the x axis and the rotation was such that the axial component of vorticity was positive.

At inflow, the specified primitive variables were: the axial velocity component, u, the y derivative of the w, and the z derivative of the v components of velocity, (i. e. u, $\frac{\partial v}{\partial z}$, $\frac{\partial w}{\partial y}$). These conditions must be interpreted with respect to the algorithm. The axial velocity component, u, was held fixed at inflow when solving the "velocity equations." This allowed for direct specification of wake-like or jet-like profiles. The v and w components of velocity were specified to the extent that they took on the values determined by the component of vorticity normal to the inflow boundary. This led to the specification of $\partial w/\partial y$ and $\partial v/\partial z$ as the additional primitive variable boundary

54

conditions, since these derivatives can be combined to give the axial component of vorticity. Note further that the axial component of vorticity can be oriented in the same direction in both cylindrical and Cartesian coordinate systems. Therefore, the specification of ω_x in the Cartesian coordinate system (of the algorithm) can be interpreted as specifying the vorticity distribution of Burgers' vortex, since $\partial w/\partial y$ and $\partial v/\partial z$ were obtained analytically from Eq. (4.5).

The "vorticity solver" required the specification of two additional boundary conditions. These were chosen as ω_y and ω_z.

In nondimensional form, ω_y and ω_z can be written:

$$\omega_y = 1.12 \text{ Ro } \left(\frac{\partial u}{\partial z} - \frac{\partial w}{\partial x}\right) \tag{4.12}$$

$$\omega_z = 1.12 \text{ Ro } \left(\frac{\partial v}{\partial x} - \frac{\partial u}{\partial y}\right) \tag{4.13}$$

Since u is an analytic boundary condition at inflow, the derivatives $\partial u/\partial z$ and $\partial u/\partial y$ were known. It was necessary to calculate the derivatives $\partial w/\partial x$ and $\partial v/\partial x$ numerically since they could not be derived from the analytic boundary conditions. First order forward differences were used to compute these derivatives. The resulting boundary conditions were assumed to be at time level n (present time).

A different strategy had to be used to specify the outflow boundary conditions since the solution here was unknown and highly dependent on the flow upstream. With respect to the "velocity solver", the condition

$$\partial v/\partial y + \partial w/\partial z = \text{constant} \tag{4.14}$$

was chosen. This is a statement regarding the divergence of the velocity in the plane perpendicular to the vortex axis. The constant

55

equals zero for a steady flow in the limit as the Rossby number approaches zero [40].

Flux conditions were chosen for the vorticity boundary conditions at outflow. Here, the effects of viscosity were neglected and the Dirichlet type boundary conditions were obtained assuming a time advance of

$$\frac{D\bar{\omega}}{Dt} = \bar{\omega} \cdot \nabla \bar{u}. \tag{4.15}$$

The velocities and vorticities on the right hand side. of Eq. (4.15) were taken at time level n. The time derivative was discretized using first order forward differences. The resulting discretized equation was then solved for the vorticity vector at time level n+1.

At the large radius boundaries given by planes of constant j and k, the axial component of velocity was specified. This was done so that the effects of an external pressure gradient, analagous to the experimental investigations, could be modeled.

At these boundaries the three components of vorticity were specified using the Cartesian coordinate equivalents of Eqs. (4.9) and (4.11). For a uniform inflow profile, Eq. (4.11) shows the ω_y and ω_z components of vorticity are zero. By evaluating Eq. (4.11) at large radius, one can see that the axial component approaches zero asymptotically. Therefore, the radial boundaries were placed at a radius which was large enough to ensure that vorticity did not, through convection or diffusion, contaminate the boundary conditions.

To summarize, the specification of the boundary conditions for both the "velocity solver" and the "vorticity solver" are represented in Table 4.1.

Table 4.1

Summary of Velocity and Vorticity Boundary Conditions

Velocity Solver

	Surface	Specification
(a)	inflow	$u = \text{given}$
(b)	outflow	$\partial v/\partial y + \partial w/\partial z = 0$
(c)	radial boundaries	$u = \text{given.}$

Vorticity Solver

	Surface	Specification
(a)	inflow	$\omega_x = 2\, e^{-r^2}$
		$\omega_y = 1.12\ \text{Ro}\ (\partial u/\partial z - \partial w/\partial x)$
		$\omega_z = 1.12\ \text{Ro}\ (\partial v/\partial x - \partial u/\partial y)$
(b)	outflow	$\dfrac{D\bar{\omega}}{Dt} = \bar{u}\cdot\nabla\bar{\omega}$
(c)	radial boundaries	$\bar{\omega} = \text{given}$

The discretized form of the governing equations were solved over a 48x28x28 grid (47 cells in the x-direction, 27 cells in the y-direction, 27 cells in the z-direction) on a Cyber 205. Course grid (52x20x20) solutions were computed on a CDC 830 at Old Dominion University to help identify relevant parameter ranges. Since the difference scheme is compact, grid clustering is easily performed. Grid points are usually clustered in regions where large gradients occur. In studies of vortex breakdown, this includes the region immediately upstream of the breakdown and the vortex core region. Immediately upstream of breakdown, large gradients of the axial velocity occur as the fluid approaches the stagnation point. Large gradients of the circumferential velocity are present within the core.

Refinement of the mesh in the axial direction was accomplished using the transformation:

$$x = \frac{\bar{h}_x (\sigma^2 - 1) \left[(\frac{\beta+1}{\beta-1})^{\bar{x}-1} - 1 \right]}{(\sigma+1) \left[(\frac{\sigma+1}{\sigma-1})^{\bar{x}-1} + 1 \right]} \qquad (4.16)$$

where β is a stretching parameter and $\bar{h}_x$ is the length of the domain in the x direction. More points are clustered near x=0 as $\sigma \to 1$, $1 < \sigma < \infty$. The coordinate $\bar{x}$ varies uniformly from 0 (corresponding to the x=0 grid point) to 1 (corresponding to the $x = \bar{h}_x$ grid point).

To cluster points near the vortex centerline (y and z coordinates) the following transformation was used:

$$y = y_c \{1 + \frac{\sinh[\epsilon(\bar{y}-\beta)]}{\sinh(\epsilon\beta)}\} \qquad (4.17)$$

where

$$B = \frac{1}{2\varepsilon} \ln \left[\frac{1 + (e^{\varepsilon}-1)(y_c/\bar{h}_y)}{1 + (e^{-\varepsilon}-1)(y_c/\bar{h}_y)} \right], \quad 0<\varepsilon<\infty \qquad (4.18)$$

and ε is a stretching parameter. Increasing ε clusters more points near $y=y_c$. If $\varepsilon=0$, a uniformly spaced grid results. The domain length is given by $\bar{h}_y$. The coordinate $\bar{y}$ varies uniformly from 0 (corresponding to the y=0.0 gridpoint) to 1 (corresponding to the $y=\bar{h}_y$ gridpoint).

The above transformations can be found in Anderson, Tannehill and Pletcher [52]. The values of the grid parameters for the solutions generated in this work were given as:

$\bar{h}_x = 16.0, \; \sigma = 1.15$ x direction grid

$y_c = 5.0, \; \bar{h}_y = 10.0, \; \varepsilon = 4.5$ y direction grid

$z_c = 5.0, \; \bar{h}_z = 10.0, \; \varepsilon = 4.5$ z direction grid

These resulted in the following minimum cell lengths:

$$\Delta x = 0.1303$$

$$\Delta y = 0.1778$$

$$\Delta z = 0.1778.$$

The distribution of the cells within the domain and the orientation of a typical vortex is shown in Fig. 4.1.
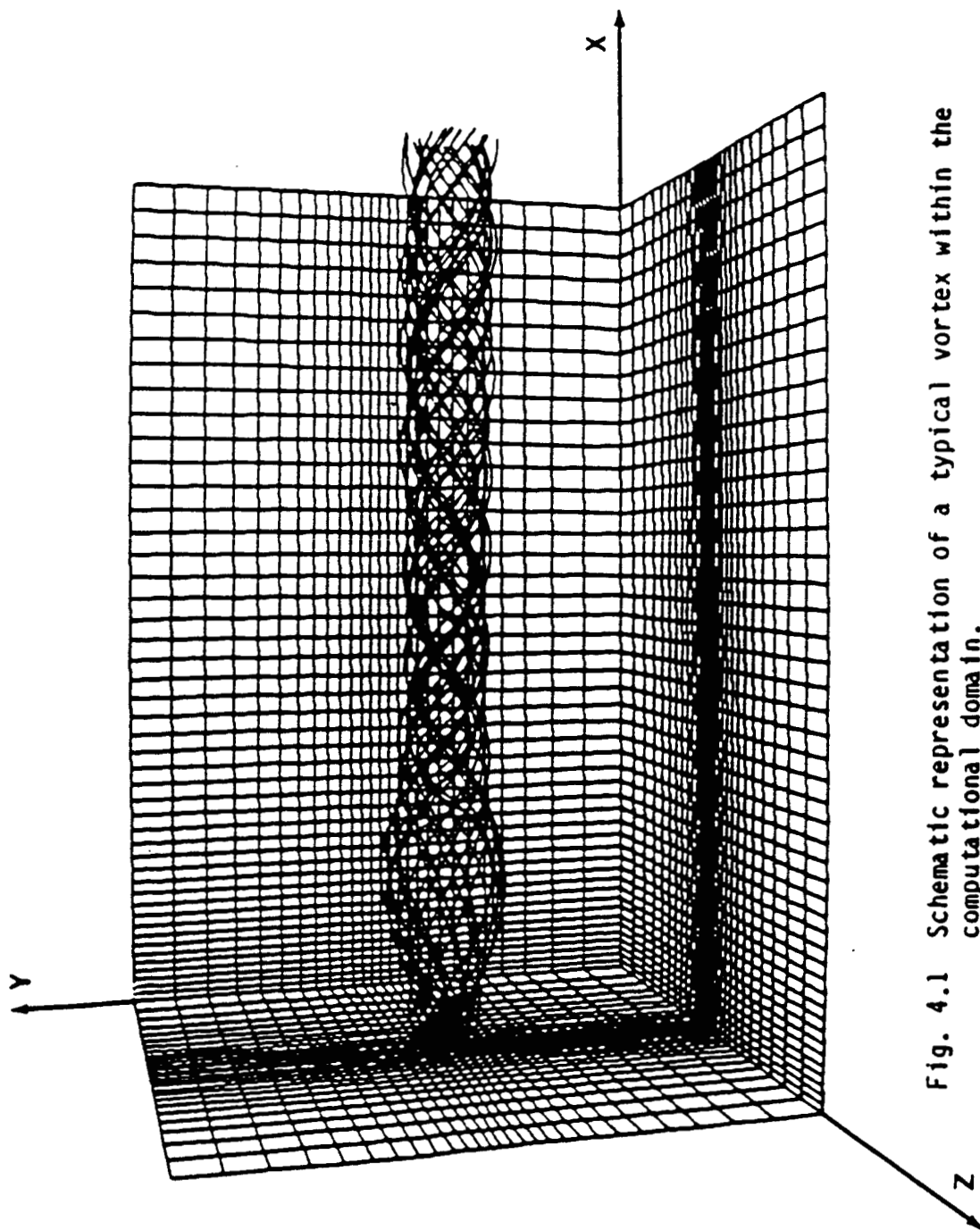
Fig. 4.1 Schematic representation of a typical vortex within the computational domain.

RESULTS AND DISCUSSION

Results of two test cases are presented. In the first case, (Ro=0.625, Re=225), the vortex was imbedded in a uniform external flow with no external pressure gradient. The flow produced by this Rossby, Reynolds number case, along with numerous other cases, predicted an axisymmetric breakdown which occurred at the inflow boundary. That result was similar to the results obtained by previous investigators [31,33,35,36]. The questions which arise from breakdown near inflow have been discussed earlier in this work. In order to alleviate this problem, a different type flow was computed, (Ro=0.8, Re=225), in which the vortex was imbedded in a decelerating free stream. This, in essence, modeled the effects of an adverse pressure gradient on the streamwise development of the vortex. The resulting breakdown occurred away from the inflow boundary. In addition, a multiple celled breakdown region was observed, in accord with experimental observations [27]. In both cases, the parameter, $\bar{\delta}$, defined in Eq. (4.6), equaled 0.0. Thus, a uniform axial velocity profile was specified at inflow. In the following discussion, detailed results of the above two test cases are displayed in the form of line and contour plots. Several other test cases that were run without graphic output are discussed. Finally, the results of tests performed to ascertain the effects of domain length and grid size on the temporal evolution of the solution are discussed.

61

Case 1 - Uniform Free Stream Axial Velocity

Based on previous numerical studies, breakdown of trailing wing tip vortices occurred at Rossby numbers of approximately 0.6 or less when the Reynolds number was greater than 100. This behavior is shown clearly in Fig. 2.1. The initial numerical simulation in the present study was completed in an attempt to verify these results and to determine the effects of asymmetries on the solution. The test was performed at a Rossby number of 0.625, which was chosen because it was near the delimiting line for vortex breakdown displayed in Fig. 2.1. Flows computed by previous investigators at Rossby numbers considerably below the delimiting line in Fig. 2.1 appear to become distorted and non-physical near the inflow boundary. A Reynolds number of 225 was chosen to minimize the apparent damping effects of viscosity at very low Reynolds numbers. The results of this simulation are displayed in Figs. 5.1 to 5.15 for the time level t=126.8. Unless otherwise noted, the contour plots are in the x-y plane along the centerline of the vortex. Solid contour lines denote positive values (or zero) and dashed lines denote contours with negative values. In all plots, the contour levels are evenly spaced. Plots of particle traces, vortex lines and velocity vectors are also displayed. They were obtained using PLOT3D, a three-dimensional color graphics program implemented on an Iris color graphics workstation. These plots are projections of three-dimensional vector fields onto a two-dimensional surface.

Velocity vectors, projected onto the mid plane (z=5), are displayed in Fig. 5.1. Observe that the internal structure of the breakdown region is seen to consist of a single cell, nearly symmetric about the vortex centerline. Fluid is entrained through the top half of the rear
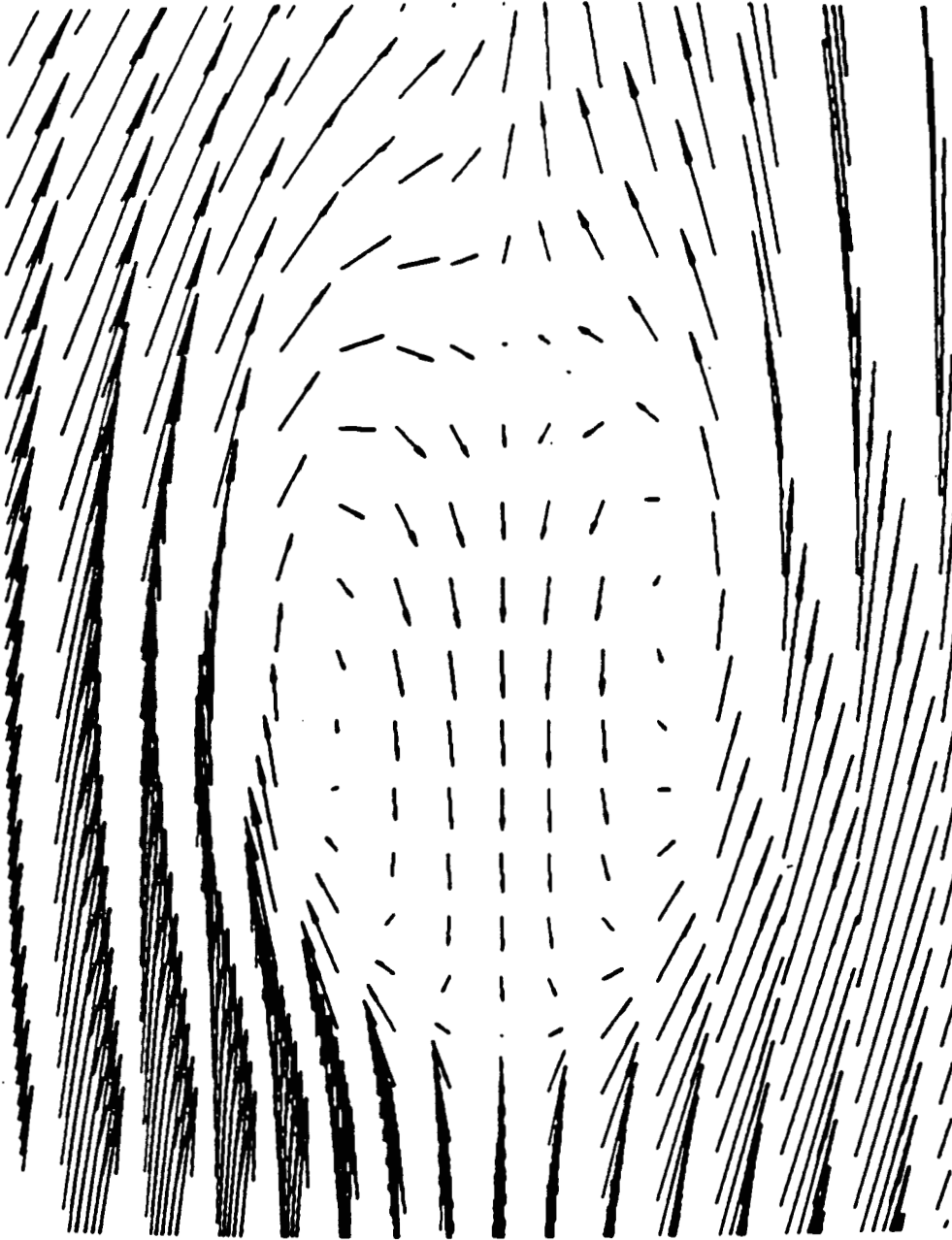
Fig. 5.1 Projected velocity vectors over the interior of the breakdown region. (x-y plane)

of the breakdown region. The fluid appears to exit the bubble from the lower half. In addition, two stagnation points along the axis can be distinguished.

Figure 5.2 represents particle traces. Nine white colored traces were started at the inflow plane. These traces were all started from a radial position within the rotational portion of the core. In addition, a trace was started within the breakdown region itself, and is represented by the red line. A third trace was started at the inflow plane but outside the core in the irrotational region of the flow. That trace is blue. Particle traces satisfy the equations $\partial \bar{x}/\partial t = \bar{u}(\bar{x}, t)$. If a particle passes through the point (x, y, z) at time $t = 0$ the solution is of the form $\bar{x} = \bar{x}(x, y, z, t)$ which traces out the pathline as t increases. The PLOT3D graphics package is limited to instantaneous particle traces, i.e., the velocity components must be time independent. Therefore, in this sense, the traces can be considered as streamlines, pathlines or streaklines because in a steady flow they all coincide. The tangents to these traces are everywhere parallel to the velocity vector.

The white traces shown in Fig. 5.2 can be seen to approach the breakdown region and diverge - never entering the cell itself. These traces also reveal that the diameter of the vortex core has increased behind the breakdown region. The red trace, released from within the bubble, is seen to spiral about within a single cell. It eventually exits the region from behind, closer to the axis radius than the white traces. The blue trace spirals around the outside of the vortex core in the irrotational region and is essentially unaffected by the breakdown.

Contours of the axial velocity are displayed in Fig. 5.3. This plot clearly reveals a breakdown region which occurs in close proximity

64

Fig. 5.2   Instantaneous streamline pattern for flow with vortex
breakdown.

to the inflow boundary. The recirculation region is bounded by the area within the innermost solid contour line (the 0.0 level contour). The breakdown bubble appears symmetric about the vortex centerline.

Figure 5.4 represents the ω_x (axial) component of vorticity. For this figure and all succeeding vorticity contour figures (including ω_y, and ω_z contours), the vorticity has been scaled by the Rossby number. For example, $\omega_x = 1.12 \ Ro(\partial w/\partial y - \partial v/\partial z)$. An interesting feature of this flow is the intensification of the axial component of vorticity occurring just aft of the breakdown region. Here, the axial vorticity has increased by approximately 25% over the maximum value at inflow. This is due to vortex stretching which results from a rapid acceleration of the axial velocity component. Within the breakdown region itself, the axial component of vorticity is small. This indicates that within the breakdown region the radial gradients of the circumferential velocities are small. Downstream of the breakdown region the contour lines become parallel, revealing a return to a quasi-cylindrical flow. In the absence of breakdown, the vorticity contour lines over the entire region would appear nearly parallel.

Contours of ω_y and ω_z vorticity are displayed in Figs. 5.5 and 5.6, respectively. The 0.0 level contours are not displayed, because outside the core of the vortex, large regions exist where the vorticity field is near zero. Therefore, plotting zero level contours results in a large number of undesirable and confusing lines in the far field. The plot represented by Fig. 5.5 is in the x-z plane since the ω_y component of vorticity in the x-y plane is nearly zero. The ω_y and ω_z components are due entirely to perturbations of the base flow since the initial (t=0) distribution possessed only an axial component of vorticity.

66
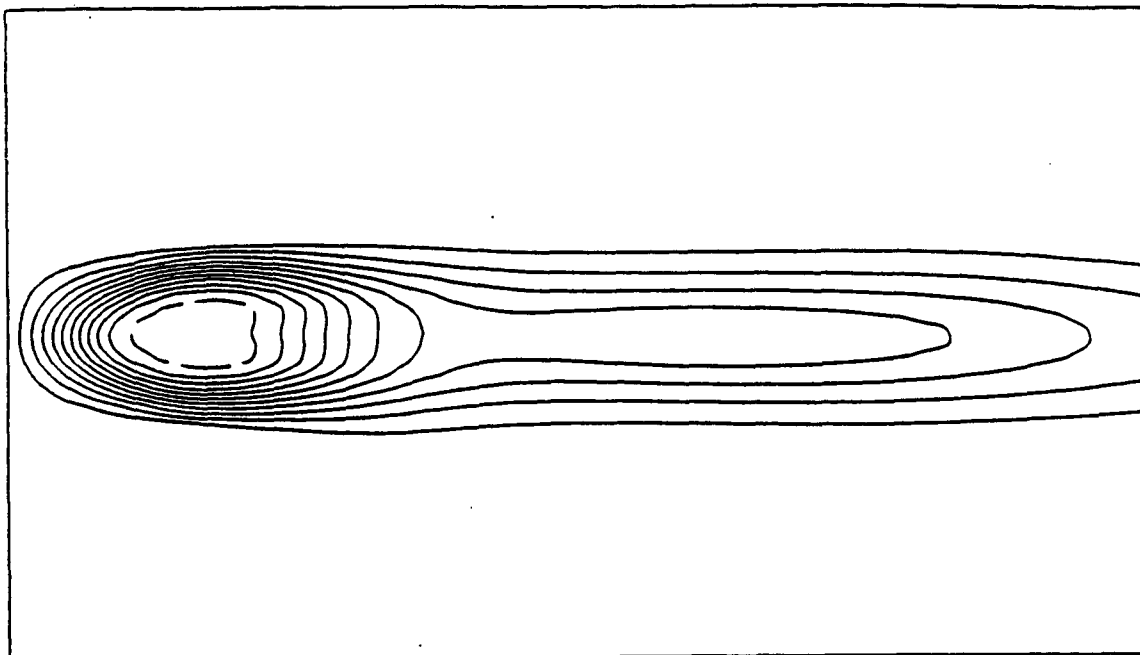
Fig. 5.3   Contours of constant axial velocity.   Contour levels range
from -0.1 (dashed) to 0.9 in intervals of 0.1.
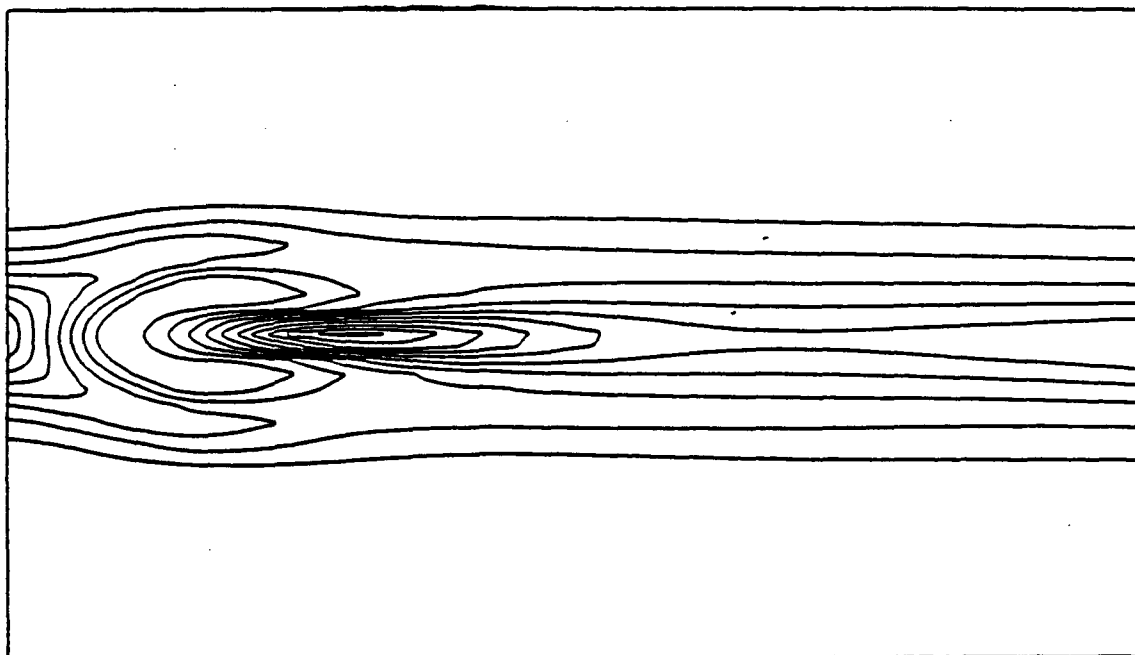
Fig. 5.4   Contours of constant axial vorticity, ω_x.   Contour levels
range from 0.25 to 2.5 in intervals of 0.25.
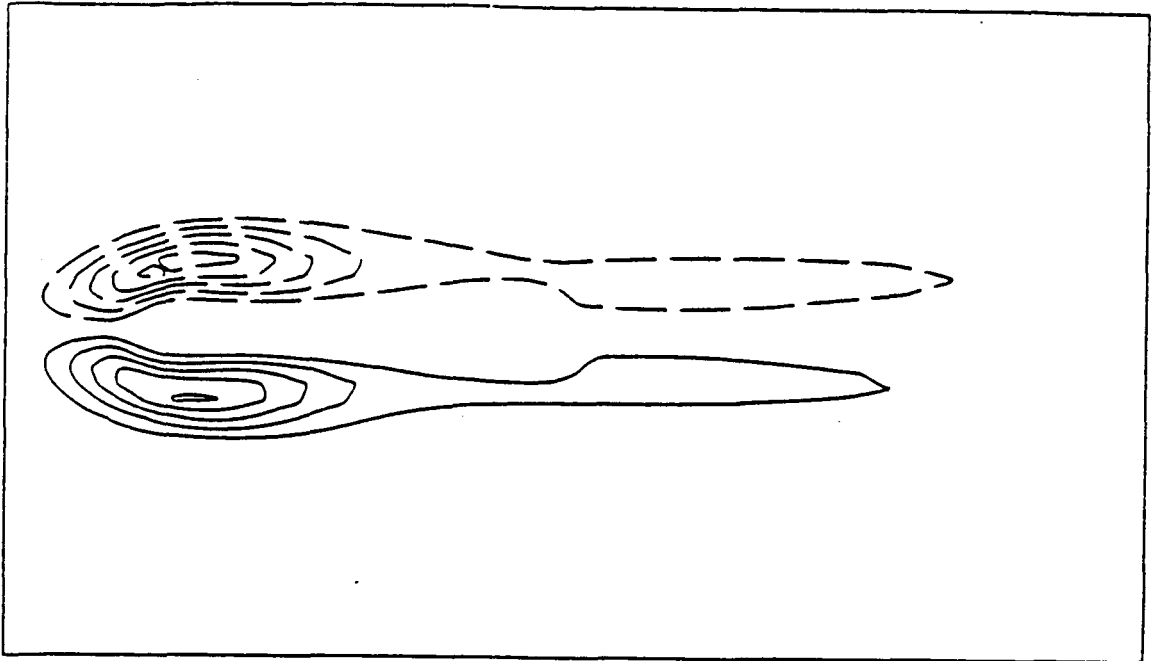
Fig. 5.5 Contours of constant ω_y vorticity. Contour levels range from -1.25 to 1.25 in intervals of 0.25.
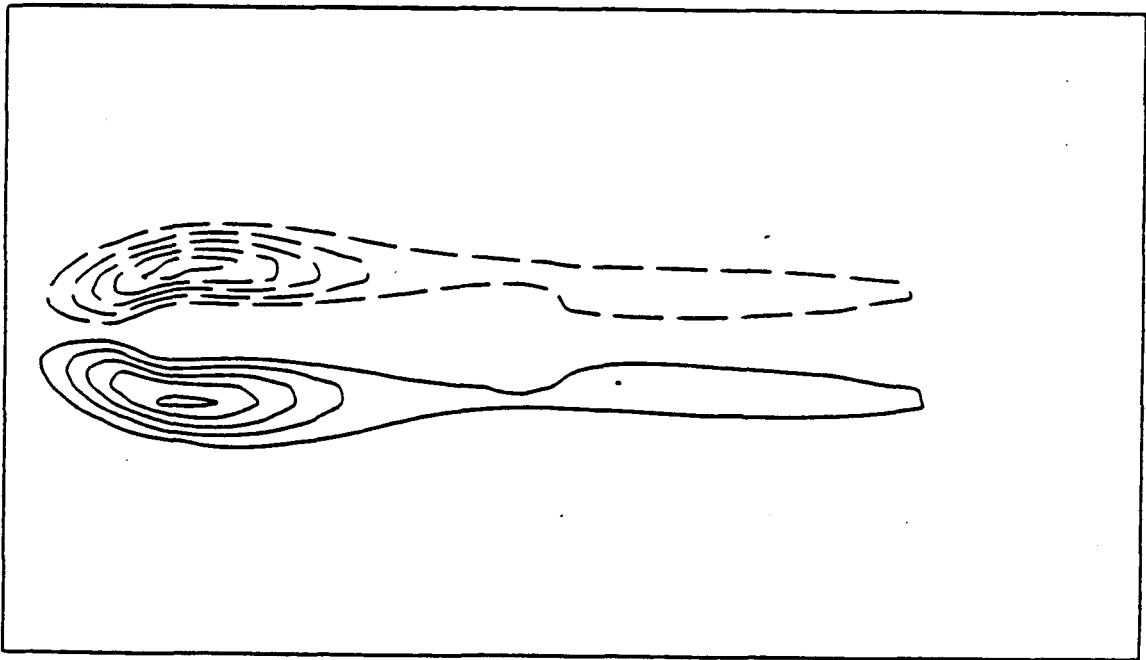
Fig. 5.6 Contours of constant ω_z vorticity. Contour levels range from -1.25 to 1.25 in intervals of 0.25.

Vortex lines are shown in Fig. 5.7. These are lines whose tangent is everywhere parallel to the vorticity vector. The lines are three-dimensional and were obtained using the Iris color graphics work-station and PLOT3D. As was the case with the particle traces, the vortex lines must be considered to be time independent. The radial locations of the lines at the inflow plane correspond to the radial locations of the white particle traces in Fig. 5.2. Note that the magnitude of the vorticity cannot be inferred from these lines. At inflow, the lines are oriented in the x direction, revealing that only the axial component of vorticity exists. Upon entering the breakdown region the lines become oriented nearly perpendicular to the vortex axis. This signifies a transfer of vorticity to the ω, and ω_z components, and is controlled by the vortex stretching and bending terms in the vorticity transport equation. Aft of the breakdown region, the vortex lines are oriented primarily in the axial direction, indicating a transfer of vorticity back to the axial component.

Figure 5.8 is a line plot of the integral $\int \frac{1}{2} \bar{\omega}^2$ dV as a function of axial location, where $\bar{\omega}^2/2$ is defined as the enstrophy. The integration was carried out over control volumes defined by $0 < y < 10$, $0 < z < 10$, Δx. The resulting numerical values were then divided by the volume over which the integration was performed. When the enstrophy is integrated over a volume of fluid it is an appropriate measure of the total amount of vorticity within the fluid [40]. The enstrophy is maximum within the breakdown region at the axial location $x \approx 3$. The enstrophy decreases and remains nearly constant downstream of the bubble.

Fig. 5.7 Vortex lines for flow with vortex breakdown.

Figure 5.9 is a line plot of the volume integral of the material derivative of enstrophy as a function of axial location. The integral is given as $\frac{d}{dt} \int \frac{1}{2} \bar{\omega}^2 dv$ which provides a measure of the rate of change of the total amount of vorticity in a specific volume of fluid, V. Here, V is enclosed by a surface B moving with the fluid. The plot displays axial variation of total enstrophy, along with the rate of change provided by stretching, viscosity and the flux of enstrophy across the boundaries of the control volume. The meaning of these terms can be explained by expanding the time rate of change of enstrophy integral in terms of volume integrals containing Eulerian derivatives. The result, derived in Appendix D, can be written as:

$$\frac{d}{dt} \int \frac{1}{2} \omega_i \omega_i dV = \int \omega_i \omega_j \frac{\partial u_i}{\partial x_j} dv - \nu \int \left(\frac{\partial \omega_i}{\partial x_j}\right)^2 dv + \frac{1}{2} \nu \int \frac{\partial(\omega_i \omega_i)}{\partial x_j} n_j dS \quad (5.1)$$

By examining the right hand side of Eq. (5.1) it can be seen that the total amount of vorticity in a material volume can change as a result of vortex stretching and viscous effects. The first term on the right, the stretching term, is positive if the fluid element is extended in the direction of the local vortex lines. The second term reveals that the effect of viscosity, neglecting diffusive transport across the boundaries, is to decrease the total enstrophy of the fluid. In general, it is possible for the entire right hand side of Eq. (5.1) to be positive, leading to an increase in the enstrophy, or total amount of vorticity, in the fluid.

The volume integrals on the right-hand side of Eq. (5.1), which are plotted in Fig. 5.9, were evaluated using trapezoidal rule integration. The integrations were performed over volumes defined by

71
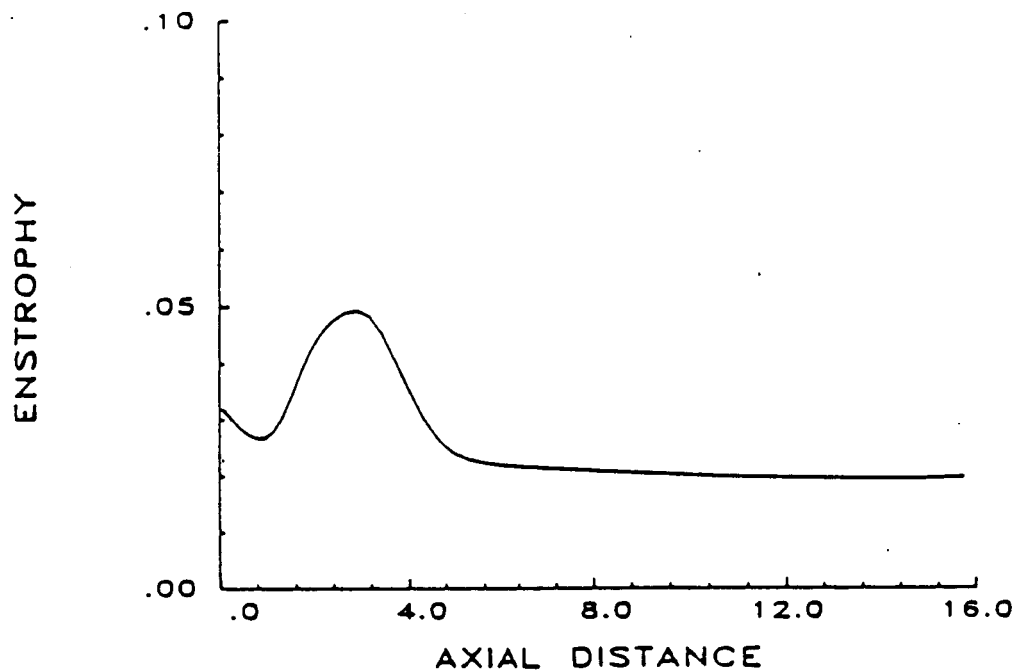
Fig. 5.8   Variation of integrated enstrophy with axial location.
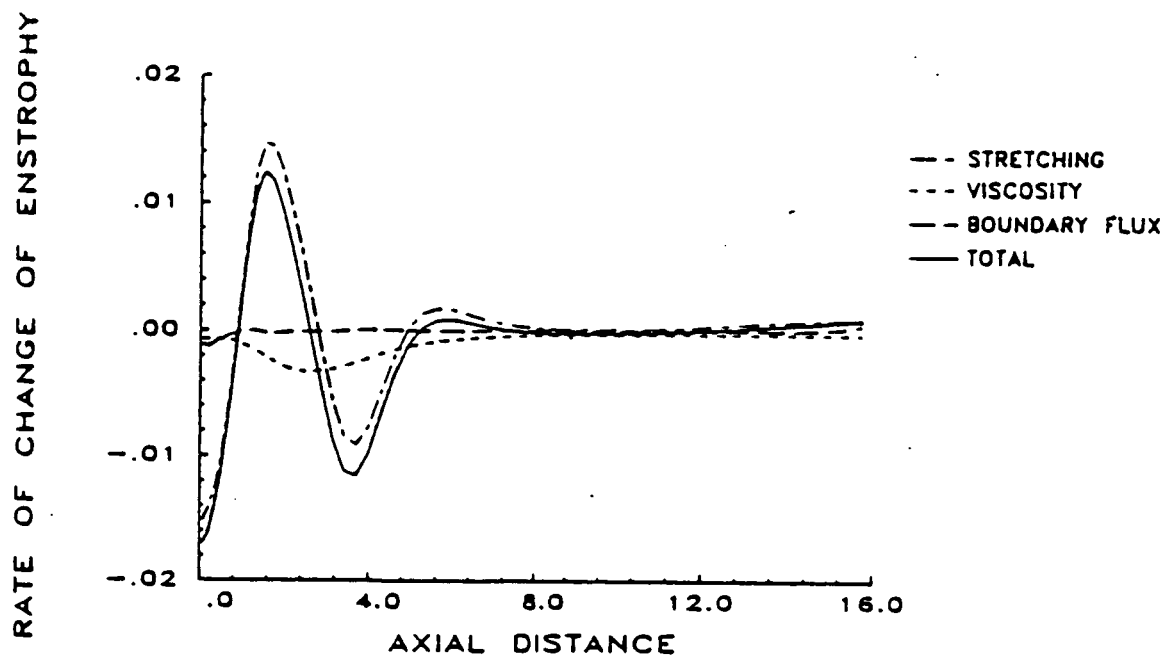
Fig. 5.9   Variation of integrated material derivative of enstrophy
with axial location.

$0 < y \leq 10$, $0 < z \leq 10$, Δx. The plotted values represent volume averages, i.e., the numerical values resulting from the trapezoidal rule integration were divided by the volume over which the integration was performed. From a Lagrangian point of view the rate of change of enstrophy of a material volume is due to both temporal changes and changes due to spatial movement of the volume. In a steady flow, the temporal changes are non-existent. Since the breakdown is an unsteady phenomena, temporal changes may be significant although it is unlikely that they are dominant. Whenever the rate of change of enstrophy is negative, the total amount of vorticity contained in a material volume passing through that location is decreasing. By examining Fig. 5.9 it is apparent that the distribution of enstrophy within the fluid is controlled, for the most part, by vortex stretching. Viscous effects appear to be important only within the breakdown region. The diffusion of enstrophy into, or out of, a material volume is negligible. The maximum and minimum values of the total rate of change of enstrophy occur at axial locations corresponding to the stagnation points. These points approximately define the front and rear of the bubble.

A contour of the pressure field, non-dimensionalized by ρU^{*^2}, is shown in Fig. 5.10. Beginning at the inflow boundary and near the centerline, the fluid encounters an adverse pressure gradient with a corresponding decrease in the axial velocity. Within the breakdown region itself, the pressure remains nearly constant. The fluid is accelerated beyond the breakdown region, and this is manifest in the form of a weak favorable pressure gradient. Downstream, the pressure contours are nearly parallel. Since the vortex was imbedded in a free

73

stream with a constant axial velocity, the pressure along the radial boundaries is nearly constant.

The relationship between the centerline axial velocity and the centerline pressure is shown in Fig. 5.11. Except for a short distance within the breakdown region, increasing axial velocities correspond to favorable pressure gradients and vice versa.

Figure 5.12 is a contour plot of the dimensionless total pressure, $q^2/2 + p$. In a steady inviscid flow, $q^2/2 + p$ remains constant along a streamline. Therefore, the above contours can be thought of as approximating streamlines. Along a streamline, wherever the dynamic pressure $(q^2/2)$ is high, the static pressure (p) is low and vice versa.

The rate of change of energy is plotted in Fig. 5.13. The rate of change of total energy is given as the sum of the rates of change of internal and kinetic energy. The rate of change of kinetic energy is given as the sum of the rates of change due to both pressure and viscous forces. For an isothermal, incompressible fluid in a Lagrangian framework, the rate of change of total energy of a specific material volume is given as:

$$\frac{d}{dt} \int (E + \frac{1}{2} \bar{u}^2) dV = -\int \frac{u_i}{\rho} \frac{\partial p}{\partial x_i} dV + \nu \int u_i \frac{\partial^2 u_i}{\partial x_j \partial x_j} dV + \partial \nu \int e_{ij} e_{ij} \, dV \quad (5.2)$$

The interpretation of the above material derivative is analagous to the interpretation given earlier for the enstrophy equation. The rate of change of internal energy is due solely to the dissipation of mechanical energy through viscous effects. Here, the shape of the fluid element is distorted. This is an irreversible loss of energy, manifested in the form of heat. This is accounted for the third term on the right hand
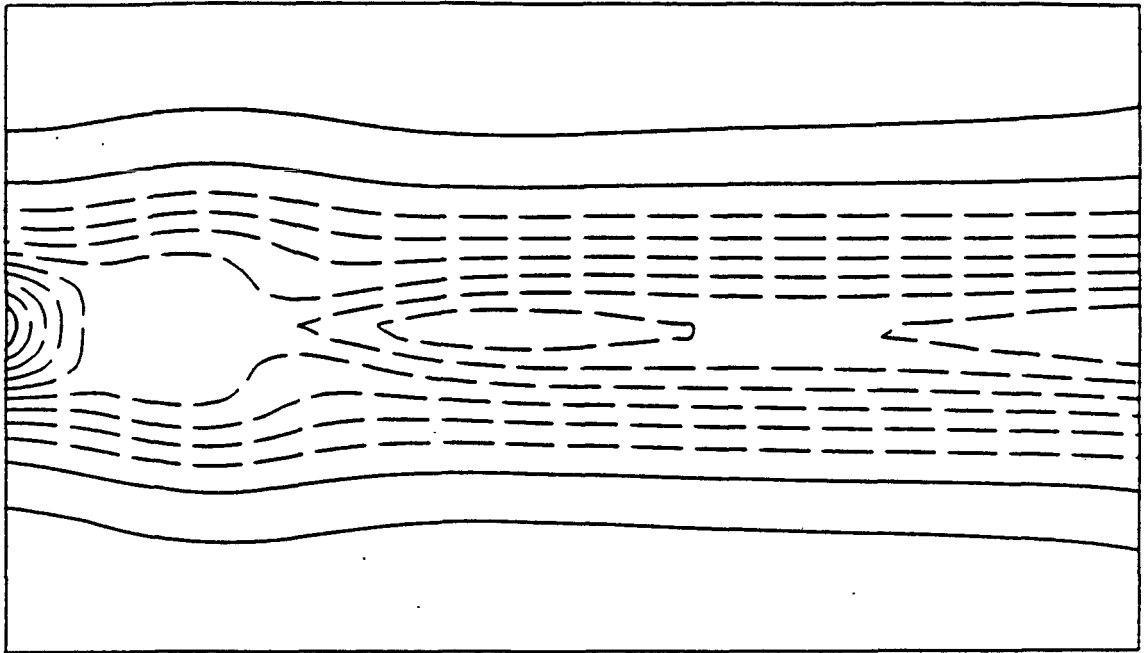
Fig. 5.10 Isobar plots: contour levels varying from -0.9 to 0.1 in intervals of 0.1.
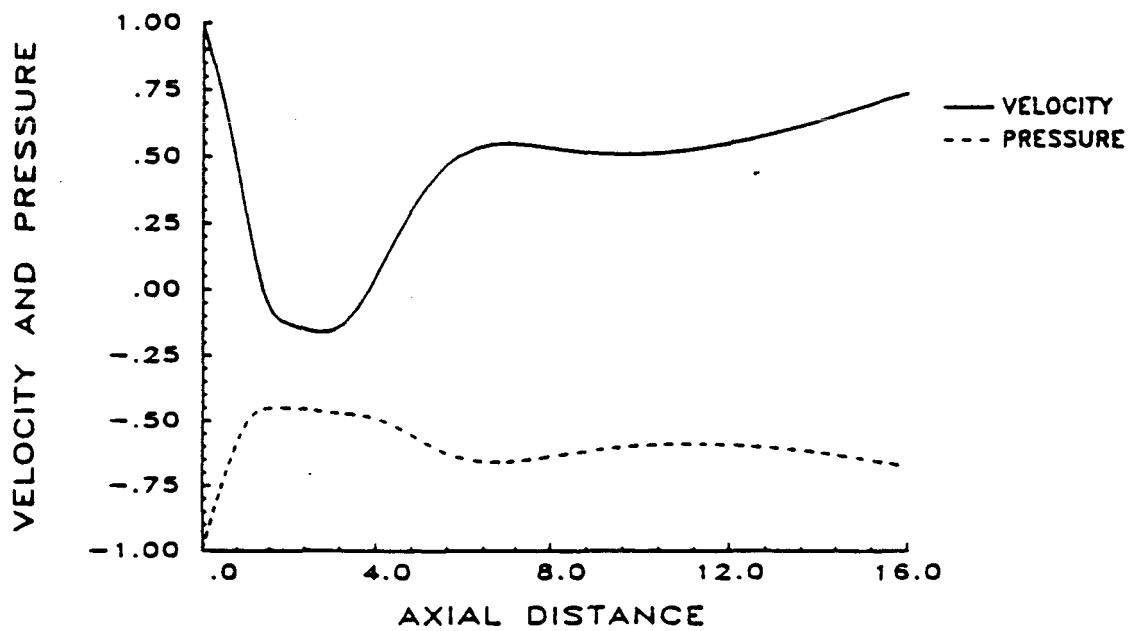
Fig. 5.11 Variation of axial velocity and pressure along the vortex centerline.
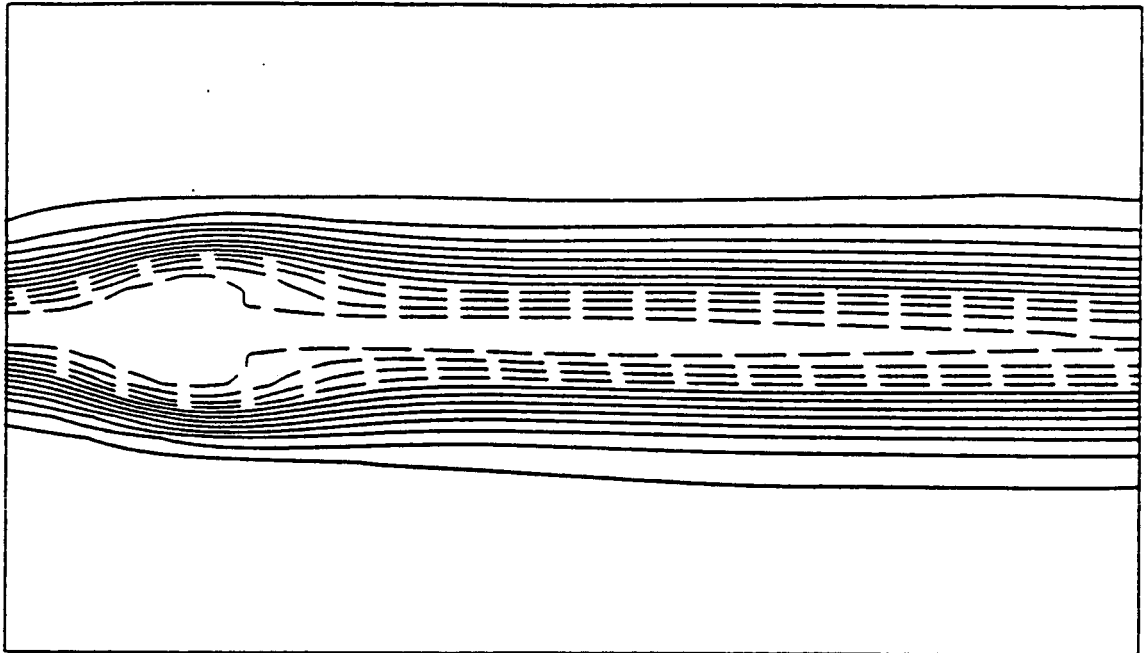
Fig. 5.12   Contours of total pressure: contour levels of -0.5 to 0.7
in intervals of 0.1.

side of Eq. (5.2). The effect of the first and second terms (pressure and viscous stresses, respectively) is to change the kinetic energy of a fluid element. The pressure forces are reversible changes in energy.

The kinetic energy per unit volume is plotted as a function of axial distance in Fig. 5.14. Following a slight decrease near inflow, kinetic energy remained constant in the axial direction.

Figures 5.15 a-d represent velocity profiles at four different axial locations. Axial (x), transverse (y) and spanwise (z) velocities are plotted as a function of the transverse coordinate (with a translation of the origin to the vortex centerline; y=5.0, z=5.0). Since the spanwise location of the data points was along the vortex centerline, the velocity components in a Cartesian system can be transformed easily to the corresponding components in a cylindrical system. The axial location of the profiles in Fig. 5.15a is slightly upstream of breakdown (x=0.27). Figure 5.15b represents profiles from within the breakdown region (x=2.52). Figure 5.15c represents profiles near the aft stagnation point (x=3.85). The profiles plotted in Fig. 5.15d are at an axial location downstream of the breakdown region (x=9.52). Upstream of breakdown, the spanwise (swirl) velocity represents the two-dimensional Burgers vortex to a good approximation. The flow is no longer quasi-cylindrical, since non-zero transverse (radial) velocities appear near the centerline. These velocities are due to the divergence of the flowfield away from the axis as the stagnation point is approached. The axial velocity shows approximately a 20% deficit near the axis. At an axial location within the breakdown region, decay of the spanwise (swirl) velocity at large radii (outside the recirculation zone) is inversely proportional to the radius. Within
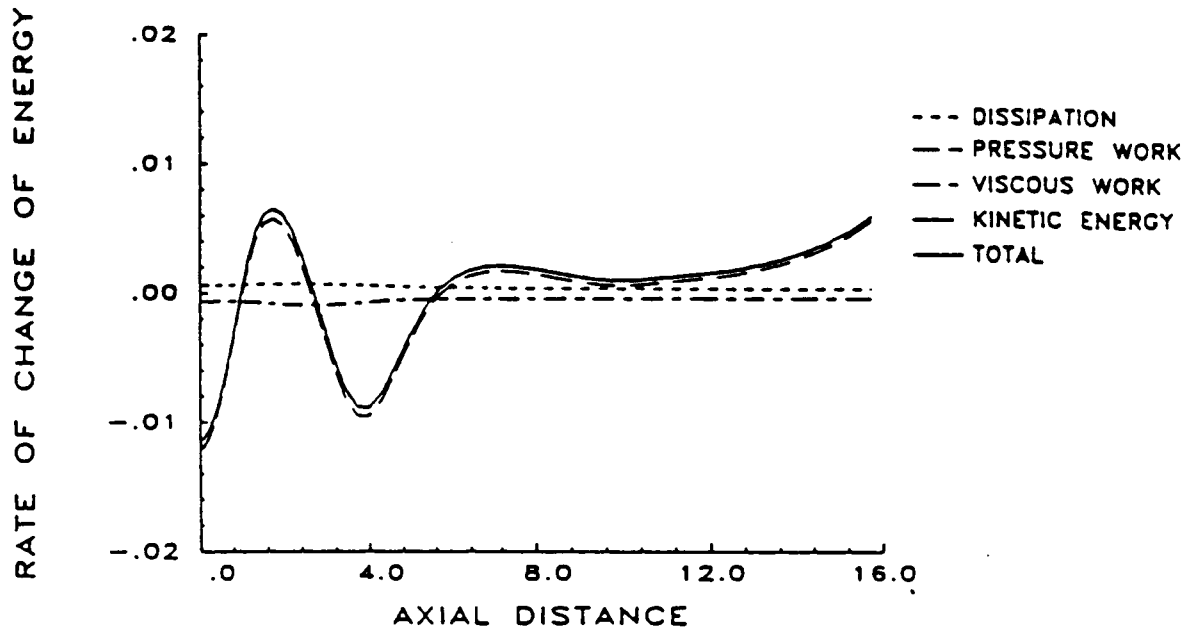
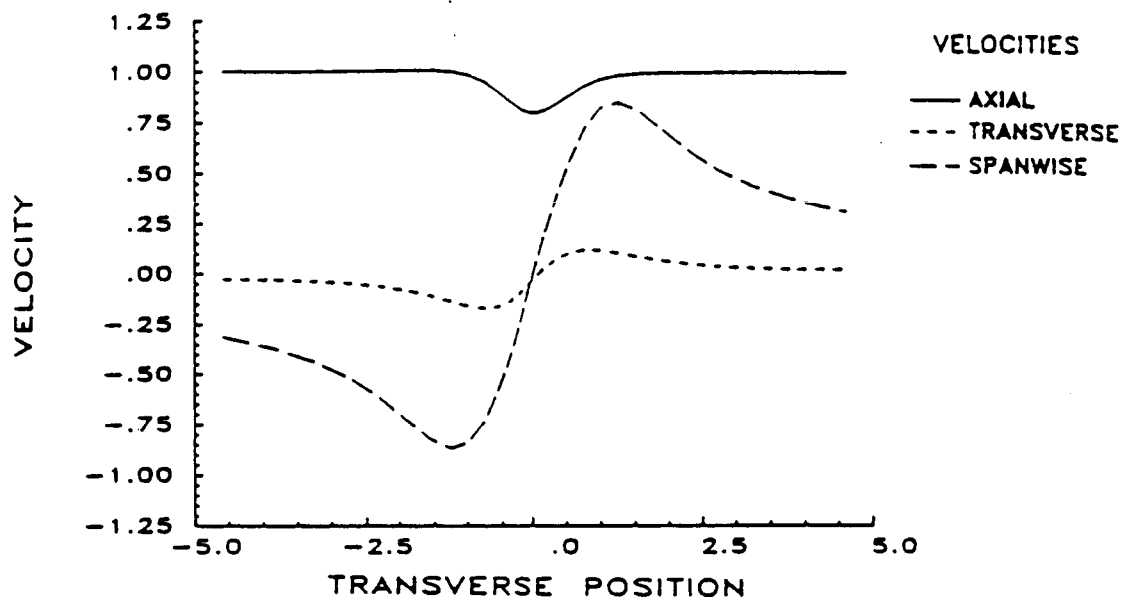Fig. 5.13 Contribution of various energy transport terms to the integrated rate of change of energy.
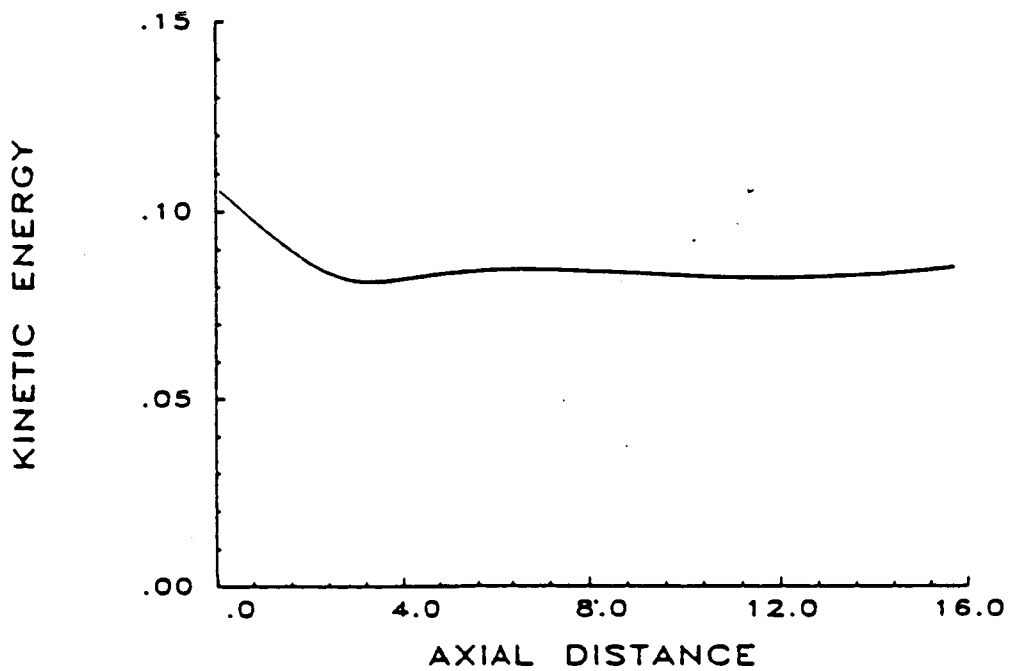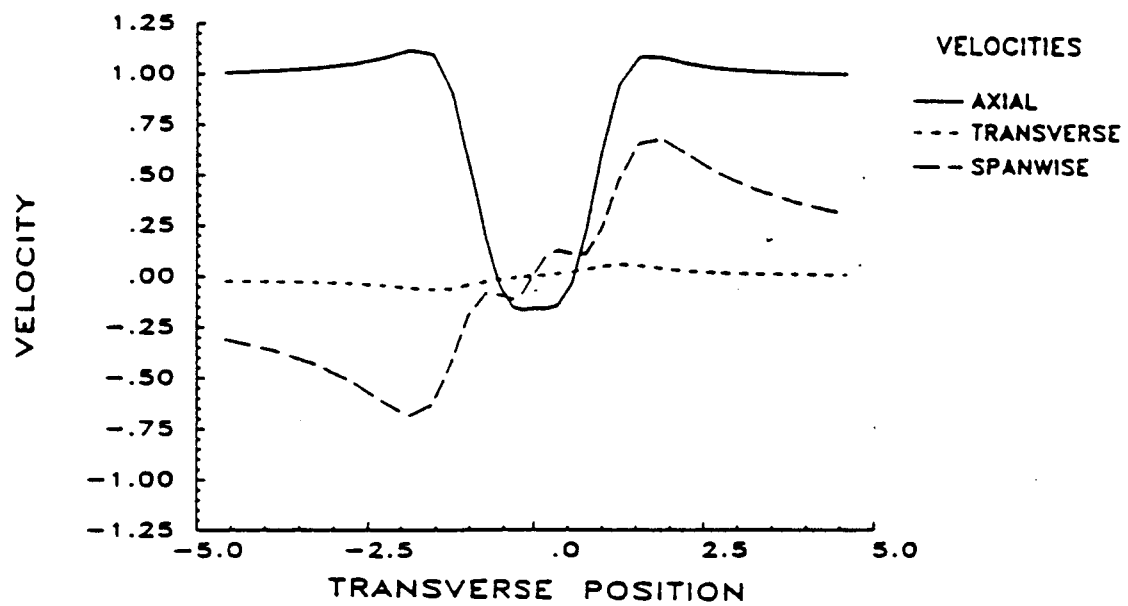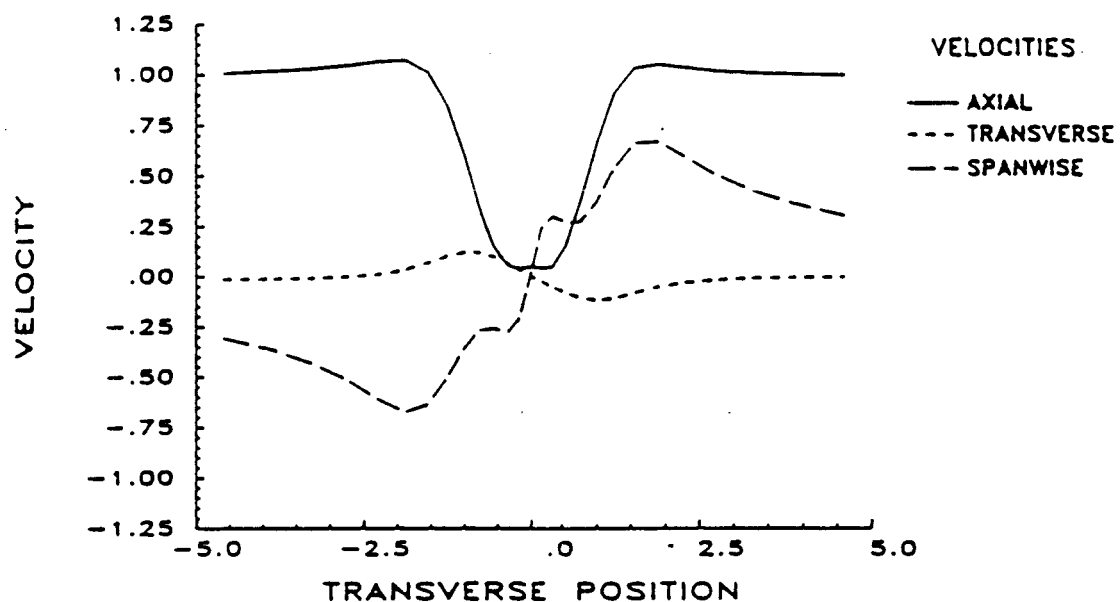

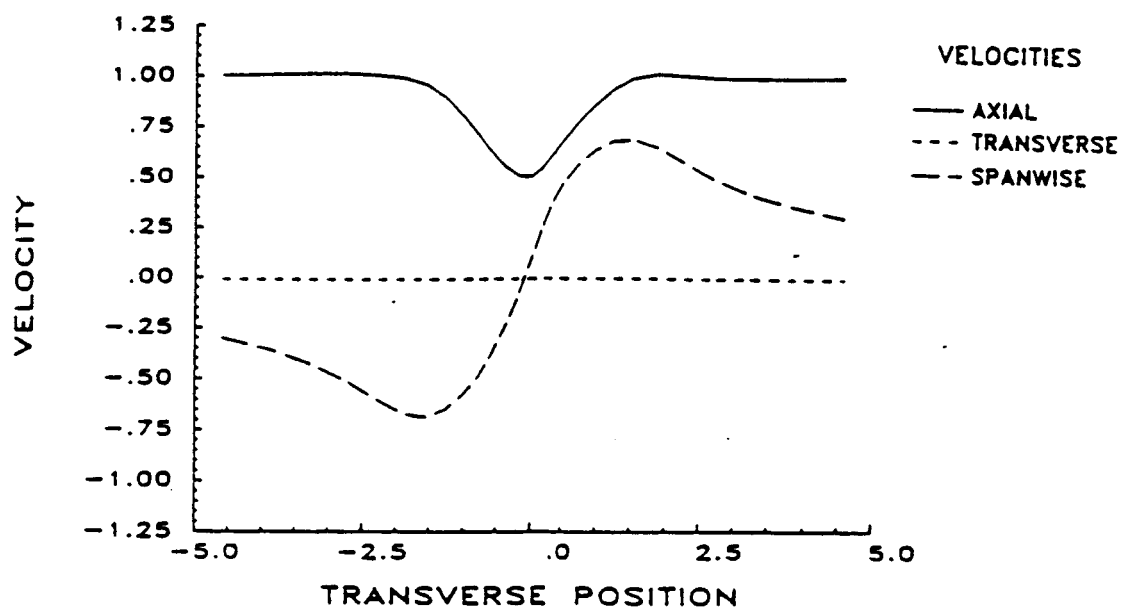Fig. 5.14 Variation of integrated kinetic energy with axial location.

(a)   x = 0.27

(b)   x = 2.52

(c) x = 3.85

(d) x = 9.52

Fig. 5.15   Radial variation of axial, swirl and radial velocity
a,b,c,d.   components at different axial locations

80

the recirculation zone, a short annular region is observed in which the spanwise (swirl) velocity is constant. The transverse (radial) velocities are near zero for all transverse (radial) locations.

In Fig. 5.15c, the transverse (radial) velocities have become significant, and are nearly the same magnitude as the transverse (radial) velocities in Fig. 5.15a, but are of opposite sign. This signifies that the axial location is near the aft portion of the bubble, since the streamlines are converging.

It is revealed in Fig. 5.15d that the flow downstream of the breakdown is quasi-cylindrical, with a small axial velocity deficit. It is apparent that the vortex core diameter, defined by the radius of maximum swirl velocity, is greater downstream of the breakdown region than upstream.

The minimum axial velocity varies with time as shown (on a semi-log plot) in Fig. 5.16. Note that the axial velocity decays exponentially to approximately 30 percent of its original magnitude (over a time period of 60 units). An exponential decay of the velocity field is indicative of a viscous time scale. By dimensional analyses, the viscous time scale for the flow is given as $t = 1.12$ Re, which for this case, equals approximately 100 time units.

Case 2 - Deceleration of the Free Stream
Axial Velocity

The breakdown just described was very similar to breakdowns computed in several previous investigations. In an attempt to alleviate the problem of the non-physical results and breakdown occurring near the inflow boundary, an additional vortex flow was computed. Here, the vortex was imbedded in a decelerating free stream. The purpose of this
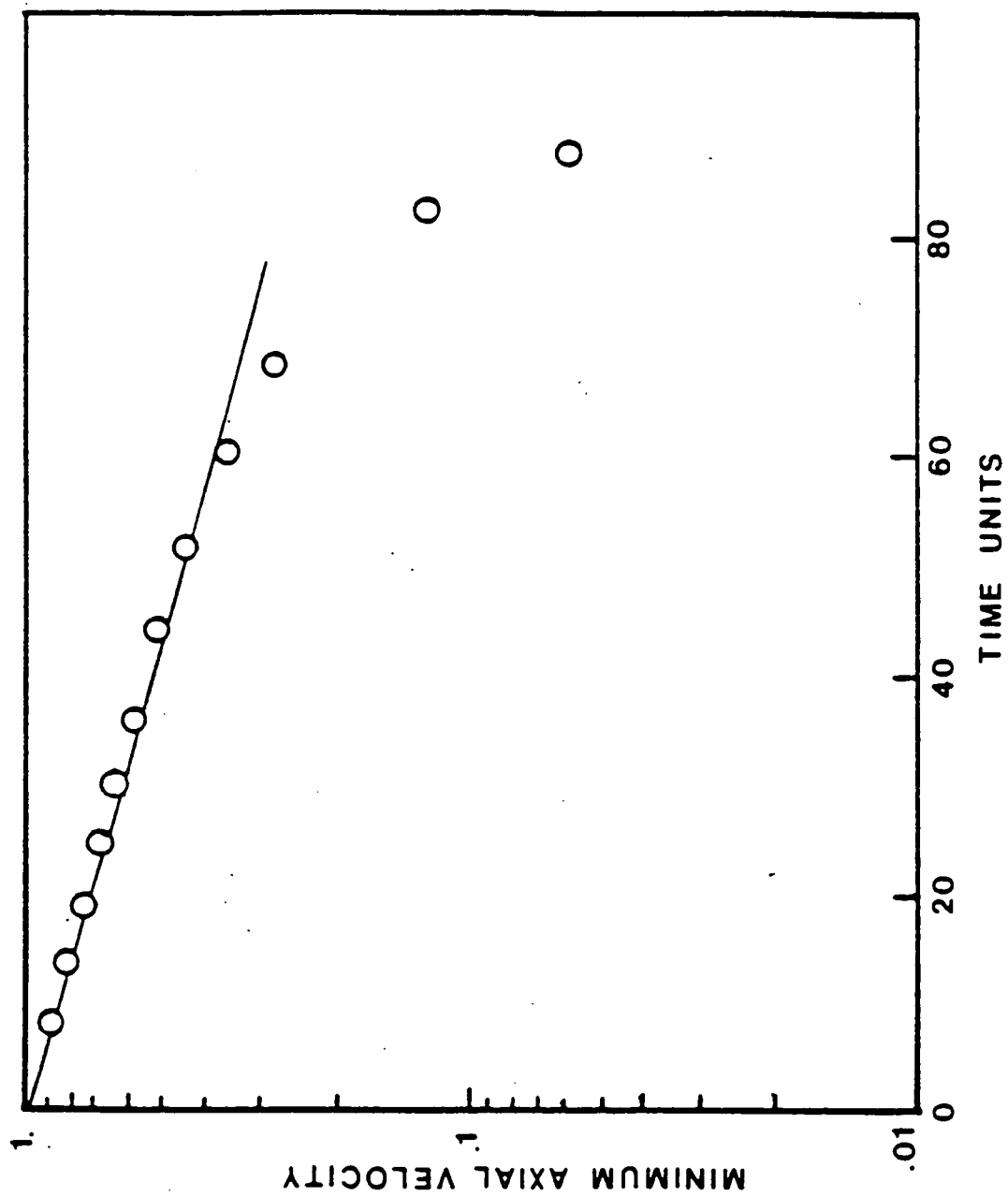
81

Fig. 5.16 Variation of the minimum centerline axial velocity with time.

82

case was to force the local Rossby number to decrease as the flow evolved in the axial direction. The Rossby number at inflow was 0.8 and the Reynolds number was 225. The free stream axial velocity was linearly decelerated from 1.0 to 0.55 over the range x=1.43 to x=16.0, thus du/dx=0.03. The results are plotted in Figs. 5.17 to 5.32. The data in Figs. 5.18 to 5.32 is at time level t=81.28. Five different time levels are represented in Fig. 5.17.

Velocity vectors, representing time levels t=81.28, 85.27, 87.45, 89.63 and 91.82 are displayed in Fig. 5.17 a-e, respectively. The general appearance of the bubble is one of asymmetry. At time t=81.28 the internal structure of the breakdown contains two major cells, or vortex rings, rotating in opposite directions about their respective axis. The aft vortex ring is inclined to the x-axis. Fluid enters the bubble from near the downstream end, through the side of the bubble, and exits the bubble at the same axial location but on the opposite side. The inclination of the aft vortex ring also appears to be related to the exchange of fluid in the bubble. The most forward section of the ring corresponds to the location of fluid influx, whereas the aft section of the ring corresponds to the location where fluid is emptied. In addition, the velocities are considerably greater in the aft portion of the bubble than in the forward portion. The length to diameter ratio of the bubble is approximately 1.75. The maximum diameter of the bubble occurs approximately 0.7L units downstream from the front stagnation point (where L is the length of the bubble).
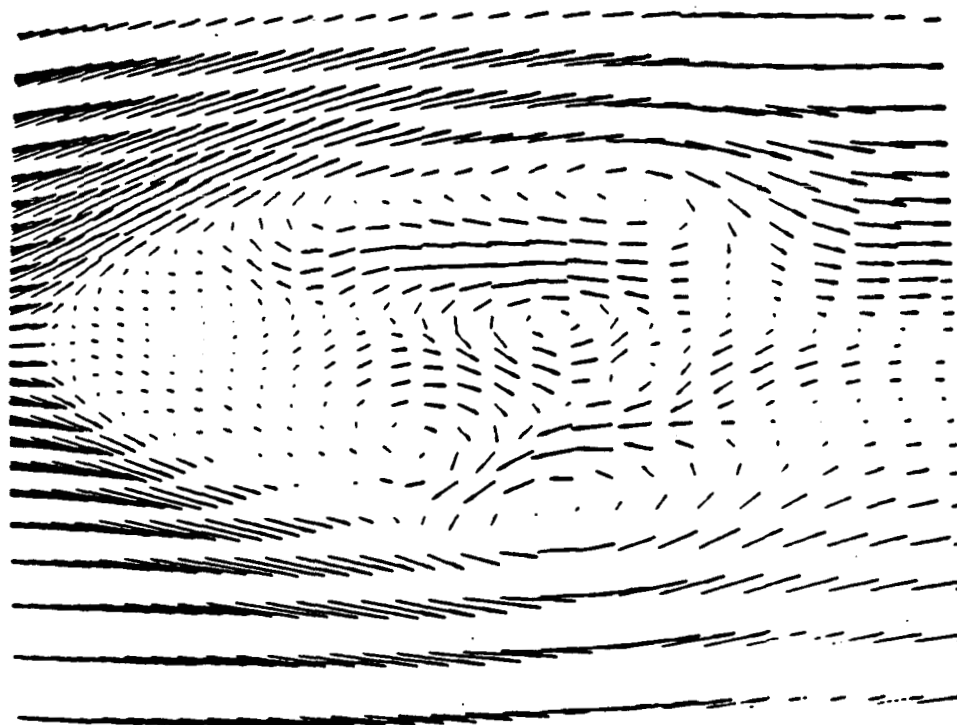
The velocity vectors for the subsequent time levels indicate that the flow within the bubble is unsteady. In addition to rotating about the x-axis, the individual cells within the bubble tend to merge and
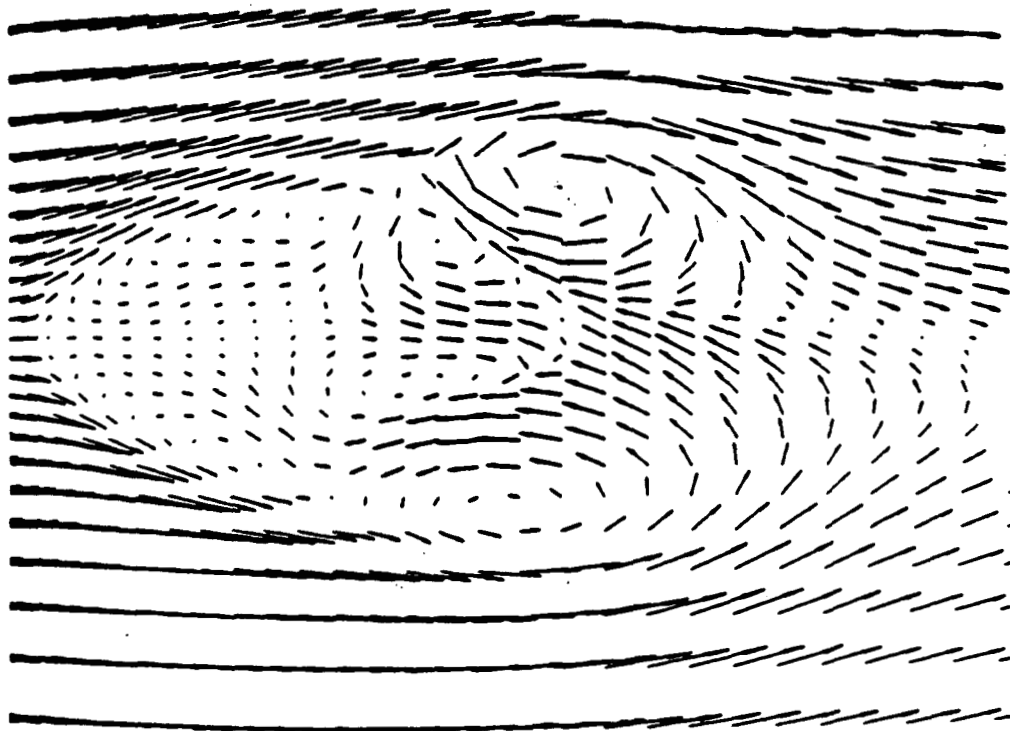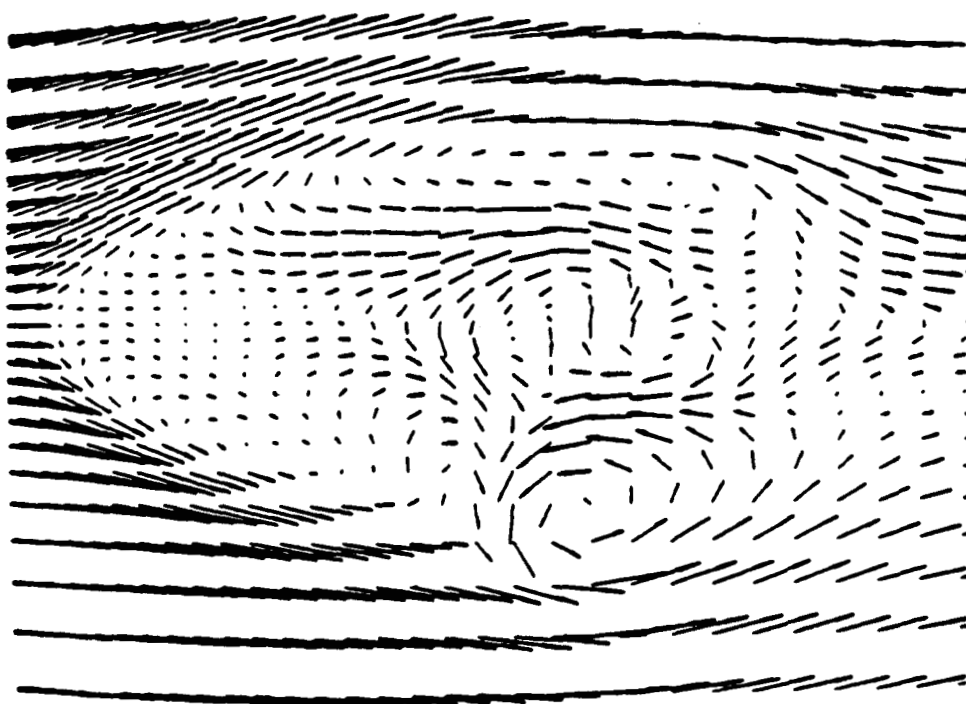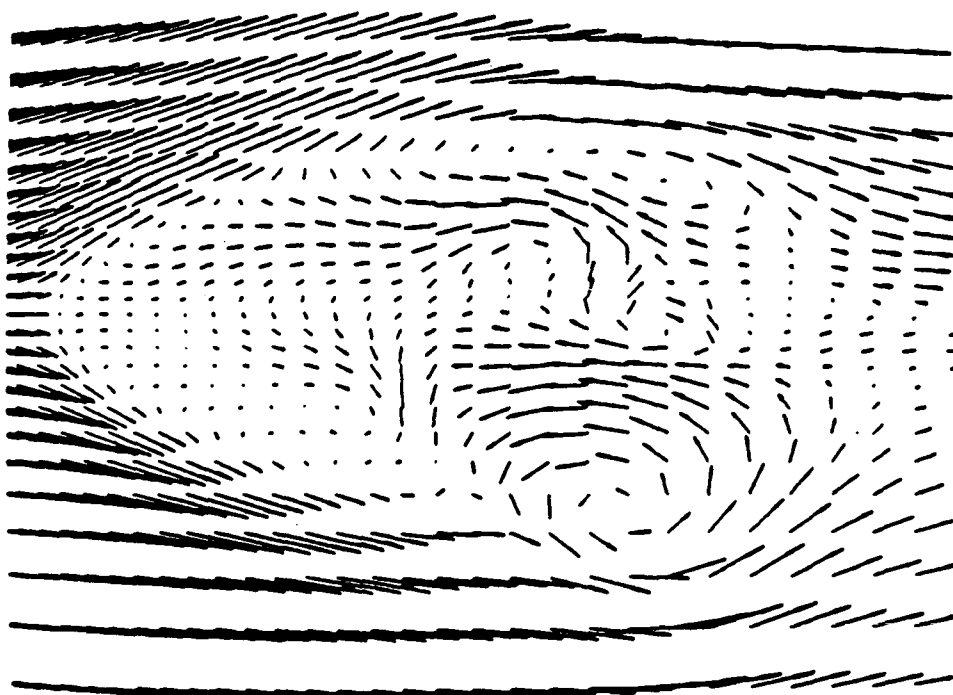
(a) t = 81.28
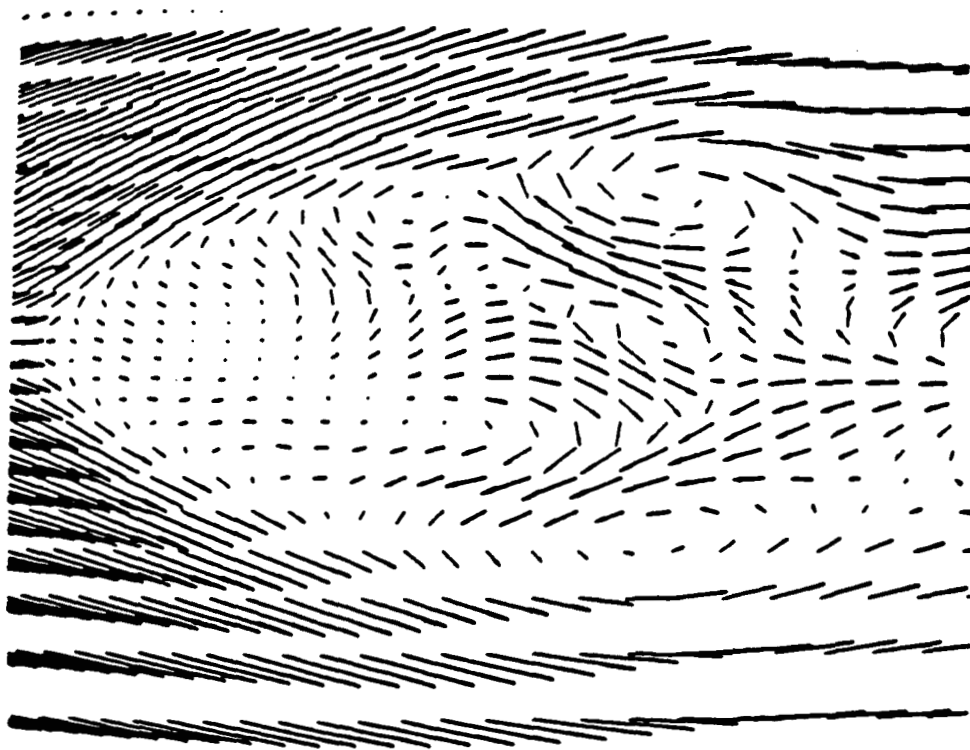
(b) t = 85.27

(c)   t = 87.45

(d)   t = 89.63

85

(e) t = 91.82

Fig. 5.17   Projected velocity vectors over the interior of the
a,b,c,d,e.   breakdown region at different time levels.

separate, and change in strength and location. The location at which fluid enters the bubble appears to have shifted towards the back for the time levels t=89.63 and t=91.82. In addition, at these time levels, the forward recirculation region has lost considerable coherence.

Particle traces are displayed in Fig. 5.18. In this figure, and for all remaining figures, the time level represented is t=81.28. An examination of the different contour plots at other time levels shows this time level to be representative of the solution. The nine white traces were started at the inflow plane from a radial position within the rotational region of the vortex. A single blue trace was started at the inflow plane, but from a radial position in the irrotational region of the flow. The red trace was started from a position within bubble in the forward cell. The yellow trace was started from within the "tail" region of the breakdown. The white traces seem to define the general shape of the bubble. One of these traces enters the forward cell, spirals about, then exits. This seems to indicate that most of the fluid approaching the bubble from the front is deflected around it. The red trace reveals that the fluid particles in the forward cell remain in the forward cell until they are forced out of the bubble. The red trace leaves the breakdown region from the side in the forward half of the bubble. The yellow trace reveals that fluid enters the breakdown region from the aft section of the bubble. The spiral traced out by this line (as it enters the bubble) is in the opposite direction to the spiral traced out by the blue line. The yellow line spirals about in the rear cell before exiting the bubble from the outer edge. Note that the red trace never enters the aft cell and the yellow trace never enters the forward cell. This indicates that the exchange of fluid between the

Fig. 5.18 Instantaneous streamline pattern for flow with vortex breakdown.

forward and aft section of the bubble is minimal. The blue trace spirals about the breakdown essentially unaffected.

Figure 5.19 is a contour plot of the axial component of velocity. The breakdown region is located near the center of the computational domain. The recirculation region ·is defined by the outer 0.0 level contour line. Immediately within this region are negative valued contour lines. Interior to these negative valued contour lines are additional positive valued contour lines. Thus, along the centerline of the bubble there exists a region in which no flow reversal occurs. The contour lines intersecting the top and bottom of the domain indicate a decelerating external flow (which was imposed by the boundary conditions).

A contour plot of the axial component of vorticity (scaled by the Rossby number) is shown in Fig. 5.20. The vorticity decreases continuously as the stagnation point is approached. In the forward portion of the breakdown region, the axial component of vorticity is nearly zero. This indicates that the radial gradients of the swirl velocity are small. In contrast, the aft section of the breakdown region is characterized by high levels of ω_x vorticity along the axis. Furthermore, the radial gradients of ω_x vorticity in this region are high. Note that the vorticity is negative in the region of the bubble corresponding to the approximate location of the aft vortex ring.

Figures 5.21 and 5.22 are contour plots of the ω_y and ω_z components vorticity respectively. The 0.0 level contours are not displayed, as was the case in Figs. 5.5 and 5.6. These components are due entirely to perturbations of the base flow since at time t=0.0 the only non-zero vorticity component was ω_x. The asymmetric, two celled structure of the
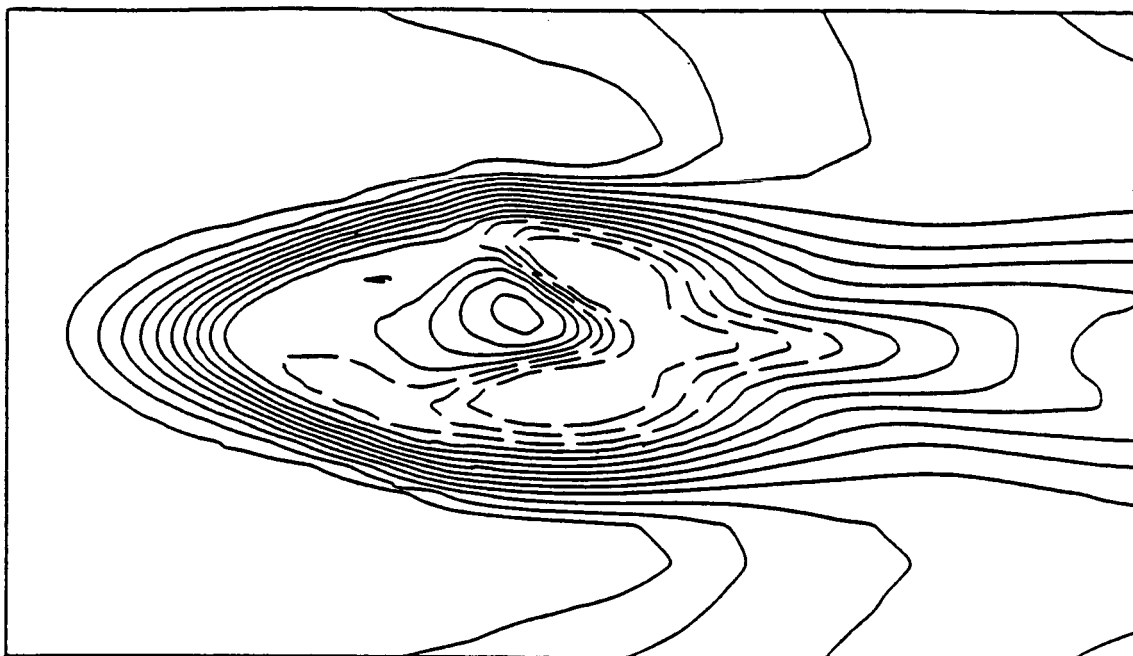
Fig. 5.19   Contours of constant axial velocity.   Contour levels range
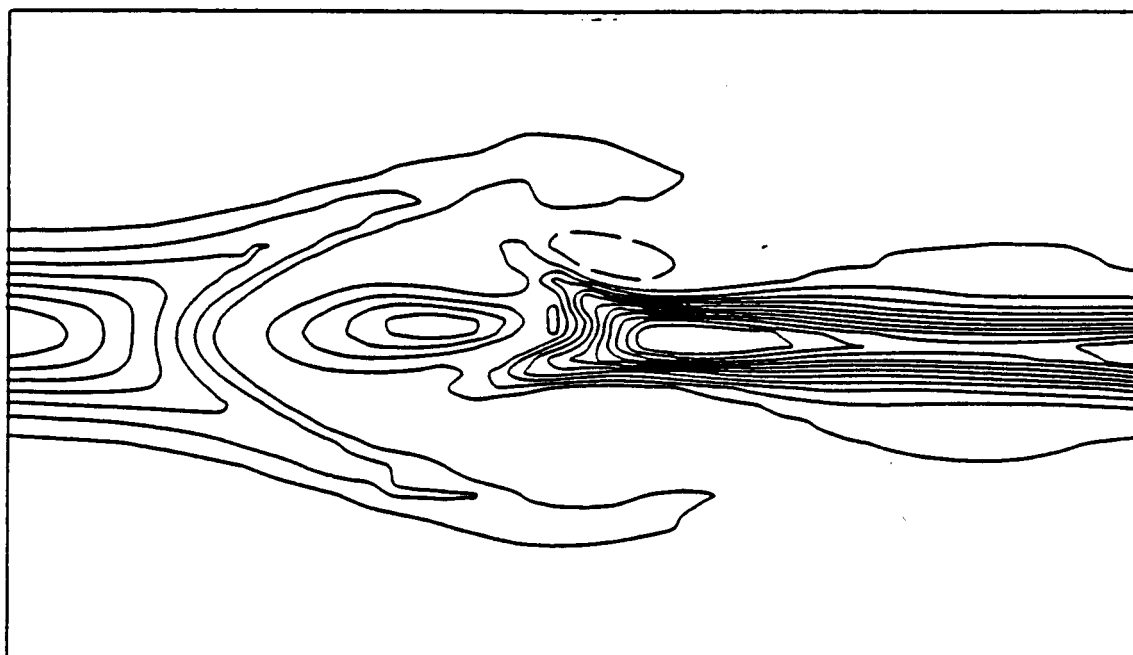   from -0.3 to 0.9 in intervals of 0.1.

Fig. 5.20   Contours of constant axial vorticity, ω_x.   Contour levels
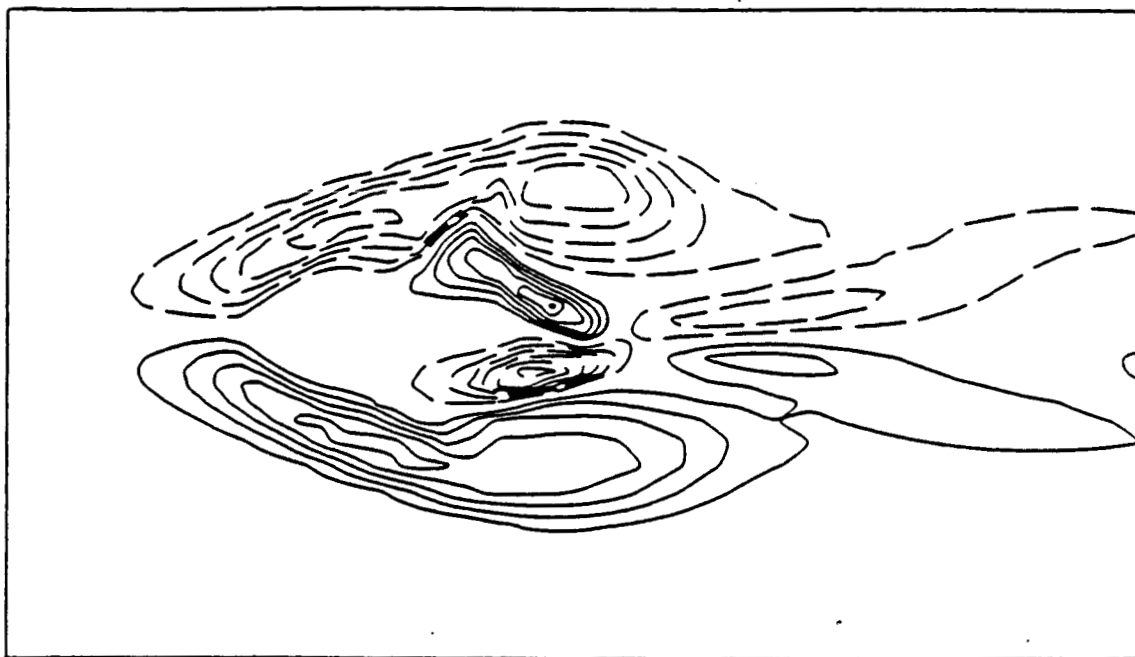   range from -.0.25 to 2.5 in intervals of 0.25.

Fig. 5.21 Contours of constant ω_y vorticity. Contour levels range
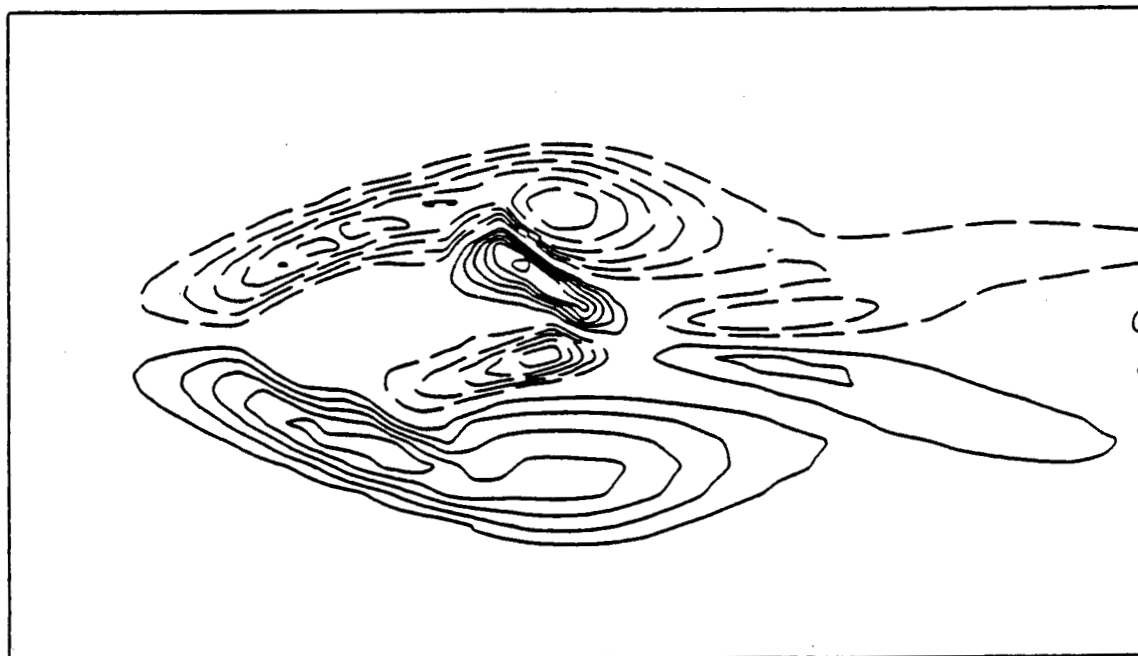from -1.50 to 1.50 in intervals of 0.25.

Fig. 5.22 Contours of constant ω_z vorticity. Contour levels range
from -1.50 to 1.50 in intervals of 0.25.

bubble is revealed in these contours. In addition, points on the axes of the two vortex rings can be identified. Since the vorticity of the two rings is of opposite sign, they rotate in opposite directions about their respective axes. The maximum vorticity levels in these two rings is approximately equal. A possible third vortex ring can be seen in the outer region of the forward portion of the bubble. This ring rotates in the same direction as the aft most vortex ring.

Vortex lines are shown in Fig. 5.23. The radial locations of these lines at the inflow plane correspond to the locations of the white particle traces at inflow. In the approach flow the vortex lines are oriented in the x-direction. The transfer of vorticity from the x to the y and z components takes place as the first stagnation point is approached. Different orientations of the vorticity vector are observable within the bubble. Near the centerline of the bubble, the vorticity vector is oriented primarily in the axial direction. Near the outer regions, the orientation is mostly in the circumferential direction. Downstream of the breakdown, the vorticity vector is oriented in the axial direction, but with a superimposed small undulation.

A line plot of the integral of $\frac{1}{2} \bar{\omega}^2$ as a function of axial location appears in Fig. 5.24. This figure shows that the enstrophy per unit volume of fluid remains nearly constant in the streamwise direction until the breakdown region is encountered. Here, large gains in enstrophy are realized. Downstream of the breakdown region, the enstrophy level returns to the levels present upstream of breakdown.

The volume integral of the material derivative of enstrophy is plotted in Fig. 5.25. The distribution of enstrophy within the
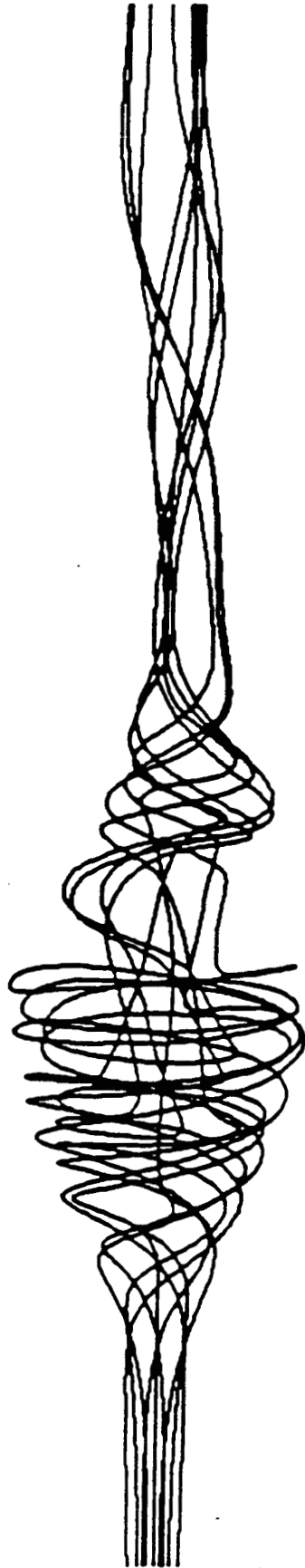
92

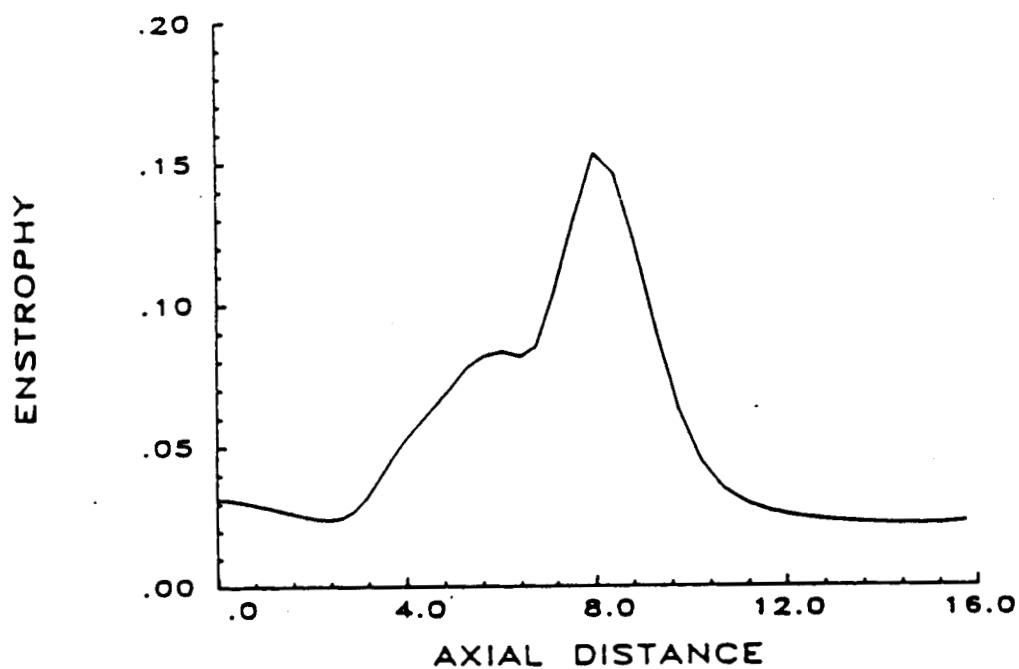Fig. 5.23 Vortex lines for flow with vortex breakdown.

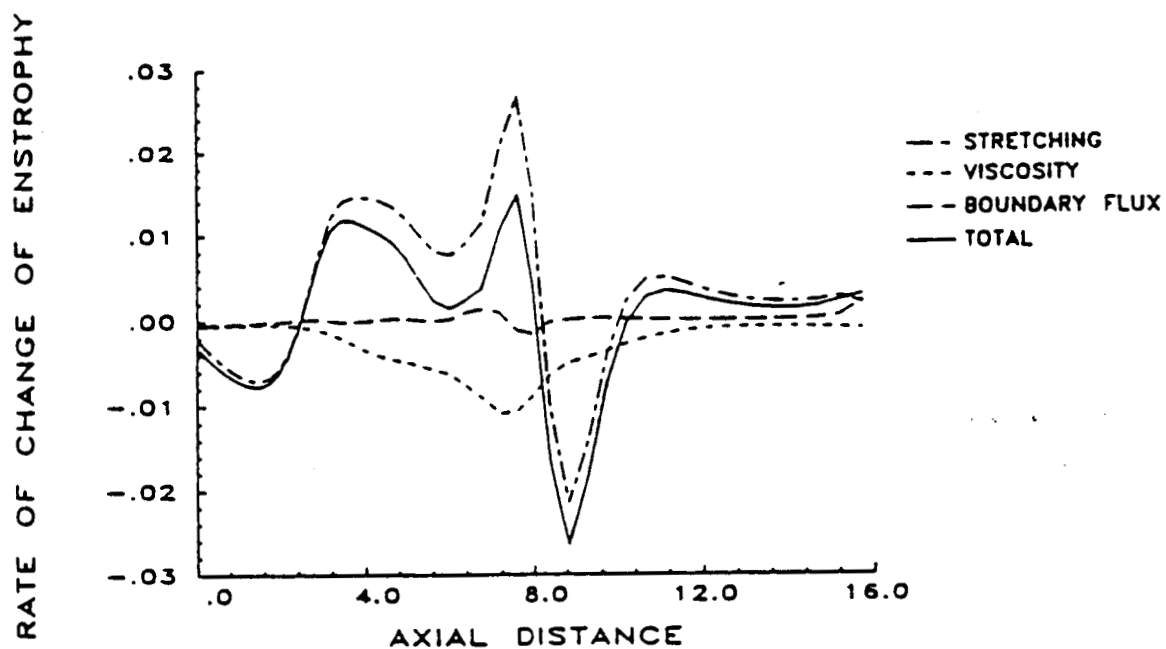Fig. 5.24 Variation of integrated enstrophy with axial location.

Fig. 5.25 Variation of integrated material derivative of enstrophy with axial location.

94

breakdown region is affected significantly by both vortex stretching and viscous action. The effect of viscosity is to offset the gains in enstrophy due to stretching. The enstrophy changes due to diffusion across the boundaries of a specific material volume are insignificant. The axial location at which the enstrophy is a maximum agrees with the location in where the rate of change of enstrophy is zero.

Contour lines of pressure are shown in Fig. 5.26. The minimum pressure at any axial location occurs along the centerline of the vortex, with the absolute minimum occurring at inflow. A strong adverse gradient is encountered by the fluid as it approaches the breakdown region. Within the forward part of the breakdown region, the pressure is nearly constant. A local minimum occurs in the aft portion of the bubble. This point corresponds to the location of minimum axial velocity. The pressure distribution is asymmetric. This may correspond to the orientation of the aft vortex ring.

The pressure and axial velocity along the vortex centerline are plotted in Fig. 5.27. A strong adverse pressure gradient extends from the inflow boundary to the axial location x=3.2, corresponding to the first stagnation point. From x=3.2 to x=7.2 a decrease in pressure is accompanied by an increase in the axial velocity. The axial velocity then decelerates rapidly even though the pressure continues to decrease. Downstream of the breakdown region, the centerline axial velocity is accelerated toward its free stream value. Stagnation points are observed at axial locations x=3.0, 5.5, 8.3. and 12.3.

Since the external flow was decelerated in the axial direction, it was expected that a corresponding adverse pressure gradient would exist. For clarity, the pressure variation along the top computational
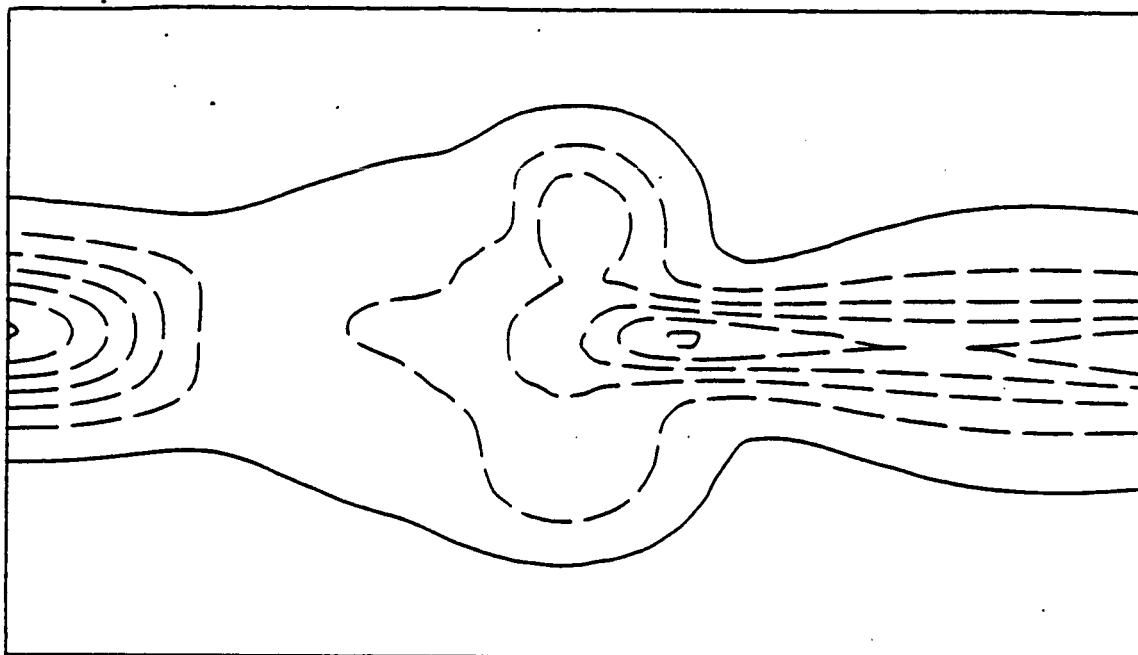
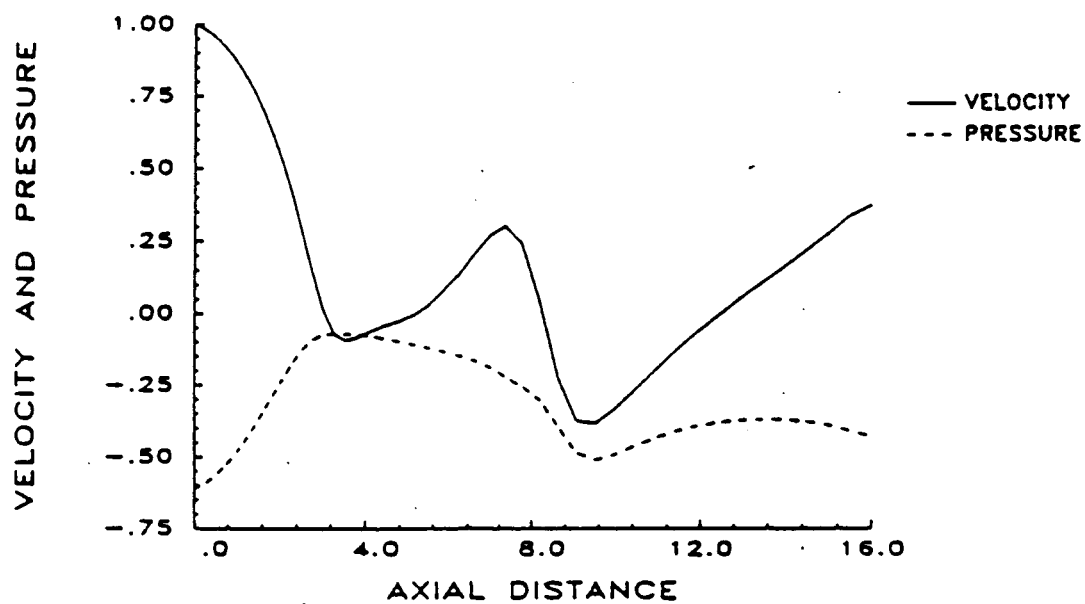Fig. 5.26 Isobar contours: contour levels of -0.6 to 0.0 in intervals of 0.1.

Fig. 5.27 Variation of axial velocity and pressure along vortex centerline.

boundary (y=10.0, z=5.0) is plotted as a function of axial location in Fig. 5.28 using a magnified scale. A rapid change in the slope is apparent at x=1.5. This corresponds to the approximate axial location in which the imposed deceleration of the free stream axial velocity begins. The pressure then increases linearly until the axial location corresponding to the onset of breakdown is reached. Downstream from this location the pressure decreases and then increases. This is due to the curvature of the streamlines (displayed in Fig. 5.29). Experimental wall pressure distributions measured by Sarpkaya [25] in a tube and vane apparatus behaved in a similar manner. Note that the maximum values of dp/dx along the computational boundary are much smaller in magnitude than the values of dp/dx occurring within the vortex core.

Figure 5.29 is a contour plot of the total pressure, $q^2/2 + p$. As previously mentioned, where viscous forces are insignificant and the flow is steady, these lines can be considered as streamlines. In this sense, the aft recirculation cell is clearly visible.

The volume integral of the material derivative of energy is plotted in Fig. 5.30. The interpretation of the various lines follows from the description of 5.13. Note that the rate of change of energy due to pressure work follows the total rate of change of energy almost exactly. These lines appear on top of one another in Fig. 5.30. As is required, the rate of change of internal energy is positive throughout the flow. The magnitude of this change is small when compared to the rate of change of kinetic energy throughout most of the region. The plot shows that the rate of change of kinetic energy is due primarily to differential pressure forces acting on a material volume. The viscous forces responsible for changing the kinetic energy are small.
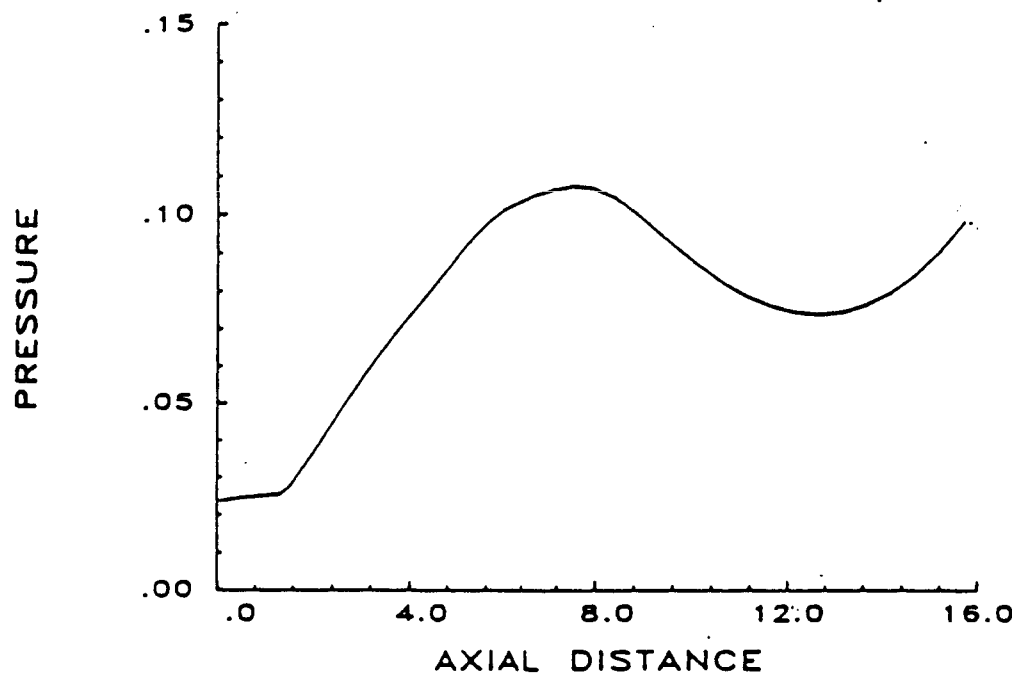
Fig. 5.28   Computed pressure distribution along the top computational
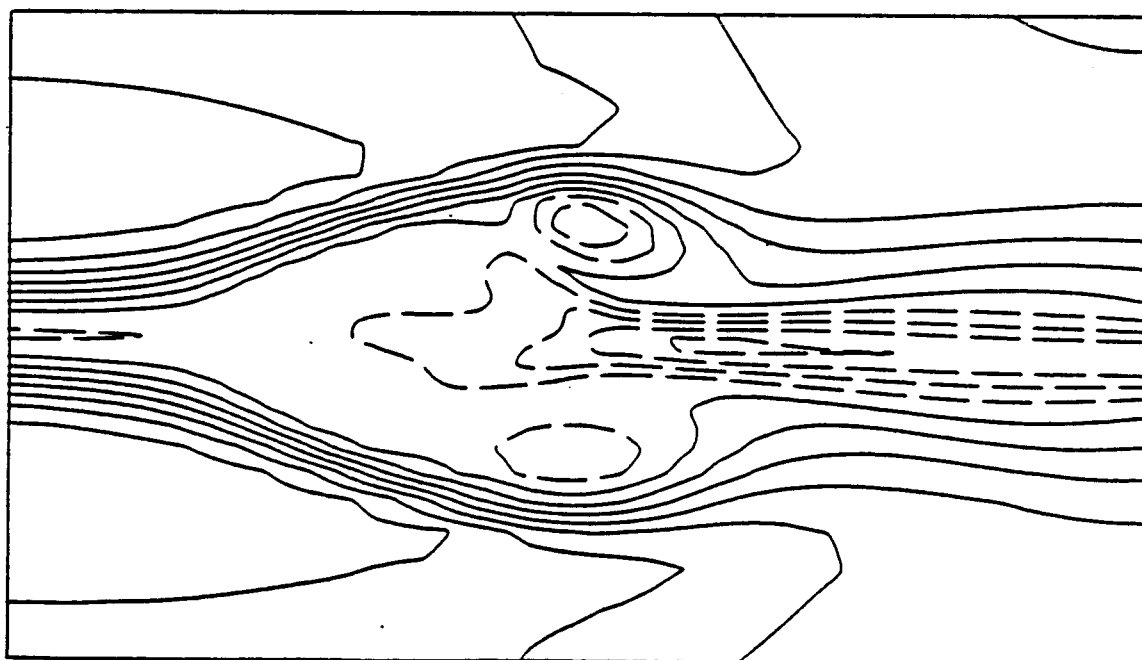boundary.

Fig. 5.29   Contours of total pressure: contour levels of -0.4 to 0.6 in
intervals of 0.1.

The integral of the volume averaged kinetic energy has been computed and plotted as a function of axial location in Fig. 5.31. The kinetic energy is observed to decrease by approximately 50% between the inflow plane and the axial location, x=8.0. Downstream of this point, the kinetic energy increases slightly and then remains constant.

Axial, transverse (radial), and spanwise (swirl) velocity profiles at four different axial locations are plotted in Fig. 5.32 a-d for time level t=81.28. The axial location of the profiles in Fig. 5.32a is upstream of breakdown (x=0.41). The profiles in Figs. 5.32b and 5.32c represent axial locations within the breakdown region (x=5.46 and x=7.36, respectively). Profiles from downstream of the breakdown region are plotted in Fig. 5.32d (x=13.92). For reference purposes, the first stagnation point is located at x=3.0. Upstream of breakdown, the spanwise (swirl) velocity profile approximates the two-dimensional Burgers vortex. The radial velocity is small and the axial velocity profile nearly uniform. Within the breakdown region, as revealed in Figs. 5.32b and 5.32c, the flow is no longer symmetric. Transverse (radial) velocities are significant and the spanwise (swirl) velocity profiles no longer approximate Burgers vortex. At both axial locations within the breakdown, the axial velocity profiles have a local maximum and two local minima. The profiles in Fig. 5.32d, downstream of the breakdown region, reveal a large axial velocity deficit near the vortex centerline. The spanwise (swirl) velocity profiles reveal a solid body-like rotation near the centerline. At the edge of the core, the maximum spanwise (swirl) velocities are considerably less than values occurring upstream of the breakdown region.
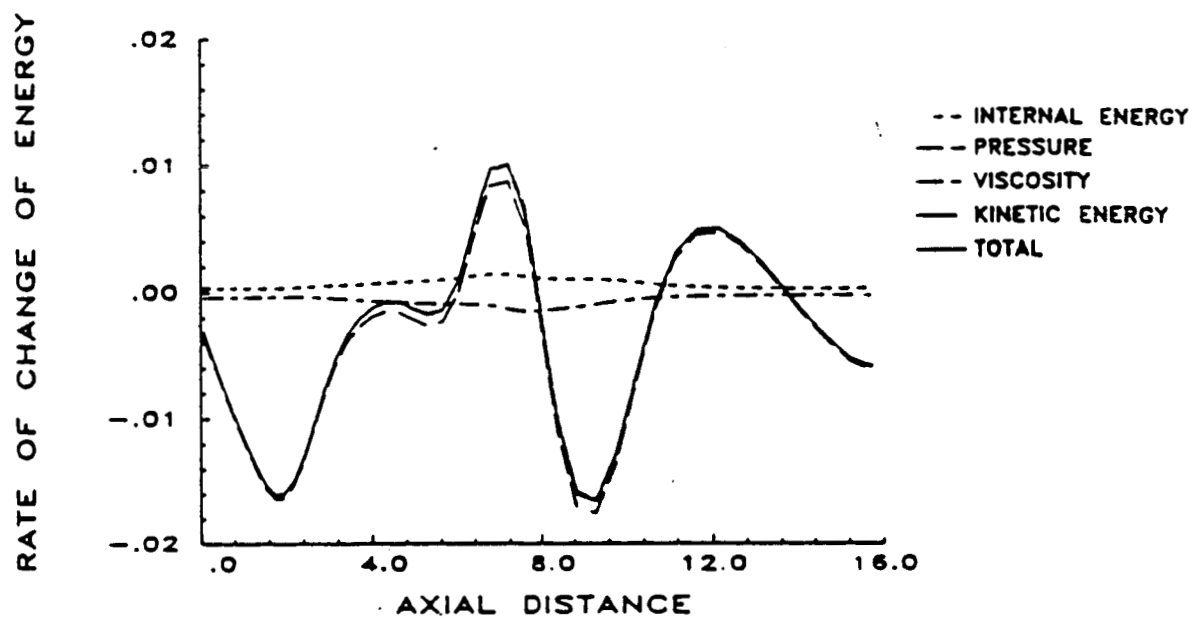
Fig. 5.30 Contribution of various energy transport terms to the integrated rate of change of energy.
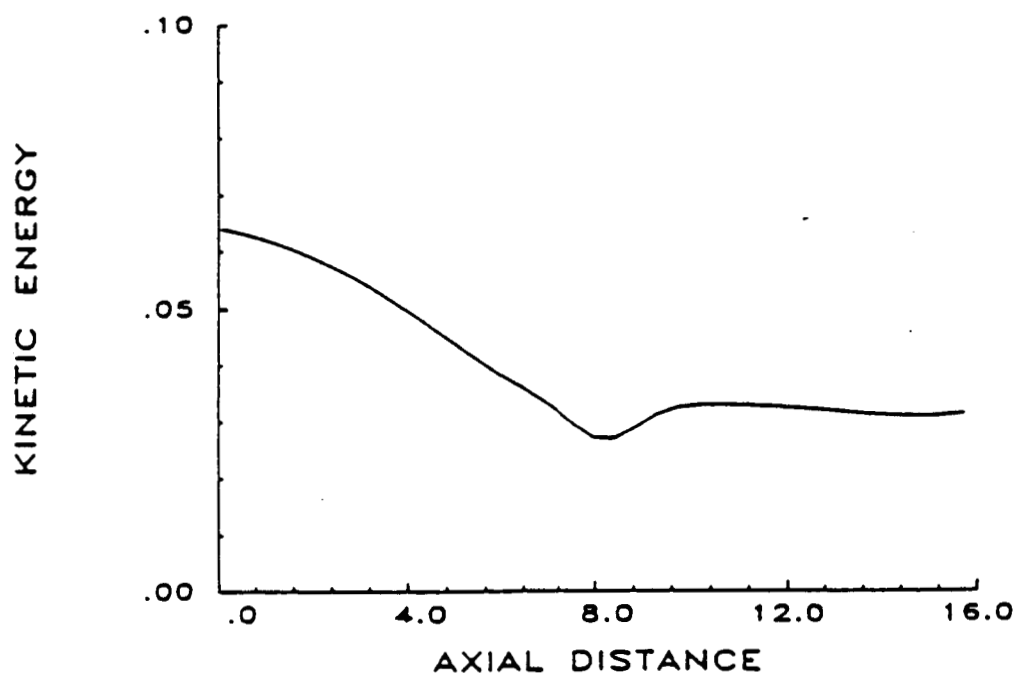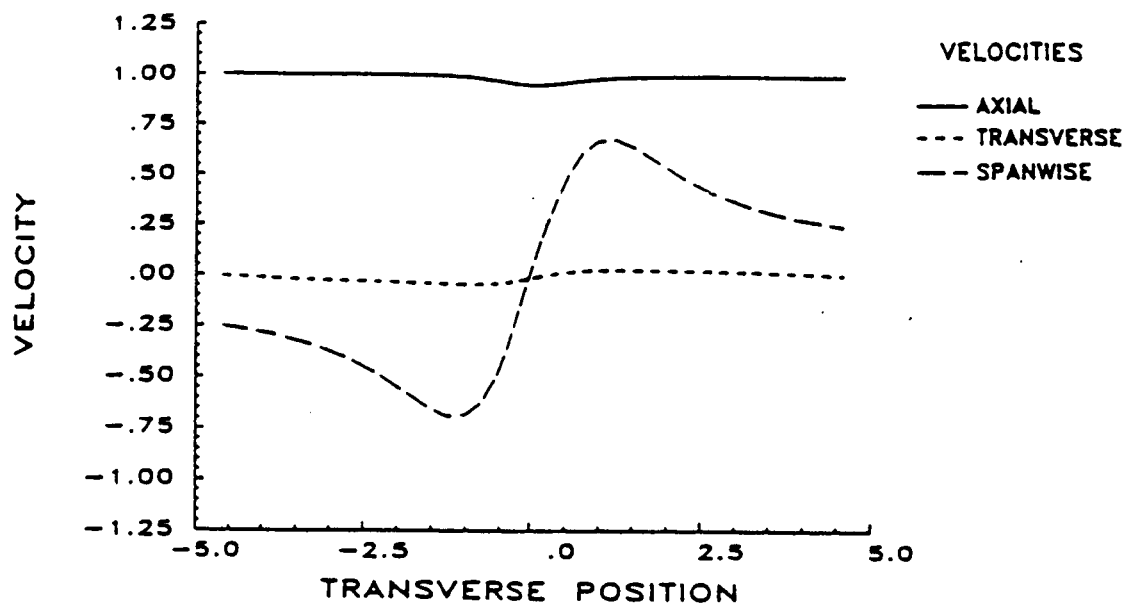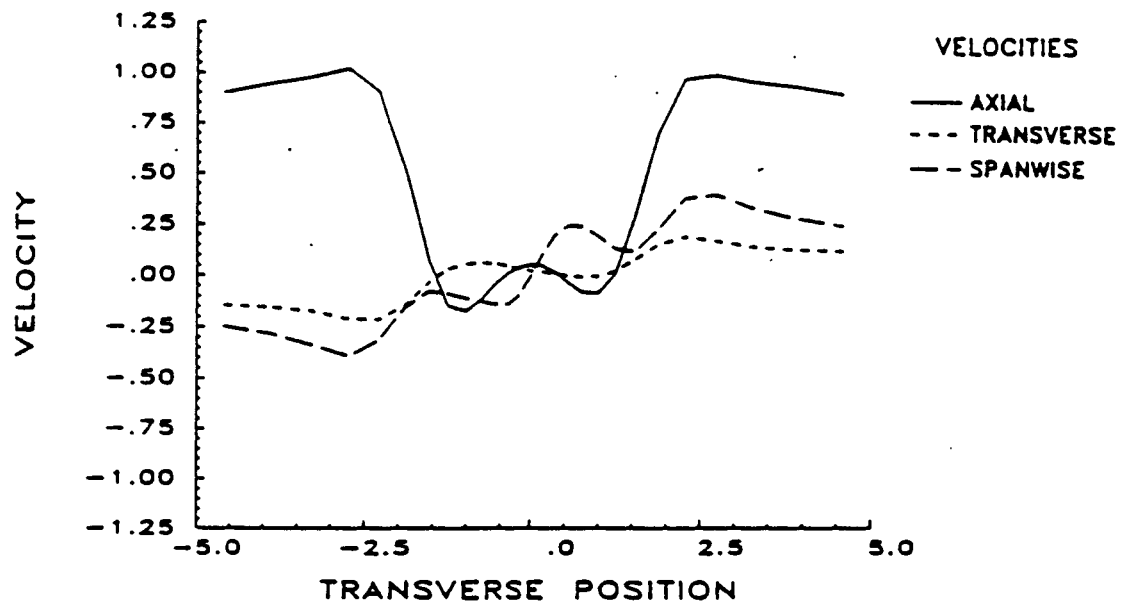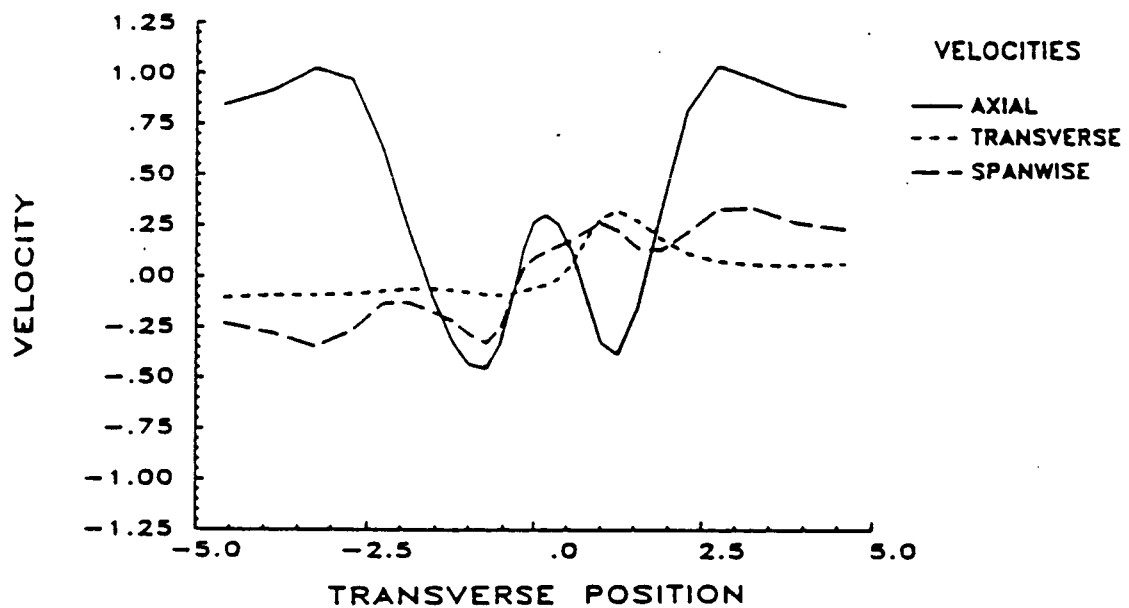

Fig. 5.31 Variation of integrated kinetic energy with axial location.
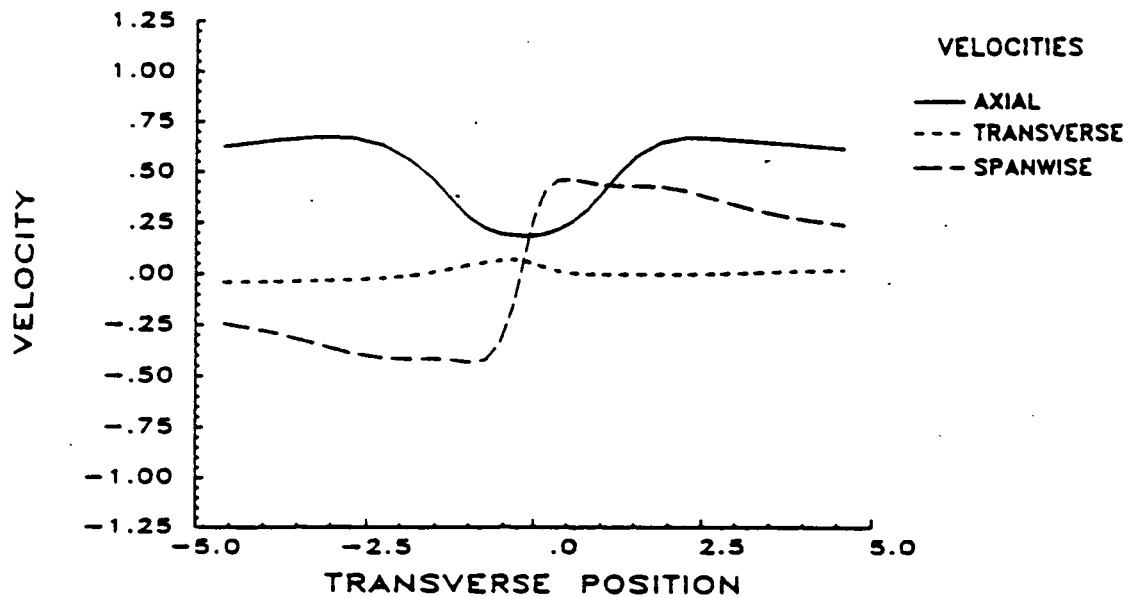
(a) x = 0.41

(b) x = 5.46

(c) x = 7.36

(d) x = 13.92

Fig. 5.32   Radial variation of axial, swirl and radial velocity
a,b,c,d.   components at different axial locations.

A comparison of this computed breakdown structure (at t=81.28) with mean streamline and axial velocity profiles constructed by Faler and Leibovich [27] using experimentally measured data is shown in Fig. 5.33. The profiles given by Faler and Leibovich are for the upper half of the bubble only. Although the Reynolds number for the experimental case was of order 1000, the overall qualitative agreement regarding the structure of the bubble is excellent.

Other Cases

Several additional test cases were computed to determine the effect of a jet-like axial velocity profile on vortex breakdown. The results, although not available in the form of line and contour plots, will be discussed for the purposes of comparison.

Several additional cases were computed in which the vortex was imbedded in a uniform external flow. For two of these cases the Rossby number at inflow was 0.80 and the Reynolds number, 225. The axial velocity profile at inflow was given by Eq. (4.6). For the two test cases, $\bar{\delta}$, was chosen as 1.0 and 0.5, respectively.

The purpose of these two computations was to determine the effect of viscous diffusion on the flow, as measured by the local Rossby number. In both cases, the local Rossby number increased in the streamwise direction as the flow evolved. This was because the rate of decrease of the solid body rotation of the vortex (near the centerline) was greater than the rate of decrease of the axial velocity component (at the radius of maximum swirl velocity). The radius, r^*, increased slightly in the streamwise direction. Breakdown did not occur, since at
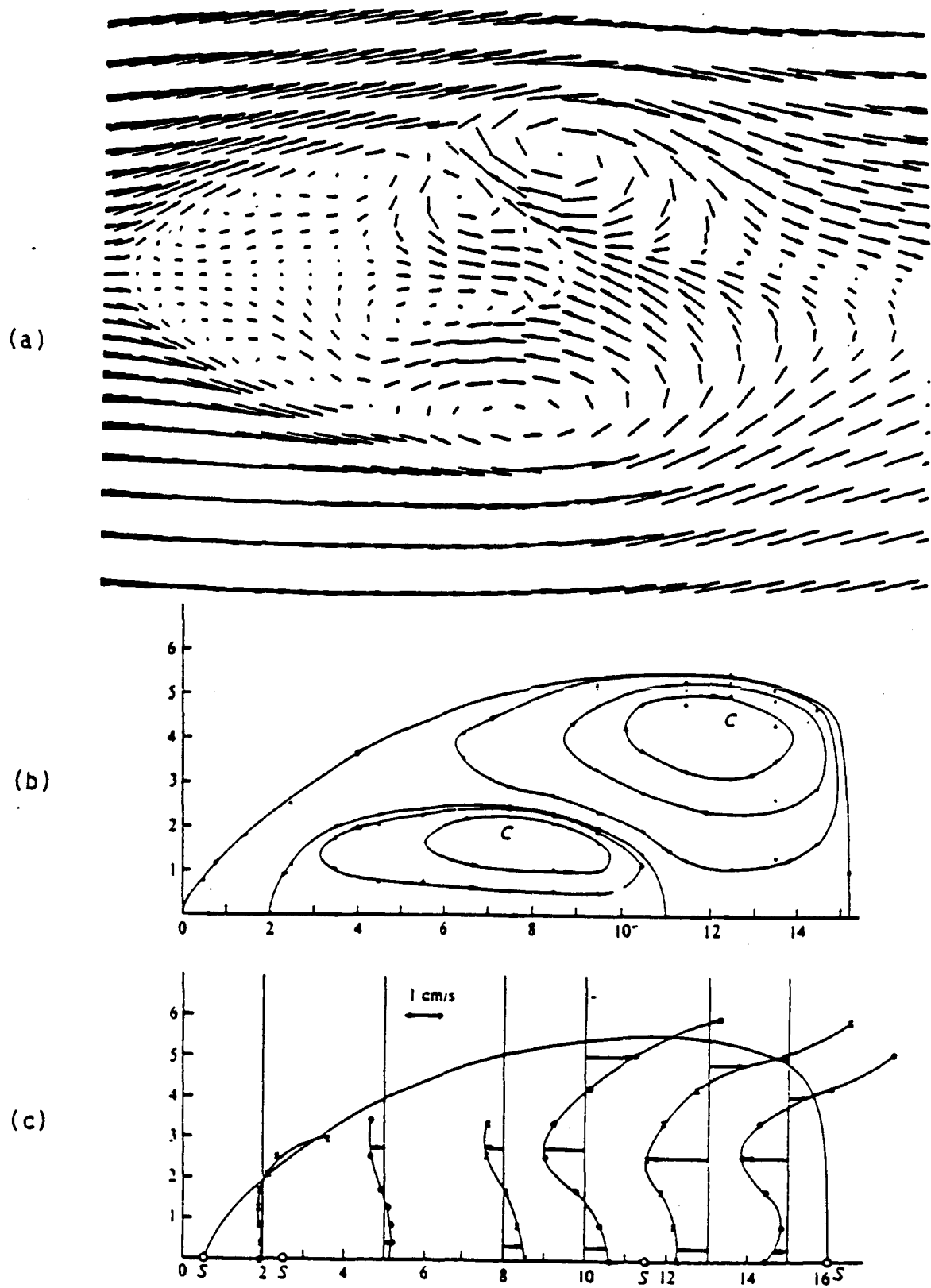
(a)

(b)

(c)

Fig. 5.33   Comparison of the numerical solution (a) at t=81.28 with
a,b,c.   experimentally determined mean streamline pattern (b) and
            mean axial velocity profiles (c) as measured by Faler and
            Leibovich (1978).

inflow the Rossby number was above critical value and, as the flow evolved, it remained supercritical everywhere.

Two additional test cases were computed with the parameter, $\bar{\sigma}$, being chosen as 1.0 and 0.5, respectively. The Reynolds number was 225 and the Rossby number at inflow, 0.625. The purpose of the tests was to determine if the jet-like axial velocity profile would delay the onset of vortex breakdown. The computations were not carried out to completion because it became apparent that breakdown would occur near the inflow boundary. This was analagous to the results that were obtained for the case Ro=0.625, Re=225 and $\bar{\delta}$ = 0.0, discussed in detail previously.

Tests to ascertain the effect of grid size and domain length on the time evolution of the solution were performed. In all cases the Rossby number and Reynolds number were maintained at values of 0.5 and 225, respectively. The vortex was imbedded in a uniform free stream. The inflow axial velocity profile was uniform. The solution was computed over three different domain lengths; 16.0, 24.0, and 32.0 (x-direction). The stretching coefficient, σ, present as a parameter in Eq. (4.16), was equal to 1.15 for the cases h_x=16.0 and h_x=24.0. For the case h_x=32 it was set equal to 1.25. This resulted in minimum cell sizes of 0.13, 0.195 and 0.46 for the domain lengths 16.0, 24.0, and 32.0, respectively. The stretching parameter ϵ, (present in Eqs. (4.17) and (4.18) for the y and z direction grids) was set equal to 4.5. The domain in the y and z direction was given by 0<y<10 and 0<z<10. In each case, the minimum axial velocity was plotted as a function of time. results were plotted in Fig. 5.34. The results showed that
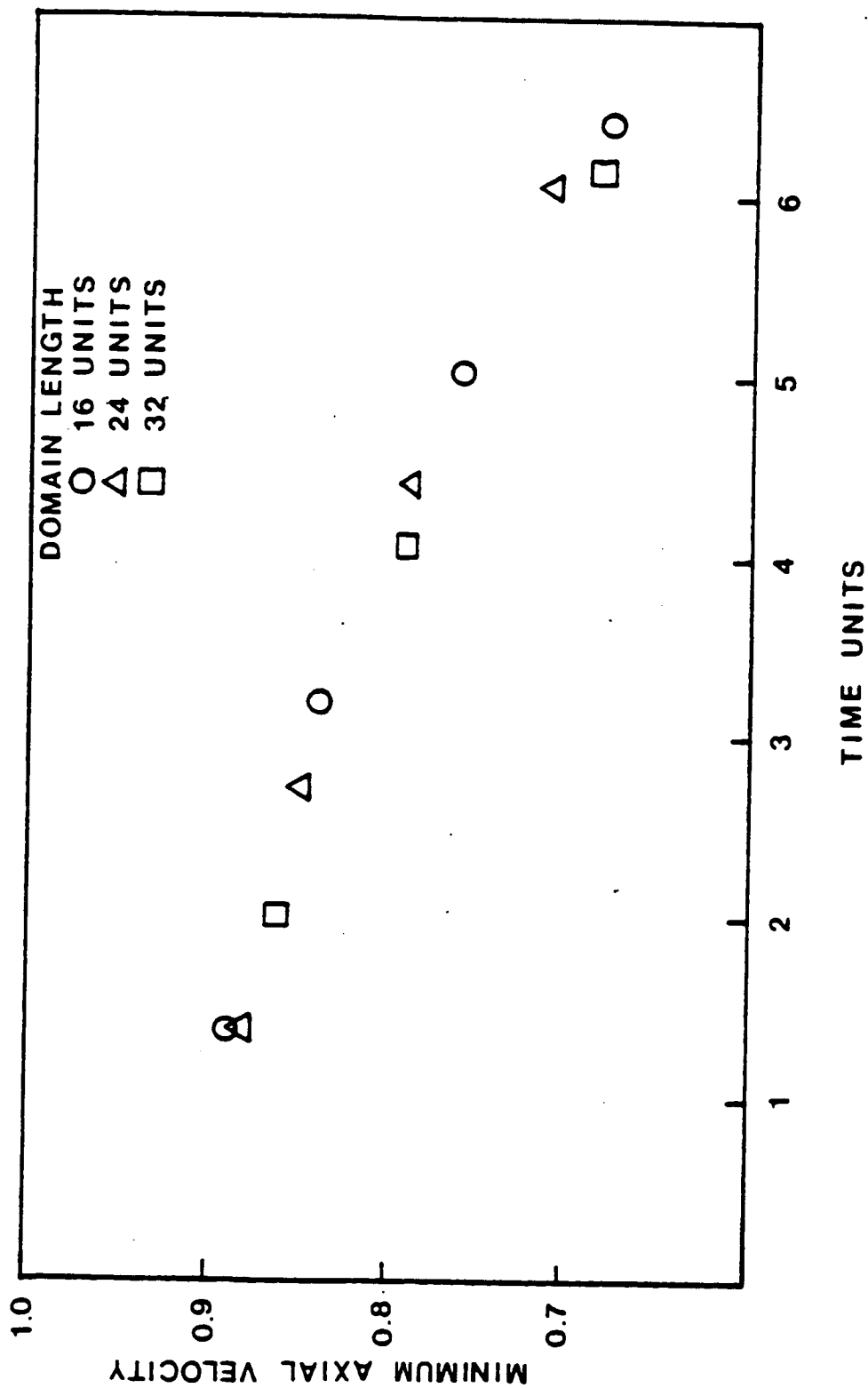
Fig. 5.34 Influence of grid spacing and computational length on the minimum axial velocity variation with time.

the effect of increased domain length and cell size had a minimal effect on the time evolution of the solution.

It has been suggested that vortex breakdown is a consequence of inertial wave disturbance on the swirling flow. The azimuthal modes (excluding n=0) of these disturbances correspond to the asymmetric internal structure of the bubble. Any flow variable can be described by Fourier series in the azimuthal (θ) direction in the form:

$$\sum_n C_n(x,r,t)\, e^{-in\theta}$$

It is of interest to examine the Fourier coefficients of the radial velocity component in front of and within the breakdown region. In order to compute the coefficients, the original data were interpolated to produce data at specified cylindrical (r,θ,x) locations. The Fourier coefficients (C_n) were then easily computed using Fast Fourier Transform techniques. For these calculations, $\Delta\theta$ was taken as ten degrees $(\pi/18)$ which resulted in 36 spacial locations along a given radius. The coefficients were tabulated in magnitude, phase angle form for the modes n=0,1,2,3. These results, for combinations of (x,r,t), appear in Tables 5.1 and 5.2. The magnitudes of the coefficients for all higher mode numbers were insignificant, thus they were not tabulated.

A brief investigation into the upstream propagation of wavelike disturbances was performed. The purpose of the tests was to determine if appropriately defined wavelike disturbances introduced at the outflow boundary would propagate upstream. Disturbances of the form

$$\partial v/\partial y/\partial w/\partial z = e^{-r^2}\, A\, \sin(2\pi\, f\cdot t) \tag{5.3}$$

Table 5.1

Complex Fourier Coefficients for the Radial Velocity Component

(x,r)	n=0	n=1	n=2	n=3
(0.56,0.5)	(0.03,0.0)	(0.01,3.11)	(0.00,-1.82)	(0.00,-3.09)
(0.56,1.0)	(0.04,0.0)	(0.01,3.09)	(0.00,-1.96)	(0.00,-0.41)
(0.56,1.5)	(0.04,0.0)	(0.01,3.14)	(0.00,-1.94)	(0.00,-0.68)
(0.56,2.0)	(0.03,0.0)	(0.00,3.04)	(0.00,-1.47)	(0.00,-0.83)
(0.56,2.5)	(0.03,0.0)	(0.00,2.95)	(0.00,-1.03)	(0.00,-0.89)
(4.15,0.5)	(0.00,3.14)	(0.00,2.94)	(0.00,-0.98)	(0.00,0.88)
(4.15,1.0)	(0.08,0.0)	(0.00,-0.78)	(0.00,-0.43)	(0.00,-2.22)
(4.15,1.5)	(0.23,0.0)	(0.01,-2.29)	(0.01,3.05)	(0.00,-0.90)
(4.15,2.0)	(0.24,0.0)	(0.01,-2.77)	(0.00,-0.91)	(0.00,-1.47)
(4.15,2.5)	(0.18,0.0)	(0.01,-2.76)	(0.00,0.66)	(0.01,-1.94)
(6.95,0.5)	(0.00,0.0)	(0.02,-2.92)	(0.00,-0.67)	(0.00,2.78)
(6.95,1.0)	(0.10,0.0)	(0.04,2.51)	(0.02,-2.40)	(0.01,-1.19)
(6.95,1.5)	(0.17,0.0)	(0.03,1.25)	(0.02,-2.83)	(0.0,-1.87)
(6.95,2.0)	(0.16,0.0)	(0.02,1.13)	(0.01,-2.60)	(0.00,-0.92)
(6.95,2.5)	(0.16,0.0)	(0.01,1.35)	(0.00,2.52)	(0.00,-0.72)
(8.62,0.5)	(0.05,0.0)	(0.05,-0.46)	(0.00,-0.75)	(0.00,-1.26)
(8.62,1.0)	(0.03,3.14)	(0.02,-1.17)	(0.00,0.07)	(0.00,2.74)
(8.62,1.5)	(0.10,3.14)	(0.02,-2.06)	(0.00,2.50)	(0.00,-2.38)
(8.62,2.0)	(0.14,3.14)	(0.03,-2.27)	(0.00,3.12)	(0.00,-2.18)
(8.62,2.5)	(0.12,3.14)	(0.03,-2.06)	(0.00,0.01)	(0.00,-3.00)
(12.40,0.5)	(0.01,3.14)	(0.07,-1.45)	(0.00,2.10)	(0.00,-0.57)
(12.40,1.0)	(0.01,3.14)	(0.04,-1.56)	(0.00,1.83)	(0.00,-0.02)
(12.40,1.5)	(0.02,3.14)	(0.03,-1.67)	(0.00,1.57)	(0.00,1.77)
(12.40,2.0)	(0.02,3.14)	(0.02,-1.71)	(0.00,1.81)	(0.00,2.45)
(12.40,2.5)	(0.01,3.14)	(0.02,-1.79)	(0.00,1.71)	(0.00,-2.17)

Table 5.2

Complex Fourier Coefficients for the Radial Velocity Component

(x,r)	n=0	n=1	n=2	n=3
(0.56,0.5)	(0.04,0.0)	(0.01,3.08)	(0.00,2.29)	(0.00,-2.39)
(0.56,1.0)	(0.05,0.0)	(0.01,3.09)	(0.00,2.42)	(0.00,-0.45)
(0.56,1.5)	(0.05,0.0)	(0.00,3.04)	(0.00,2.57)	(0.00,-0.79)
(0.56,3.0)	(0.04,0.0)	(0.00,2.93)	(0.00,2.79)	(0.00,-0.92)
(0.56,2.5)	(0.04,0.0)	(0.00,2.82)	(0.00,3.09)	(0.00,-0.92)
(4.15,0.5)	(0.02,0.0)	(0.02,-2.27)	(0.00,-2.50)	(0.00,1.55)
(4.15,1.0)	(0.02,0.0)	(0.01,-2.60)	(0.00,-1.94)	(0.00,0.71)
(4.15,1.5)	(0.19,0.0)	(0.01,-2.11)	(0.00,-1.34)	(0.00,0.87)
(4.15,2.0)	(0.27,0.0)	(0.02,-2.29)	(0.00,-0.33)	(0.00,0.29)
(4.15,2.5)	(0.23,0.0)	(0.01,-2.28)	(0.00,0.39)	(0.00,-2.54)
(6.95,0.5)	(0.01,0.0)	(0.05,2.78)	(0.01,-1.50)	(0.01,2.26)
(6.95,1.0)	(0.01,0.0)	(0.05,-2.58)	(0.01,-0.54)	(0.01,-2.90)
(6.95,1.5)	(0.00,0.0)	(0.05,-1.32)	(0.01,0.85)	(0.00,-1.97)
(6.95,2.0)	(0.03,0.0)	(0.05,-0.57)	(0.02,1.77)	(0.01,-2.56)
(6.95,2.5)	(0.13,0.0)	(0.01,0.61)	(0.01,2.91)	(0.00,-1.27)
(8.62,0.5)	(0.02,3.14)	(0.07,0.52)	(0.06,0.05)	(0.02,1.74)
(8.62,1.0)	(0.07,0.0)	(0.08,1.20)	(0.01,-0.67)	(0.01,1.74)
(8.62,1.5)	(0.07,0.0)	(0.05,1.46)	(0.01,-2.43)	(0.01,2.60)
(8.62,2.0)	(0.02,0.0)	(0.04,2.86)	(0.01,-0.00)	(0.01,-2.85)
(8.62,2.5)	(0.01,3.14)	(0.06,-3.00)	(0.03,-0.13)	(0.01,3.03)
(12.40,0.5)	(0.02,3.14)	(0.10,-1.76)	(0.00,1.96)	(0.00,1.26)
(12.40,1.0)	(0.06,3.14)	(0.05,-1.97)	(0.00,1.87)	(0.00,1.64)
(12.40,1.5)	(0.10,3.14)	(0.03,-2.35)	(0.00,2.86)	(0.00,1.89)
(12.40,2.0)	(0.11,3.14)	(0.02,-2.57)	(0.00,0.95)	(0.00,2.74)
(12.40,2.5)	(0.09,3.14)	(0.01,-2.42)	(0.00,0.48)	(0.00,-2.70)

were introduced where the amplitude A=0.03 and the frequency f=4.0. Three test cases were investigated. In two cases the vortex was imbedded in a uniform free stream. In one of these cases the Rossby number was 0.5 and in the other case the Rossby number was 0.8. In the third case the Rossby number at inflow was 0.8 and the vortex was imbedded in a decelerating flow. In each case the solution obtained with forcing at the outflow boundary was subtracted from a base flow solution. This base flow was the solution that resulted from identical inflow and initial conditions, but without forcing at outflow. For the specific forcing frequency and forcing amplitude combination applied, no disturbances were seen to propagate upstream (for time t<8). A discussion of the motivation for these tests follows.

The theories of Squire [7] and Benjamin [8] pertain to stationary disturbances present on columnar vortices. Randall and Leibovich [18] have shown that for upstream propagation to be possible, the base vortical flow must change in the axial direction. This would be the case if an adverse pressure gradient were encountered. This pressure gradient could be self-induced (through viscous-diffusion) or externally imposed. Thus the motivation for the three previously mentioned tests. That the disturbances did not propagate upstream in the cases where the vortex was imbedded in a uniform free stream was expected. These solutions were allowed to develop for 8 time units, thus the vortices remained nearly cylindrical (no variations were present in the axial direction). In the third case it was expected that some type of disturbance would have propagated upstream to the critical station. Possibly the forcing frequency/amplitude combination that was imposed resulted in waves that were damped immediately.

CONCLUSIONS

Numerical solutions of the fully three-dimensional Navier-Stokes equations were obtained for vortex breakdown. The numerical algorithm was an implementation of the velocity-vorticity formulation developed by Gatski, Grosch and Rose [39]. In this formulation, both the velocity and vorticity vectors are second order accurate in space and time. The solutions were presented for unconfined vortices of the leading edge type and were parameterized by the Rossby number and the Reynolds number. Breakdown was predictable using the local Rossby number as the critical parameter.

The present analysis supports Squire's [7] earlier conjecture that the physical mechanism responsible for breakdown is the growth of wavelike disturbances along the vortex core. The Coriolis acceleration produces a restoring force which is responsible for the creation of the disturbance waves. This effect was described in terms of the Rossby number by examining the theoretical, computational and experimental results available in the literature. The resulting correlations showed that when the Rossby number of the base vortical flow decreased to approximately 0.6, breakdown occurred.

The Rossby number criterion may find practical applications in the field of aeronautics. For instance, it would be advantageous if vortex breakdown could be induced in the case of trailing wing tip vortices

generated by commercial aircraft. Retarding vortex breakdown is desirable in the case of leading edge vortices generated by delta wing type military aircraft. In applications such as swirl combustors, the internal structure of the breakdown region is of importance. The size, shape and stability of the recirculation zone are critical to flame stability and performance. Optimal rates of entrainment and mixing could be predicted through a numerical simulation of the process.

Detailed results of vortex breakdown were obtained for two numerical simulations. In the first case, (Ro=0.625, Re=225) the vortex was imbedded in a uniform free stream. In the second case, (Ro=0.8, Re=225) the vortex was imbedded in a decelerating free stream. The internal structure of the resulting solutions differed dramatically.

The structure resulting from the first case consisted of a single, steady, nearly symmetric toroidal recirculation zone. The length of the bubble was defined by the two existing stagnation points. The structure in the second, decelerating case contained multiple internal cells, or "ring" vortices. In addition, the flow within the bubble was unsteady, asymmetric and dominated in the aft portion by large amplitude velocity fluctuations.

The discrepancy between the results of the first case and the experimental results may be attributed to the proximity of the numerical breakdown to the inflow boundary. In that case, the fixed boundary conditions at inflow act as an artifical critical barrier to the propagation of waves. At the inflow boundary, the amplitude of a standing wave grows to the extent that stagnation points and reversed flow appear along the axis. In the decelerating case, the critical condition arises from the Rossby number effect in a manner analagous to

experimental findings. The solution is not contaminated by the inflow boundary layer or by an artifical critical condition. In addition, the unsteady features of this case may be due to disturbances originating downstream since the flow was imbedded in the decelerating stream. The bubble in the first case was imbedded in a uniform free stream, thus it is expected that downstream disturbances should be damped immediately. This would account for the nearly steady features of that flow. This could not be confirmed by the tests which employed forcing at the outflow boundaries.

For the case Ro=0.8, Re=225 the radial velocity component was expanded in a complex Fourier series in the circumferential direction. An examination of the resulting Fourier coefficients $c_n(x,r,t)$ has shown that the n=0 mode is the dominant mode at a location slightly upstream of the first stagnation point for all time levels. At time level t=81.28, the magnitude of the n=1 mode in certain areas within the breakdown region is significant. At the later time level t=91.82, the magnitude of the n=1 modes within the breakdown region has increased. This indicates that the asymmetric structural features of the bubble, due primarily to n=1 mode disturbances, have been enhanced with time.

In conclusion, theoretical results, interpreted in terms of a Rossby number, give conditions favorable for the occurrence of breakdown. By considering the flow to be three-dimensional, unsteady and asymmetric, the author believes the first correct numerical representation of the internal structure of the "bubble" type breakdown was computed.

REFERENCES

1. Lugt, H. J., "Vortex Flow in Nature and Technology," John Wiley & Sons, 1983.

2. Syred, N. and Beer, J. M., "Combustion in Swirling Flows: A Review," Combustion and Flame, Vol. 23, 1974, pp. 143-201.

3. Peckham, D. H. and Atkinson, S. A., "Preliminary Results of Low Speed Wind Tunnel Tests on a Gothic Wing of Aspect Ratio 1.0," Aero. Res. Counc., CP 508, 1957, pp. 16-17.

4. Gore, R. W. and Ranz, W. E., "Backflow in Rotating Fluids Moving Axially Through Expanding Cross Sections," A.I.Ch.E. Journal, Vol. 10, 1964, pp. 83-88.

5. Barcilon, A. I., "Vortex Decay Above a Stationary Boundary," J. Fluid Mech., Vol. 27, 1967, pp. 555-559.

6. Faler, J. H. and Leibovich, S., "Distrupted States of Vortex Flow and Vortex Breakdown," Phys. Fluids, Vol. 20, 1977, pp. 1385-1400.

7. Squire, H. B., "Analysis of the 'Vortex Breakdown' Phenomenon, Part 1.," Aero. Dept., Imperial Coll., London, Rep. 102, 1960.

8. Benjamin, T. B., "Theory of the Vortex Breakdown Phenomena," J. Fluid Mech., Vol. 14, 1962, pp. 593-629.

9. Bossel, H. H., "Vortex Breakdown Flowfield, Phy. Fluids, Vol. 12, 1969, pp. 498-508.

10. Gartshore, I. S., "Recent Work in Swirling Incompressible Flow," NRC Can. Aero. Rep. LR-343, 1962.

11. Hall, M. G., "A New Approach to Vortex Breakdown," Proc. Heat Transfer Fluid Mech, Inst., 1967, Stanford Univ. Press, pp. 319-340.

12. Ludwig, H., "Zur Erklarung den Instabilit der Uber Angestellen Deltaflugen auftretenden freien Wirbelkerne," Zeitschrift fur Flugwissenschaften, Vol. 10, 1962, pp. 242-249.

13. Howard, L. N. and Gupta, A. S., "On the Hydrodynamic and Hydromagnetic Stability of Swirling Flows," J. Fluid Mech., Vol. 14, 1962, pp. 463-476.

14. Lessen, M., Singh, P. J. and Paillet, F., "The Stability of a Trailing Line Vortex. Part 1. Inviscid Theory.," J. Fluid Mech., Vol. 63, 1974, pp. 753-763.

15. Taylor, G. I., "Stability of a Viscous Liquid Contained Between Two Rotating Cylinders," Phil. Trans. Roy. Soc. Lond. Ser. A, Vol. 223, 1923, pp. 289-343.

16. Ito, T., Suematsu, Y. and Hayase, T., "On the Vortex Breakdown Phenomena in Swirling Pipe Flow," Memoirs of the Faculty of Engineering, Nagoya University, Vol. 37, 1985, pp. 117-172.

17. Tsai, C-Y, and Widnall, S. E., "Examination of Group-Velocity Criterion for Breakdown of Vortex Flow in a Diverging Duct," Phys. Fluids, Vol. 23, 1980, pp. 864-870.

18. Randall, J. D. and Leibovich, S., "The Critical State: A Trapped Wave Model of Vortex Breakdown," J. Fluid Mech., Vol. 53, 1973, pp. 495-515.

19. Garg, A. K. and Leibovich, S., "Spectral Characteristics of Vortex Breakdown Flowfields," Phys. Fluids, Vol. 22, 1979, pp. 2053-2064.

20. Kirkpatrick, D.L.T., "Experimental Investigation of the Breakdown of a Vortex in a Tube," 1964, ARC CP821.

21. Leibovich, S., "Vortex Stability and Breakdown: Survey and Extension," AIAA Journal, Vol. 22, 1984, pp. 1192-1206.

22. Rayleigh, Lord "On the Dynamics of Revolving Fluids," Proceedings of the Royal Society of London, Vol. A93, 1916, pp. 148-154.

23. Pedley, T. J., "On the Instability of Viscous Flow in a Rapidly Rotating Pipe," J. Fluid Mech., Vol. 35, 1969, pp. 97-115.

24. Harvey, J. K., "Some Observations of the Vortex Breakdown Phenomena," J. Fluid Mech., Vol. 14, 1962, pp. 585-592.

25. Sarpkaya, T., "On Stationary and Traveling Vortex Breakdown," J. Fluid Mech., Vol. 53, 1971, pp. 545-559.

26. Sarpkaya, T., "Vortex Breakdown in Swirling Conical Flows," AIAA Journal, Vol. 9, 1971, pp. 1792-1799.

27. Faler, J. H. and Leibovich, S., "An Experimental Map of the Internal Structure of a Vortex Breakdown," J. Fluid Mech., Vol. 86, 1978, pp. 313-335.

28. Sarpkaya, T., "Effect of Adverse Pressure Gradient on Vortex Breakdown", AIAA Journal, Vol. 12, 1974, pp. 602-607.

29. Delray, J., Horowitz, E., Leuchter, O. and Solignac, J. L., "Fundamental Studies on Vortex Flows," Rech. Aerosp., 1984-2, pp. 1-24.

30. Lavan, Z., Nielsen, H. and Fejer, A. A., "Separation and Flow Reversal in Swirling Flows in Circular Ducts," Phys. Fluids, Vol. 12, 1969, pp. 1747-1757.

31. Kopecky, R. M. and Torrance, K. E., "Initiation and Structure of Axisymmetric Eddies in a Rotating Stream," Computers & Fluids, Vol. 1, 1973, pp. 289-300.

32. Narin, J. P., "Numerical Prediction of Confined Swirling Jets," Computers & Fluids, Vol. 5, 1977, pp. 115-125.

33. Grabowski, W. J. and Berger, S. A., "Solutions of the Navier Stokes Equations for Vortex Breakdown," J. Fluid Mech., Vol. 75, 1976, pp. 525-544.

34. Kraus, E., Shi, X, and Hartwich, P. M., "Computation of Leading Edge Vortices," AIAA Computational Fluid Dynamics Conference, 1983, Danvers, MA. AIAA Paper No. 83-1907.

35. Benay, R., "Numerical Modeling of a Vortex Breakdown in a Laminar Flow of Revolution," Rech. Aerosp., 1984-4, 15-27.

36. Hafez, M., Kuruvila, G. and Salas, M. D., "Numerical Study of Vortex Breakdown," AIAA 24th Aerospace Sciences Meeting, 1986, Reno, Nevada, AIAA Paper No. 86-0558.

37. Mager, A., "Dissipation and Breakdown of a Wingtip Vortex," J. Fluid Mech., Vol. 55, 1972, pp. 609-628.

38. Hall, M. G., "Vortex Breakdown," Ann. Rev. Fluid Mech., Vol. 4, 1972, pp. 195-218.

39. Gatski, T. B., Grosch, C. E. and Rose, M. E., "The Numerical Solution of the Navier-Stokes Equations for 3D, Unsteady, Incompressible Flows by Compact Schemes" to be submitted.

40. Batchelor, G. K., "An Introduction to Fluid Dynamics," Cambridge University Press, 1967, pp. 555-559.

41. Uchida, S. and Nakamura, Y., "Experiments on the Axisymmetric Vortex Breakdown in a Swirling Air Flow," Trans. Japan Soc. Aero. Sci., Vol. 27, 1985, pp. 206-216.

42. Singh, P. I. and Uberoi, M. S., "Experiments on Vortex Stability," Phys. Fluids, Vol. 19, 1976, pp. 1858-1863.

43. Owen, F. K. and Peake, D. J., "Vortex Breakdown and Control Experiments in the Ames-Dryden Water Tunnel," Fluid Dynamics Panel Symposium on Aerodynamics and Related Hydrodynamic Studies Using Water Facilities, Monterey, CA, 20-23 October 1986.

44. Anders, K. "LDV Measurements of the Velocity Field of a Leading Edge Delta Wing Before and After Vortex Breakdown," von Karman Institute for Fluid Dynamics, Tech. Note 142, March 1982.

45. Verhaagen, N. G. and Kruisbrink, A. C., "The Entrainment Effect of a Leading Edge Vortex," AIAA 18th Fluid Dynamics and Plasma Dynamics and Laser Dynamics Conference, Cincinnati, OH, July 16-18, 1985, Paper No. 85-1584.

46. Orszag, S. A., Israeli, M. and Deville, M. O., "Boundary Conditions for Incompressible Flows," Journal of Scientific Computing, Vol. 1, 1986, pp. 75-111.

47. Fix, G. J. and Rose, M. E., "A Comparative Study of Finite Element and Finite Difference Methods for Cauchy-Riemann Type Equations," SIAM J. Numer. Anal., Vol. 22, 1985, pp. 250-261.

48. Kaczmarz, S., "Angenaherte Auflosung von Systemen Linear Gleichungen," Bull. Acad. Pol. Sci. Lett., A, 1937, pp. 355-357.

49. Tanabe, K., "Projection Method for Solving a Singular System of Linear Equations and its Applications," Numer. Math., Vol. 17, 1971, pp. 203-214.

50. McInville, R. M., "Numerical and Experimental Investigation of Forced Laminar Free Shear Layers and Turbulent Slot Injection Flows," PhD Dissertation, Dept. of Mechanical and Aerospace Engineering, North Carolina State University, 1985.

51. Gatski, T. B., Grosch, C. E. and Rose, M. E., "A Numerical Study of the Two Dimensional Navier-Stokes Equations in Vorticity-Velocity Variables" J. Comp. Physics, Vol. 48, 1982.

52. Anderson, D. A., Tannehill, J. C. and Pletcher, R. H., "Computational Fluid Mechanics and Heat Transfer," McGraw-Hill Book Company, 1984, pp. 247-252.

53. Courant, R., Friedrichs, K. and Lewy, H., "On the Partial Difference Equations of Mathematical Physics," IBM Journal, March, 1967, pp. 215-234.

54. Rose, M. E., "Pressure Calculation for Incompressible Flows," Proc. of Workshop in CFD, University of California at Davis, June 1986.

55. Hall, M. G., "The Structure of Concentrated Vortex Cores," Progress in Aeronautical Sciences, Vol. 7, 1966, pp. 53-110.

APPENDICES

APPENDIX A

EXPONENTIAL TRANSFORMATION

Gatski, Grosch and Rose [39] employ an exponential transformation of the form

$$\omega^i = e^{[B_n(t-t_n)]} \zeta^i \tag{A1}$$

where $[B_n]$ is a constant matrix, to eliminate the explicit appearance of the vortex stretching term from the vorticity transport equation. The procedure is outlined below.

The vorticity transport equation is written in the form

$$\frac{\partial \omega^i}{\partial t} + u_j \omega^i{}_{,j} - \omega^j u^i{}_{,j} = \nu \omega^i{}_{,jj} \tag{A2}$$

let $u^i{}_{,j} = B_n$, a constant at time level n. Introduce $\omega^i = e^{B_n(t-t_n)} \zeta^i$ into the above equation. This results in the following transformed equation.

$$B_n e^{[B_n(t-t_n)]} \zeta^i + e^{[B_n(t-t_n)]} \frac{\partial \zeta^i}{\partial t} + e^{[B_n(t-t_n)]} u_j \zeta^i{}_{,j}$$

$$- B_n e^{[B_n(t-t_n)]} \zeta^j = \nu e^{[B_n(t-t_n)]} \zeta^i{}_{,jj} \tag{A3}$$

It is apparent that the vortex stretching term is eliminated through the time derivative. The resulting equation appears below.

$$\frac{\partial \zeta^i}{\partial t} + u_j \zeta^i{}_{,j} = \nu \zeta^i{}_{,jj} \tag{A4}$$

APPENDIX B

REDUCTION OF X-SWEEP VORTICITY EQUATIONS TO TRIDIAGONAL FORM

The reduction of the x-sweep vorticity equations to tridiagonal form is shown below. For the sake of clarity only appropriate indices are expressed. The derivation of the y and z sweeps are analogous, with only the final results being expressed.

The 3-D advection diffusion equation for the transformed vorticity and the necessary averaging conditions appears below as Eqs. (B1) to (B14). Note that the (u,v,w) velocity components represent averages at cell centers.

$$\delta_t \bar{\zeta} + u\delta_x \bar{\zeta} + v\delta_y \bar{\zeta} + w\delta_z \bar{\zeta} = \nu(\delta_x \bar{\phi} + \delta_y \bar{\psi} + \delta_t \bar{\xi}) \tag{B1}$$

$$(\mu_x - h_x q_x \delta_x) \bar{\phi} = \delta_x \bar{\zeta} \tag{B2}$$

$$(\mu_y - h_y q_y \delta_y) \bar{\psi} = \delta_y \bar{\zeta} \tag{B3}$$

$$(\mu_z - h_z q_x \delta_z) \bar{\xi} = \delta_z \bar{\zeta} \tag{B4}$$

$$\mu_t \bar{\zeta} = \mu_x \bar{\zeta} - h^2_x p_x \delta_x \bar{\phi} \tag{B5}$$

$$\mu_t \bar{\zeta} = \mu_y \bar{\zeta} - h^2_y p_y \delta_y \bar{\psi} \tag{B6}$$

$$\mu_t \bar{\zeta} = \mu_z \bar{\zeta} - h^2_z p_z \delta_z \bar{\xi} \tag{B7}$$

where

$$h_x = \frac{\Delta x}{2} \tag{B8}$$

$$h_y = \frac{\Delta y}{2} \tag{B9}$$

$$h_z = \frac{\Delta z}{2} \tag{B10}$$

$$p_x = \frac{q(\theta_x)}{\theta_x} \tag{B11}$$

$$p_y = \frac{q(\theta_y)}{\theta_y} \tag{B12}$$

$$p_z = \frac{q(\theta_z)}{\theta_z} \tag{B13}$$

$$\text{and, } \tau = \frac{\Delta t}{2} \tag{B14}.$$

The first step is to eliminate the $n+\frac{1}{2}$ time level dependence from equation (B1) as follows. Combine the identity

$$\tau \delta_t \bar{\zeta} = \mu_t \bar{\zeta} - \bar{\zeta}^{n-\frac{1}{2}} \tag{B15}$$

with Eqs. (B5) through (7) to obtain the following three vector equations.

$$\tau \delta_t \bar{\zeta} = \mu_x \bar{\zeta} - h^2_x p_x \delta_x \bar{\phi} - \bar{\zeta}^{n-\frac{1}{2}} \tag{B16}$$

$$\tau \delta_t \bar{\zeta} = \mu_y \bar{\zeta} - h^2_y p_y \delta_y \bar{\psi} - \bar{\zeta}^{n-\frac{1}{2}} \tag{B17}$$

$$\tau \delta_t \bar{\zeta} = \mu_t \bar{\zeta} - h^2_z p_z \delta_z \bar{\xi} - \bar{\zeta}^{n-\frac{1}{2}} \tag{B18}$$

When Eqs. (B16) to (B18) are each combined with Eq. (B1), three systems of equations result, each of which can be solved simultaneously for a component of the viscous terms $\delta_x \bar{\phi}$, $\delta_y \bar{\psi}$ and $\delta_z \bar{\xi}$. The systems appear below as Eq. (B20).

$$\nu\tau \begin{vmatrix} K_x & 1 & 1 \\ 1 & K_y & 1 \\ 1 & 1 & K_z \end{vmatrix} \begin{matrix} \delta_x \bar{\phi} \\ \delta_y \bar{\psi} \\ \delta_z \bar{\xi} \end{matrix} = \tau \begin{vmatrix} 1 & 1 & 1 \\ 1 & 1 & 1 \\ 1 & 1 & 1 \end{vmatrix} \begin{matrix} u\delta_x \zeta \\ v\delta_y \bar{\zeta} \\ w\delta_z \bar{\zeta} \end{matrix} +$$

$$+ \begin{vmatrix} 1 & 0 & 0 \\ 0 & 1 & 0 \\ 0 & 0 & 1 \end{vmatrix} \begin{matrix} \mu_x \bar{\zeta} - \zeta \ ^{n-1/2} \\ \mu_y \bar{\zeta} - \zeta \ ^{n-1/2} \\ \mu_x \bar{\zeta} - \zeta \ ^{n-1/2} \end{matrix} \tag{B19}$$

where

$$K_x = \frac{h_x^2 p_x}{\nu \tau} + 1 \tag{B20}$$

$$K_y = \frac{h_y^2 p_y}{\nu \tau} + 1 \tag{B21}$$

$$K_z = \frac{h_z^2 p_z}{\nu \tau} + 1 \tag{B22}$$

Take the inverse of the matrix on the left side of Eq. (B19). This is given as

$$\frac{1}{\beta} \begin{vmatrix} \alpha_{11} & \alpha_{12} & \alpha_{13} \\ \alpha_{21} & \alpha_{22} & \alpha_{23} \\ \alpha_{31} & \alpha_{32} & \alpha_{33} \end{vmatrix} \tag{B23}$$

where

$$\beta = 2 + K_x K_y K_z - (K_x + K_y + K_z) \tag{B24}$$

$$\alpha_{11} = (K_y K_z - 1) \tag{B25}$$

$$\alpha_{12} = - (K_z - 1) \tag{B26}$$

$$\alpha_{13} = (1 - K_y) \tag{B27}$$

$$\alpha_{21} = -(K_z - 1) \tag{B28}$$

$$\alpha_{22} = (K_x K_z - 1) \tag{B29}$$

$$\alpha_{23} = -(K_x - 1) \tag{B30}$$

$$\alpha_{31} = (1 - K_y) \tag{B31}$$

$$\alpha_{32} = -(K_x - 1) \tag{B32}$$

$$\alpha_{33} = (K_x K_y - 1) \tag{B33}$$

Multiply matrix Eq. (B19) by matrix (B23). This results in the following expressions for the viscous terms.

$$\delta_x \bar{\phi} = \frac{1}{\beta \nu \tau} \{ \alpha_{11}(\mu_x \bar{\zeta} - \bar{\zeta}^{n-1/2}) + \alpha_{12}(\mu_y \bar{\zeta} - \bar{\zeta}^{n-1/2})$$

$$+ \alpha_{13}(\mu_z \bar{\zeta} - \bar{\zeta}^{n-1/2}) \}$$

$$+ \frac{1}{\nu \beta}(\alpha_{11} + \alpha_{12} + \alpha_{13})(u\delta_x \bar{\zeta} + v\delta_y \bar{\zeta} + w\delta_z \bar{\zeta}) \tag{B34}$$

$$\delta_y \bar{\psi} = \frac{1}{\beta \nu \tau} \{ \alpha_{21}(\mu_x \bar{\zeta} - \bar{\zeta}^{n-1/2}) + \alpha_{22}(\mu_y \bar{\omega} - \bar{\zeta}^{n-1/2})$$

$$+ \alpha_{23}(\mu_z \bar{\omega} - \bar{\zeta}^{n-1/2}) \}$$

$$+ \frac{1}{\nu \beta}(\alpha_{21} + \alpha_{22} + \alpha_{23})(u\delta_x \bar{\zeta} + v\delta_y \bar{\zeta} + w\delta_z \bar{\zeta}) \tag{B35}$$

$$\delta_z \bar{\xi} = \frac{1}{\beta \nu \tau} \{ \alpha_{31}(\mu_x \bar{\zeta} - \bar{\zeta}^{n-1/2}) + \alpha_{32}(\mu_y \bar{\zeta} - \bar{\zeta}^{n-1/2})$$

$$+ \alpha_{33}(\mu_z \bar{\zeta} - \bar{\zeta}^{n-1/2}) \}$$

$$+ \frac{1}{\nu \beta}(\alpha_{31} + \alpha_{32} + \alpha_{33})(u\delta_x \bar{\zeta} + v\delta_y \bar{\zeta} + w\delta_z \bar{\zeta}) \tag{B36}$$

Only Eq. (B34) is needed for the derivation of the x-sweep tridiagional system. Equations (B35] and (B36) are needed for the y-sweep and z-sweep derivations respectively. Performing the difference operation indicated on the left side of Eq. (B34) results in the following expression

$$(\bar{\phi}_{i+1/2} - \bar{\phi}_{i-1/2}) = \frac{2}{\beta\nu\lambda_x} \{\alpha_{11} (\mu_x\bar{\zeta} - \bar{\zeta}^{n-1/2})$$

$$+ \alpha_{12}(\mu_y\bar{\zeta} - \bar{\zeta}^{n-1/2}) + \alpha_{13}(\mu_z\bar{\zeta} - \bar{\zeta}^{n-1/2})\}$$

$$+ \frac{\Delta x}{\beta\nu} (\alpha_{11} + \alpha_{12} + \alpha_{13})(u\delta_x\bar{\zeta} + v\delta_y\bar{\zeta} + w\delta_z\bar{\zeta}) \qquad (B37)$$

where $$\lambda_x = \frac{\Delta t}{\Delta x}. \qquad (B38)$$

Let $$\gamma_x^{\pm} = \frac{1}{2}(1 \pm q(\theta_x)) \qquad (B39)$$

The appropriate combination of Eq. (B2) and Eq. (B39) results in the following expression for $\bar{\phi}_{i-1/2}$

$$\gamma_x^+ \bar{\phi}_{i-1/2} = \delta_x\bar{\zeta} - \gamma_x^- \bar{\phi}_{i+1/2} . \qquad (B40)$$

Multiply each side of Eq. (B37) by γ_x^+ and substitute the result into Eq. (B40). The resulting expression for $\bar{\phi}_{i+1/2}$ is given as,

$$\bar{\phi}_{i+1/2} = \frac{2\gamma_x^+}{\beta\nu\lambda_x} \{\alpha_{11} (\mu_x\bar{\zeta} - \bar{\zeta}^{n-1/2}) + \alpha_{12}(\mu_y\bar{\zeta} - \bar{\zeta}^{n-1/2})$$

$$+ \alpha_{13}(\mu_z\bar{\zeta} - \bar{\zeta}^{n-1/2})\}$$

$$+ \left[\frac{u\gamma_x^+ \Delta x}{\nu\beta} (\alpha_{11} + \alpha_{12} + \alpha_{13}) + 1 \right] \delta_x \bar{\zeta}$$

$$+ \frac{\gamma_x^+ \Delta x}{\nu\beta} (\alpha_{11} + \alpha_{12} + \alpha_{13})[\nu\delta_y\bar{\zeta} + w\delta_z\bar{\zeta}] \qquad (B41)$$

The expression for $\bar{\phi}_{i-1/2}$, obtained in a similar manner, appears below.

$$\phi_{i-1/2} = \frac{-2\gamma_x^-}{\beta\nu\lambda_x} \{ \alpha_{11}(\mu_x\bar{\zeta} - \bar{\zeta}^{n-1/2}) + \alpha_{12} (\mu_y\bar{\zeta} - \bar{\zeta}^{n-1/2})$$

$$+ \alpha_{13} (\mu_z\bar{\zeta} - \bar{\zeta}^{n-1/2}) \}$$

$$+ \left[\frac{-u\gamma_x^- \Delta x}{\nu\beta} (\alpha_{11} + \alpha_{12} + \alpha_{13}) + 1 \right] \delta_x\bar{\zeta}$$

$$- \frac{\gamma_x^+ \Delta x}{\nu\beta} (\alpha_{11} + \alpha_{12} + \alpha_{13})[\nu\delta_y\bar{\zeta} + w\delta_z\bar{\zeta}] \qquad (B42)$$

Index Eq. (B42) by i+1 and equate fluxes of ϕ across a cell face to obtain the following equality.

$$- c^- \alpha_{11} \mu_x\bar{\zeta}\big|_{i+1} - c^+ \alpha_{11} \mu_x\bar{\zeta}\big|_i$$

$$+ [- uR^- (\alpha_{11} + \alpha_{12} \alpha_{13}) + 1]\delta_x\bar{\zeta}\big|_{i+1}$$

$$- [uR^+ (\alpha_{11} + \alpha_{12} \alpha_{13}) + 1]\delta_x\bar{\zeta}\big|_i$$

$$= c^- \alpha_{12}(\mu_y\bar{\zeta} - \bar{\zeta}^{n-1/2})\big|_{i+1}$$

$$+ C^+ \alpha_{12} (\mu_y \bar{\zeta} - \bar{\zeta}^{\,n-1/2}) \Big|_i$$

$$+ C^- \alpha_{13} (\mu_z \bar{\zeta} - \bar{\zeta}^{\,n-1/2}) \Big|_{i+1}$$

$$+ C^+ \alpha_{13} (\mu_z \bar{\zeta} - \bar{\zeta}^{\,n-1/2}) \Big|_i$$

$$- C^- \alpha_{11} \bar{\zeta}^{\,n-1/2} \Big|_{i+1} - C^+ \alpha_{11} \bar{\zeta}^{\,n-1/2} \Big|_i$$

$$+ R^- (\alpha_{11} + \alpha_{12} + \alpha_{13}) [v \delta_y \bar{\zeta} + w \delta_z \bar{\zeta}] \Big|_{i+1}$$

$$+ R^+ (\alpha_{11} + \alpha_{12} + \alpha_{13}) [v \delta_y \bar{\zeta} + w \delta_z \bar{\zeta}] \Big|_i \tag{B43}$$

where
$$C^\pm = \frac{2 \gamma_x^\pm}{\beta v \lambda_x} \tag{B44}$$

and
$$R^\pm = \frac{\gamma_x^\pm \Delta x}{\beta v} \tag{B45}$$

Performing the discretizations, rearranging and redefining $\gamma_x^\pm$ as

$$\gamma_x^\pm = 1 \pm q(\theta_x) \tag{B46}$$

results in the tridiagonal form of the equations for the x sweep given below.

$$- \lambda_{i+1}^{-1} \left[\gamma_x^- \left(\frac{\alpha_{11}}{\beta} + \frac{\bar{\alpha}_1 u \lambda_x}{\beta} \right) - S_x \right]\Big|_{i+1} \bar{\zeta}_{i+3/2}$$

$$+ \left\{ - \lambda_{i+1}^{-1} \left[\gamma_x^- \left(\frac{\alpha_{11}}{\beta} - \frac{\bar{\alpha}_1 u \lambda_x}{\beta} \right) + S_x \right]\Big|_{i+1} \right.$$

$$- \lambda_i^{-1} [\gamma_x^- (\frac{\alpha_{11}}{\beta} + \frac{\bar{\alpha}_1 u \lambda_x}{\beta}) + S_x]|_i \} \ \bar{\zeta}_{i+1/2}$$

$$- \lambda_i^{-1} [\gamma_x^+ (\frac{\alpha_{11}}{\beta} - \frac{\bar{\alpha}_1 u \lambda_x}{\beta}) - S_x]|_i \ \bar{\zeta}_{1-1/2}$$

$$= \frac{2\gamma_x^- \ \bar{\alpha}_i}{\lambda_x \ \beta}\Big|_{i+1} \ \bar{\zeta}_{i+1}^{n-1/2} - \frac{2\gamma_x^- \ \bar{\alpha}_i}{\lambda_x \beta}\Big|_i \ \bar{\zeta}_i^{\ n-1/2}$$

$$+ \frac{\gamma_x^-}{\lambda_x} (\frac{\alpha_{12}}{\beta} + \frac{\bar{\alpha}_1 v \lambda_y}{\beta})\Big|_{i+1} \ \bar{\zeta}_{i+1,j+1/2}$$

$$+ \frac{\gamma_x^-}{\lambda_x} (\frac{\alpha_{12}}{\beta} - \frac{\bar{\alpha}_1 v \lambda_y}{\beta})\Big|_{i+1} \ \bar{\zeta}_{i+1,j-1/2}$$

$$+ \frac{\gamma_x^+}{\lambda_x} (\frac{\alpha_{12}}{\beta} + \frac{\bar{\alpha}_1 v \lambda_y}{\beta})\Big|_i \ \bar{\zeta}_{i,j+1/2}$$

$$+ \frac{\gamma_x^+}{\lambda_x} (\frac{\alpha_{12}}{\beta} - \frac{\bar{\alpha}_1 v \lambda_y}{\beta})\Big|_i \ \bar{\zeta}_{i,j-1/2}$$

$$+ \frac{\gamma_x^-}{\lambda_x} \frac{\alpha_{13}}{\beta} + \frac{\bar{\alpha}_1 w \lambda_z}{\beta})\Big|_{i+1} \ \bar{\zeta}_{i+1,k+1/2}$$

$$+ \frac{\gamma_x^-}{\lambda_x} (\frac{\alpha_{13}}{\beta} - \frac{\bar{\alpha}_1 w \lambda_z}{\beta})\Big|_{i+1} \ \bar{\zeta}_{i+1,k-1/2}$$

$$+ \frac{\gamma_x^+}{\lambda_x} (\frac{\alpha_{13}}{\beta} + \frac{\bar{\alpha}_1 w \lambda_z}{\beta})\Big|_i \ \bar{\zeta}_{i,k+1/2}$$

$$+ \frac{\gamma_x^+}{\lambda_x} \left(\frac{\alpha_{13}}{\beta} - \frac{\bar{\alpha}_1 w \lambda_z}{\beta} \right) \Big|_i \; \omega_{i,k-\frac{1}{2}} \tag{B47}$$

where
$$\bar{\alpha}_1 = \alpha_{11} + \alpha_{12} + \alpha_{13} \tag{B48}$$

and
$$S_x = \frac{2\nu\lambda_x}{\Delta x} \tag{B49}$$

The tridiagonal equation for the y sweep takes the form

$$- \lambda_{j+1}^{-1} \left[\gamma_y^- \left(\frac{\alpha_{22}}{\beta} + \frac{\bar{\alpha}_2 \nu \lambda_y}{\beta} - S_y \right) \right] \Big|_{j+1} \bar{\zeta}_{j+3/2}$$

$$+ \left\{ - \lambda_{j+1}^{-1} \left[\gamma_y^- \left(\frac{\alpha_{22}}{\beta} - \frac{\bar{\alpha}_2 \nu \lambda_y}{\beta} \right) + S_y \right] \Big|_{j+1} \right.$$

$$- \lambda_j^{-1} \left[\gamma_y^+ \left(\frac{\alpha_{22}}{\beta} + \frac{\bar{\alpha}_2 \nu \lambda_y}{\beta} \right) + S_y \right] \Big|_j \right\} \bar{\zeta}_{j+\frac{1}{2}}$$

$$- \lambda_j^{-1} \left[\gamma_y^+ \left(\frac{\alpha_{22}}{\beta} - \frac{\bar{\alpha}_2 \nu \lambda_y}{\beta} \right) - S_y \right] \Big|_j \bar{\zeta}_{j-\frac{1}{2}}$$

$$= \frac{-2\gamma_y^- \bar{\alpha}_2}{\lambda_y \beta} \Big|_{j+1} \bar{\zeta}_{j+1}^{n-\frac{1}{2}} - \frac{\partial \gamma_y^- \bar{\alpha}_2}{\lambda_y \beta} \Big|_j \bar{\zeta}_j^{n-\frac{1}{2}}$$

$$+ \frac{\bar{\gamma}_y}{\lambda_y} \left(\frac{\alpha_{21}}{\beta} + \frac{\bar{\alpha}_2 u \lambda_x}{\beta} \right) \Big|_{j+1} \bar{\zeta}_{i+\frac{1}{2},j+1}$$

$$+ \frac{\bar{\gamma}_y}{\lambda_y} \left(\frac{\alpha_{21}}{\beta} - \frac{\bar{\alpha}_2 u \lambda_x}{\beta} \right) \Big|_{j+1} \bar{\zeta}_{i-\frac{1}{2},j+1}$$

128

$$+ \frac{\gamma_y^+}{\lambda_y} \left(\frac{\alpha_{21}}{\beta} + \frac{\bar{\alpha}_2 u \lambda_x}{\beta}\right)\bigg|_j \bar{\zeta}_{i+1/2,j}$$

$$+ \frac{\gamma_y^+}{\lambda_y} \left(\frac{\alpha_{21}}{\beta} - \frac{\bar{\alpha}_2 u \lambda_x}{\beta}\right)\bigg|_j \bar{\zeta}_{i-1/2,j}$$

$$+ \frac{\gamma_y^-}{\lambda_y} \left(\frac{\alpha_{23}}{\beta} + \frac{\bar{\alpha}_2 w \lambda_z}{\beta}\right)\bigg|_{j+1} \bar{\zeta}_{j+1,k+1/2}$$

$$+ \frac{\gamma_y^-}{\lambda_y} \left(\frac{\alpha_{23}}{\beta} - \frac{\bar{\alpha}_2 w \lambda_z}{\beta}\right)\bigg|_{j+1} \bar{\zeta}_{j+1,k-1/2}$$

$$+ \frac{\gamma_y^+}{\lambda_y} \left(\frac{\alpha_{23}}{\beta} + \frac{\bar{\alpha}_2 w \lambda_z}{\beta}\right)\bigg|_j \bar{\zeta}_{j,\ k+1/2}$$

$$+ \frac{\gamma_y^+}{\lambda_y} \left(\frac{\alpha_{23}}{\beta} + \frac{\bar{\alpha}_2 w \lambda_z}{\beta}\right)\bigg|_j \bar{\zeta}_{j,\ k-1/2} \tag{B50}$$

where $\qquad \bar{\alpha}_2 = \alpha_{21} + \alpha_{22} + \alpha_{23}$ $\qquad\qquad\qquad$ (B51)

and $\qquad S_y = \frac{2\nu\lambda_y}{\Delta y}$ $\qquad\qquad\qquad\qquad\qquad$ (B52)

The tridiagonal equation for the z-sweep takes the form

$$- \lambda^{-1}_{k+1} \left[\gamma_z^- \left(\frac{\alpha_{33}}{\beta} + \frac{\bar{\alpha}_3 w \lambda_z}{\beta}\right) - S_z\right]\bigg|_{k+1} \bar{\zeta}_{k+3/2}$$

$$+ \left\{ - \lambda^{-1}_{k+1} \left[\gamma_z^- \left(\frac{\alpha_{33}}{\beta} - \frac{\bar{\alpha}_3 w \lambda_z}{\beta}\right) + S_z\right]\bigg|_{k+1} \right.$$

$$-\lambda^{-1}{}_k \left[\gamma^-_z \left(\frac{\alpha_{33}}{\beta} + \frac{\bar{\alpha}_3 w \lambda_z}{\beta} \right) + S_z \right]\Big|_k \} \ \bar{\xi}_{k+1/2}$$

$$- \lambda^{-1}{}_k \left[\gamma^-_z \left(\frac{\alpha_{33}}{\beta} - \frac{\bar{\alpha}_3 w \lambda_z}{\beta} \right) - S_z \right]\Big|_k \ \bar{\xi}_{k-1/2}$$

$$= - \frac{2\gamma^-_z \bar{\alpha}_3}{\lambda_z \beta}\Big|_{k+1} \bar{\zeta}_{k+1}^{n-1/2} - \frac{2\gamma^-_z \bar{\alpha}_3}{\lambda_z \beta}\Big|_k \bar{\zeta}_k^{n-1/2}$$

$$+ \frac{\gamma^-_z}{\lambda_z} \left(\frac{\alpha_{31}}{\beta} + \frac{\bar{\alpha}_3 u \lambda_x}{\beta} \right)\Big|_{k+1} \ \bar{\zeta}_{i+1/2,k+1}$$

$$+ \frac{\gamma^-_z}{\lambda_z} \left(\frac{\alpha_{31}}{\beta} - \frac{\bar{\alpha}_3 u \lambda_x}{\beta} \right)\Big|_{k+1} \ \bar{\zeta}_{1-1/2,k+1}$$

$$+ \frac{\gamma^-_z}{\lambda_z} \left(\frac{\alpha_{31}}{\beta} + \frac{\bar{\alpha}_3 u \lambda_x}{\beta} \right)\Big|_k \ \bar{\zeta}_{i+1/2,k}$$

$$+ \frac{\gamma^-_z}{\lambda_z} \left(\frac{\alpha_{31}}{\beta} - \frac{\bar{\alpha}_3 u \lambda_x}{\beta} \right)\Big|_k \ \bar{\zeta}_{i-1/2,k}$$

$$= \frac{\gamma^-_z}{\lambda_z} \left(\frac{\alpha_{32}}{\beta} + \frac{\bar{\alpha}_3 v \lambda_y}{\beta} \right)\Big|_{k+1} \ \bar{\zeta}_{j+1/2,k+1}$$

$$+ \frac{\gamma^-_z}{\lambda_z} \left(\frac{\alpha_{32}}{\beta} - \frac{\bar{\alpha}_3 v \lambda_y}{\beta} \right)\Big|_{k+1} \ \bar{\zeta}_{j-1/2,k+1}$$

$$+ \frac{\gamma_z^+}{\lambda_z} \left(\frac{\alpha_{32}}{\beta} + \frac{\bar{\alpha}_3 \, v\lambda_y}{\beta} \right) \Bigg|_k \bar{\zeta}_{j+1/2,k}$$

$$+ \frac{\gamma_z^+}{\lambda_z} \left(\frac{\alpha_{32}}{\beta} - \frac{\bar{\alpha}_3 v\lambda_y}{\beta} \right) \Bigg|_k \bar{\zeta}_{j-1/2,k} \qquad \text{(B53)}$$

where $\qquad \bar{\alpha}_3 = \alpha_{31} + \alpha_{32} + \alpha_{33}$ $\qquad\qquad\qquad$ (B54)

and $\qquad S_z = \dfrac{2v\lambda_z}{\Delta z}$ $\qquad\qquad\qquad\qquad\qquad$ (B55)

APPENDIX C

DERIVATION OF PRESSURE EQUATION

The three scalar components of the Navier-Stokes equations are given by

$$\frac{\partial u}{\partial t} + u \frac{\partial u}{\partial x} + v \frac{\partial u}{\partial y} + w \frac{\partial u}{\partial z} = \frac{-1}{\rho} \frac{\partial p}{\partial x} + \nu \nabla^2 u \qquad (C1)$$

$$\frac{\partial v}{\partial t} + u \frac{\partial v}{\partial x} + v \frac{\partial v}{\partial y} + w \frac{\partial v}{\partial z} = \frac{-1}{\rho} \frac{\partial p}{\partial y} + \nu \nabla^2 v \qquad (C2)$$

$$\frac{\partial w}{\partial t} + u \frac{\partial w}{\partial x} + v \frac{\partial w}{\partial y} + w \frac{\partial w}{\partial z} = \frac{-1}{\rho} \frac{\partial p}{\partial z} + \nu \nabla^2 w \qquad (C3)$$

Take the partial derivative of Eq. (C1) with respect to x, Eq. (C2) with respect to y and Eq. (C3) with respect to z and find

$$\frac{\partial}{\partial t} \left(\frac{\partial u}{\partial x} \right) + \left(\frac{\partial u}{\partial x} \right)^2 + u \frac{\partial^2 u}{\partial x^2} + \frac{\partial v}{\partial x} \frac{\partial u}{\partial y} + v \frac{\partial^2 u}{\partial x \partial y}$$

$$+ w \frac{\partial w}{\partial x} \frac{\partial u}{\partial z} + w \frac{\partial^2 u}{\partial x \partial z} = \frac{-1}{\rho} \frac{\partial^2 p}{\partial x^2} + \nu \frac{\partial}{\partial x} (\nabla^2 u) \qquad (C4)$$

$$\frac{\partial}{\partial t} \left(\frac{\partial v}{\partial y} \right) + \frac{\partial u}{\partial y} \frac{\partial v}{\partial x} + u \frac{\partial^2 v}{\partial x \partial y} + \left(\frac{\partial v}{\partial y} \right)^2 + v \frac{\partial^2 v}{\partial y^2} + \frac{\partial w}{\partial y} \frac{\partial v}{\partial z}$$

$$+ w \frac{\partial^2 v}{\partial y \partial z} = -\frac{1}{\rho} \frac{\partial^2 p}{\partial y^2} + \nu \frac{\partial}{\partial y} (\nabla^2 v) \qquad (C5)$$

$$\frac{\partial}{\partial t} \left(\frac{\partial w}{\partial z}\right) + \frac{\partial u}{\partial z} \frac{\partial w}{\partial x} + u \frac{\partial^2 w}{\partial x \partial z} + \frac{\partial v}{\partial z} \frac{\partial w}{\partial y} + v \frac{\partial^2 w}{\partial y \partial z} + \left(\frac{\partial w}{\partial z}\right)^2$$

$$+ w \frac{\partial^2 w}{\partial z^2} = -\frac{1}{\rho} \frac{\partial^2 p}{\partial z^2} + \nu \frac{\partial}{\partial z} (\nabla^2 w) \tag{C6}$$

Add Eqs. (C4), (C5) and (C6) together to find,

$$\frac{\partial}{\partial t} \left(\frac{\partial u}{\partial x} + \frac{\partial v}{\partial y} + \frac{\partial w}{\partial z}\right) + \left(\frac{\partial u}{\partial x}\right)^2 + \left(\frac{\partial v}{\partial y}\right)^2 + \left(\frac{\partial w}{\partial z}\right)^2 + 2 \left(\frac{\partial v}{\partial x} \frac{\partial u}{\partial y}\right.$$

$$+ \frac{\partial w}{\partial x} \frac{\partial u}{\partial z} + \frac{\partial w}{\partial y} \frac{\partial v}{\partial z}\right) + u \left(\frac{\partial^2 u}{\partial x^2} + \frac{\partial^2 v}{\partial x \partial y} + \frac{\partial^2 w}{\partial x \partial z}\right)$$

$$+ v \left(\frac{d^2 v}{dy^2} + \frac{\partial^2 u}{\partial x \partial y} + \frac{\partial^2 w}{\partial y \partial z}\right) + w \left(\frac{\partial^2 u}{\partial x \partial y} + \frac{\partial^2 v}{\partial y \partial z} + \frac{\partial^2 w}{\partial z^2}\right)$$

$$= -\frac{1}{\rho} \nabla^2 p + \nu \left[\frac{\partial}{\partial x} (\nabla^2 u) + \frac{\partial}{\partial y} (\nabla^2 v) + \frac{\partial}{\partial z} (\nabla^2 w)\right] \tag{C7}$$

Imposing the continuity condition

$$\frac{\partial u}{\partial x} + \frac{\partial v}{\partial y} + \frac{\partial w}{\partial z} = 0 \tag{C8}$$

allows Eq. (C7) to be written as:

$$\left(\frac{\partial u}{\partial x}\right)^2 + \left(\frac{\partial v}{\partial y}\right)^2 + \left(\frac{\partial w}{\partial z}\right)^2 + 2\left(\frac{\partial v}{\partial x} \frac{\partial u}{\partial y} + \frac{\partial w}{\partial x} \frac{\partial u}{\partial z} + \frac{\partial w}{\partial y} \frac{\partial v}{\partial z}\right) = \frac{-1}{\rho} \nabla^2 p. \tag{C9}$$

Expand the first three terms on the left side of Eq. (C9) as follows:

$$\left(\frac{\partial u}{\partial x}\right)^2 + \left(\frac{\partial v}{\partial y}\right)^2 + \left(\frac{\partial w}{\partial z}\right)^2 = \left(\frac{\partial u}{\partial x} + \frac{\partial v}{\partial y} + \frac{\partial w}{\partial z}\right)^2$$

$$- \left(\frac{\partial u}{\partial x} \frac{\partial v}{\partial y} + \frac{\partial u}{\partial x} \frac{\partial w}{\partial z} + \frac{\partial v}{\partial y} \frac{\partial u}{\partial x} + \frac{\partial v}{\partial y} \frac{\partial w}{\partial z} + \frac{\partial w}{\partial z} \frac{\partial u}{\partial x} + \frac{\partial w}{\partial z} \frac{\partial v}{\partial y}\right) \tag{C10}$$

Imposing the continuity equation on Eq. (C10) and substituting the results into Eq. (C9) results in the following elliptic equation for the pressure field.

$$\nabla^2 p = -2\rho\left[\frac{\partial v}{\partial x}\frac{\partial u}{\partial y} + \frac{\partial w}{\partial x}\frac{\partial u}{\partial z} + \frac{\partial w}{\partial y}\frac{\partial v}{\partial z} - \frac{\partial u}{\partial x}\frac{\partial v}{\partial y} - \frac{\partial u}{\partial x}\frac{\partial w}{\partial z} - \frac{\partial v}{\partial y}\frac{dw}{\partial z}\right] \qquad (C11)$$

1. Report No.	2. Government Accession No.	3. Recipient's Catalog No.
4. Title and Subtitle A NUMERICAL STUDY OF THREE-DIMENSIONAL VORTEX BREAKDOWN		**5. Report Date** MAY 1987
		6. Performing Organization Code
7. Author(s) Robert E. Spall Robert L. Ash		**8. Performing Organization Report No.**
		10. Work Unit No.
9. Performing Organization Name and Address Old Dominion University Research Foundation P.O. Box 6369 Norfolk, Virginia 23508		**11. Contract or Grant No.** NAG-1-530
		13. Type of Report and Period Covered Contractor Report
12. Sponsoring Agency Name and Address National Aeronautics and Space Administration Washington, DC 20546		**14. Sponsoring Agency Code**

15. Supplementary Notes

Technical Monitor: John Anders, Jr.
Principal Investigator: Dr. Robert L. Ash

16. Abstract

A numerical simulation of bubble-type vortex breakdown using a unique discrete form of the full three-dimensional, unsteady incompressible Navier-Stokes equations is performed. The Navier-Stokes equations are written in a vorticity-velocity form and the physical problem is not restricted to axisymmetric flow. Based on the results of previous study, the problem is parametrized in terms of a Rossby number-Reynolds number basis. Utilization of this parameter duo dictates the form of the free-field boundary condition specification and allows control of the axial breakdown location within the computational domain. The structure of the breakdown bubble is studied through time evolution plots of planar projected velocity vectors as well as through plots of planar projected velocity vectors as well as through plots of particle traces and vortex lines. These results are favorably compared with previous experimental studies. In addition, profiles of all three velocity components are presented at various axial stations and a Fourier analysis is performed to identify the dominant circumferential modes. The dynamics of the breakdown process are studied through plots of axial variation of rate of change of integrated total energy and rate of change of integrated enstrophy, as well as through contour plots of velocity, vorticity and pressure.

17. Key Words (Suggested by Author(s)) Vortex Dynamics, Navier-Stokes Equations, Vortex Breakdown, Laminar Flows, Three-Dimensional Flows, Numerical Solution, Vorticity-Velocity Formulation, Breakdown Bubble	18. Distribution Statement		
19. Security Classif. (of this report)	20. Security Classif. (of this page)	21. No. of Pages	22. Price*

*For sale by the National Technical Information Service, Springfield, Virginia 22161